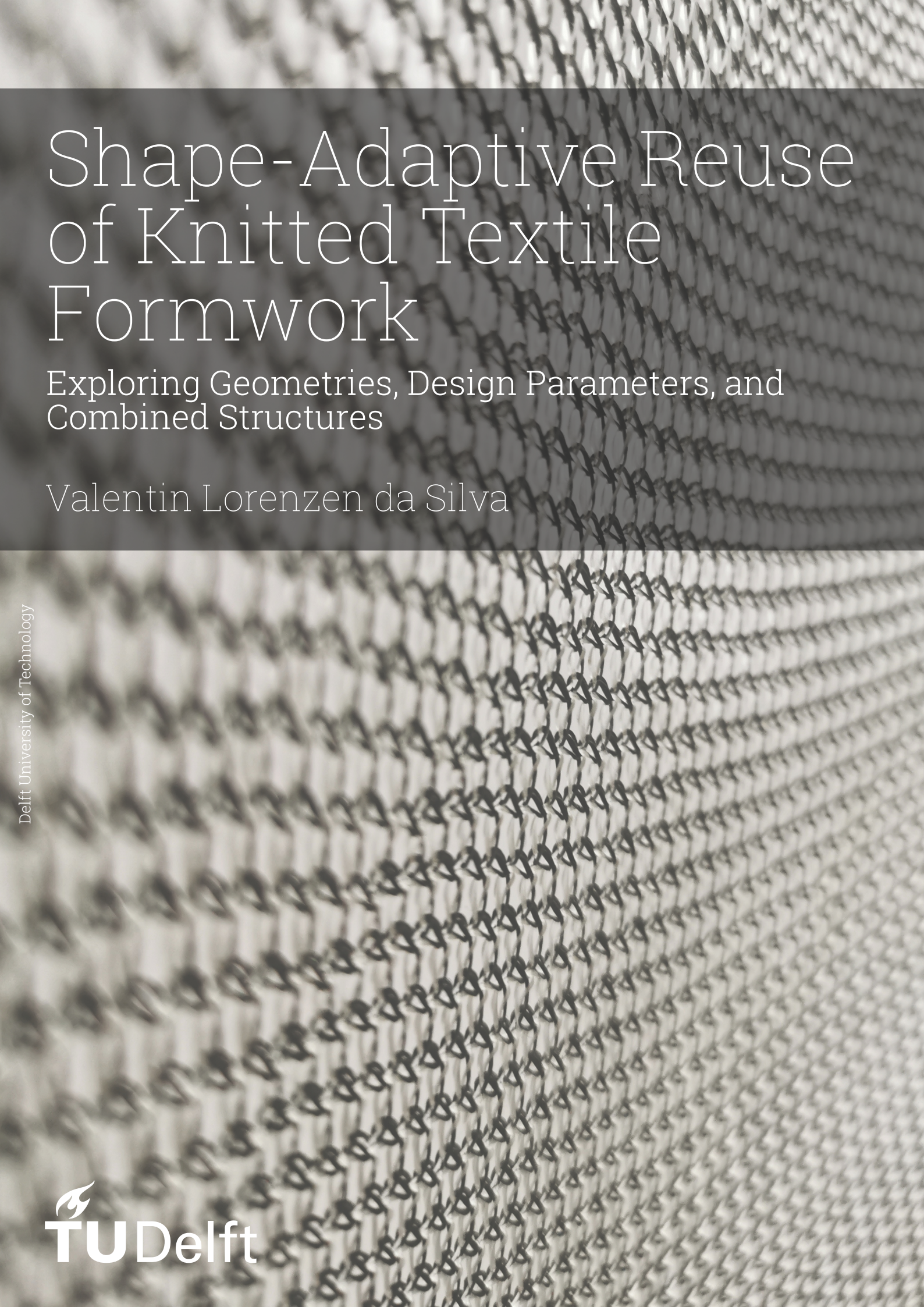

Shape-Adaptive Reuse of Knitted Textile Formwork

Exploring Geometries, Design Parameters, and Combined Structures

Valentin Lorenzen da Silva

Delft University of Technology

TU Delft

Faculty of Civil Engineering and Geosciences

Shape-Adaptive Reuse of Knitted Textile Formwork

Exploring Geometries, Design Parameters, and Combined Structures

by

Valentin Lorenzen da Silva

to obtain the degree of Master of Science
at the Delft University of Technology,
to be defended publicly on Thursday August 22, 2024.

Student number: 5856531

Thesis committee:

Dr. Mariana Popescu,	TU Delft
Dr. Robin Oval,	TU Delft
Dr. Mladena Luković,	TU Delft
Dr. Pierluigi D'Acunto	TU Munich

TU Delft Delft University of Technology

Abstract

Concrete is the most used construction material worldwide and the cement industry is responsible for around 7% of the global CO2 emissions. Due to its cost efficiency, durability and ubiquity, it is being severely overused in current engineering practice, while material efficient construction can potentially save between 24-50% of the emissions associated with concrete and cement. Considering the overdesign of recently constructed buildings, structural design optimization represents an important tool in addressing material-inefficient construction, and can contribute significantly to the improvement of the ecological impact of our built environment.

This thesis explores the geometric design space and reuse potential of knitted textile formwork for the creation of concrete structures of various geometries. While traditional rigid formworks limit the creation of structurally efficient, doubly curved structures due to material intensiveness and high cost, flexible fabric formworks offer significant advantages in terms of sustainability, efficiency, and the ability to achieve complex shapes.

Through physical prototyping and computational analysis, the study identifies a wide range of achievable shapes and evaluates their design parameters, accuracy and structural performance. The physical prototyping phase involves the fabrication of multiple small-scale models and combining these to larger structures. Different tensioning methods, such as cables, rods, and weights, are applied to the fabric to achieve various geometries. Furthermore, the study investigates the effects of repeated use on the fabric's performance. The fabricated geometries are analyzed through 3D scanning to assess their accuracy and to determine the influence of tensioning and mortar weight on their resulting geometry. Through finite element analysis, the structural performance of combined shapes, created by connecting multiple shell elements, is evaluated.

The prototypes, built throughout this research, demonstrate the feasibility of creating complex, doubly curved shapes with the same fabric sample, applying various tensioning strategies, highlighting the adaptability and reusability of the formwork system. The study finds, that that the fabric can be reused multiple times for the fabrication of different elements without significant loss of quality or functionality. The geometrical analysis shows that the formwork system can produce accurate and repeatable geometries, despite the manual fabrication of the prototypes. The results of the structural analysis provide insight into the influence of the connection between individual elements, element orientation and their overall configuration on the structural performance of structures, composed of multiple elements. The results reveal, that that in the design of composed structures, special attention must be paid to the avoidance of alignment of flexible joints between elements and regions of single curvature and low stiffness to avoid the occurrence of mechanism-like effects.

The findings of this research contribute to the development of a design methodology for the creation of complex structures using flexible formwork systems. The findings shed light on the design space provided by the fabrication method and the mechanical behavior of the resulting structures, and thereby enables designers to make informed decisions to optimize material usage, reduce waste, and create innovative, sustainable structures. The study successfully demonstrates the potential of knitted textile formwork as a versatile and sustainable solution for the construction industry, offering new possibilities for resource efficient fabrication methods.

Acknowledgements

I am very grateful to my thesis committee for their ongoing support and advice throughout this thesis. I want to give a special thanks to my chair, Dr. Mariana Popescu, for inspiring and encouraging me to think outside the box and helping make this thesis happen. I also would like to thank Dr. Robin Oval and Dr. Pierluigi D'Acunto for their guidance on structural mechanics, analysis, and modeling, and Dr. Mladena Lucović for her insights on materiality, which were essential for the physical prototyping.

A big thank you to the Tailored Materiality Research group for making the lab work feel like a team effort. Special thanks to Anass Kariouh for working with me on the initial prototyping phase and sharing his knowledge and to Nikoletta Christidi and Lucy Flieger for their support and inspiration in the lab. Also, I would like to thank the technicians at the Stevin II lab for all their help, without which the physical prototyping would not have been possible.

Lastly, I want to thank my parents, Petra and Luiz, for always supporting and believing in me, and to my friends in Delft, who made my time here so enjoyable.

Contents

List of Figures

List of Tables

1

Introduction

1.1. Research context

Concrete is the most used construction material worldwide and the cement industry is responsible for around 7% of the global CO2 emissions [2]. Due to its cost efficiency, durability and ubiquity, it is being severely overused in current engineering practice, while material efficient construction can potentially save between 24-50% of the emissions associated with concrete and cement [5]. Considering the overdesign of recently constructed buildings, structural design optimization represents an important tool in addressing material-inefficient construction, and can contribute significantly to the improvement of the ecological impact of our built environment [12].

In the context of structural optimization, the formability of concrete offers the important advantage to assume nearly any shape regardless of geometrical complexity [20]. Despite the geometrical freedom coming from the formability of concrete, prismatic and conventional forms dominate our built environment due to their relatively lower cost compared to structurally optimized shapes such as doubly curved shells [37]. The cost intensity of structures of complex or non-standard geometries largely stems from the formwork needed for their construction, which can make up more than 70% of the total cost of the structure [28]. The formwork used to create these structures is typically made from timber using subtractive methods, which limits the reusability of the formwork to structures of similar geometry. This limited reusability often results in large amounts of construction waste, as the timber formwork for complex structures is often single-use and disposed after construction. Furthermore, extensive scaffolding, falsework and labour is required during assembly and construction, further reducing its efficiency and sustainability [20, 28]. The aforementioned issues of cost and labour intensity, construction waste and lack of sustainability are addressed by digital fabrication methods for concrete elements that have gained popularity in recent years [23]. Amongst other recent innovations, flexible fabric formwork offers a promising approach to creating architecturally interesting and structurally optimized structures that can achieve significant material savings compared to conventional forms. By utilizing the fabric's inherent flexibility as a design advantage, new structural, architectural and manufacturing possibilities are introduced [14]. Successful applications of fabric formwork in various typologies of structures and structural elements, as presented in [36] and [14], showcase these new design possibilities. Advances into the reuse potential of fabric formwork systems have been made by the research project around the F.A.B. shell [37], in which a demountable steel-arch system has been designed to allow for the easy deconstruction of the formwork. While the designed system promotes multiple reuses of the formwork, it is limited to reuse in structures of the same geometry due to the uniqueness of the membrane's cutting pattern.

Little to no research has been done on the potential reuse of fabric formwork in structures of different geometry. However, the flexibility of the fabric formwork offers the possibility of being tensioned into different shapes, by manipulation of the boundary conditions, prestressing, and other parameters. Therefore, if considered in the initial design, one piece of flexible textile formwork can potentially be reused to produce structures of different geometry. Up until now, it has not been exhaustively investi-

gated what geometries and shapes are achievable from one base geometry or combinations of base geometries of the fabric formwork. Furthermore, it is not known under which modifications of boundary, loading or prestressing conditions these desired shapes can be achieved or how these modifications can be realized physically.

1.2. Problem statement and research objectives

As of now, there is no comprehensive knowledge on the reuse potential of fabric formwork for the application in a structure of different geometry. This study aims to experimentally explore the design spectrum achievable with a piece of flexible fabric formwork, including the various shapes and their respective combinations. Furthermore, it seeks to contribute to the development of a design methodology for the use and reuse of flexible fabric formwork. To achieve said objectives, the following research question is formulated:

- **How can knitted textile be employed as reusable formwork for the fabrication of shell structures of various shapes?**

To answer this research question, the following sub-questions will be investigated:

- What are the different tensioning and support parameters that can be manipulated to change the geometry of the textile?
- How does a piece of knitted textile formwork perform after repeated use?
- What new geometries can be achieved from (modular) combinations of base geometries?
- What implications does the structural performance of combined structures have for their design?

1.3. Scope

This thesis investigates the potential of flexible fabric formwork through a series of qualitative and structural evaluations. The research includes a qualitative assessment of tensioning methods such as cables, rods, and weights to understand their impact on resulting shapes. It explores various combinations of shapes, providing insights into the design possibilities and constraints of the formwork system. Additionally, the study qualitatively evaluates the reusability of fabric formwork, examining its performance after multiple uses without quantifying the maximum number of possible reuses for the fabric.

The influence of prestress and the weight of the mortar on the geometry of the structures is analyzed to determine how these factors affect the final forms. This study does not include material strength testing of the fabric or plaster material. Consequently, no specific data on the maximum loading capacity of the fabric is derived.

Structural analysis is conducted to evaluate the overall performance of the constructed prototypes, focusing on aspects such as strain energy as well as stress and deformation analysis. The analyses aim to provide an understanding of the structural behavior of the combined geometries. The study does not incorporate non-linear analysis, which limits the understanding of potential non-linear behaviors in real-world applications.

1.4. Methods

Throughout this study, both physical prototyping and computational analyses are utilized to achieve the research objectives and answer the research questions. Initially, key cornerstones are established, including the classification of typologies, a structured evaluation of potential support configurations for a specific case, and the definition of a logical approach to the combination of shapes.

During the subsequent physical prototyping phase, small scale plaster prototypes are built to evaluate design parameters, repeated use of the fabric formwork and combinations of geometries. This phase involves an iterative process with three cycles of design, construction, and evaluation. The first iteration focuses on exploring various geometries and tensioning methods such as cables, rods and weights. The second and third iterations investigate the repeatability of geometries and the potential for modular combinations, focusing on the reuse of a single fabric sample and the construction of combined

structures. Furthermore, 3D scans of the physical prototypes are produced to analyze their geometric accuracy and the influence of tensioning and material weight on the final forms.

The structural analysis of combined shapes evaluates the performance of the prototypes built in the previous phase using finite element analysis (FEA) software and simplified models. In this step, various connection types and element configurations are considered, and their impact on the structural behavior is assessed.

1.5. Thesis structure

This thesis is structured as follows: **Section 2** provides a comprehensive **literature review**, explaining the historical context, recent advancements in flexible formwork systems, and relevant concepts of geometry exploration. **Section 3** outlines the **methodology** employed in this research, elaborating the classification and variation of geometries, the **physical prototyping** process, and the **structural analysis of combined shapes**. **Section 4** presents the **results** obtained from both the physical prototyping and structural analysis phases, highlighting key findings and observations. In **Section 5**, an in-depth **discussion** of the results is provided, analyzing their implications and limitations. Finally, **Section 6 concludes** the thesis by summarizing the main findings, stating limitations, and proposing potential directions for future research.

2

Literature review

To provide context and position this study within the current state-of-the-art, as well as to identify the existing research gap that it addresses, a comprehensive literature review is conducted. This review will focus on the history and latest advancements in flexible formworking systems, precedents in geometry exploration, and fundamental concepts related to modularity.

2.1. Geometry and modularity

Geometrical concepts play a fundamental role in architectural design and structural engineering, having been explored in various ways and with different focuses throughout history [31, 18]. From studies on fundamental geometrical concepts such as Platonic solids [8] or quadric surfaces [6] to studies of the geometries of tensile and shell structures in an architectural context [4, 25], geometry has been the focus of research in various fields such as mathematics, architecture, engineering.

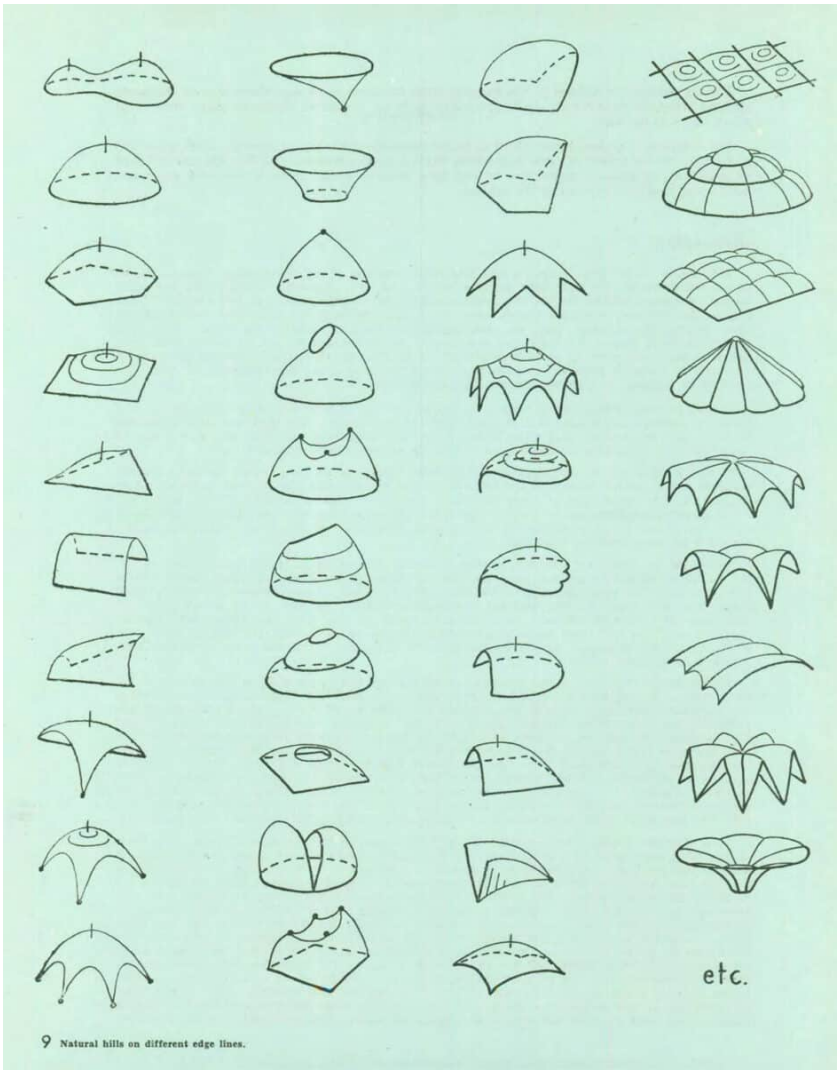

Figure 2.1: Heinz Isler's "natural hill" forms [4]

Figure 2.1 showcases a variety of shell shapes proposed by Heinz Isler in his 1961 paper, "New Shapes for Shells." Isler is renowned for his physical form-finding methods, such as pressurized membranes and hanging cloth models, which he used to design his highly efficient, complex concrete shells. His research and shape explorations primarily utilized these physical, experimental formfinding techniques. As illustrated in Figure 2.1, his approach followed a structured logic, varying edge lines and systems of lines and points and evaluating the thereof resulting "natural hill" forms [4]. In his experimental explorations, he made use of an iterative approach of testing multiple design variations that emerged from the physical models until a satisfying shape has been found. In the physical models using the hanging cloth approach, the deformation of a cloth loaded under gravity load is used to create funicular shapes. If reversed, these shapes result in structures with dominating compressive stresses under self-weight, extending the two-dimensional principle of the catenary into space [3]. Heinz Isler's shape explorations as shown in Figure 2.1 demonstrate the vastness of possibilities for shell shapes.

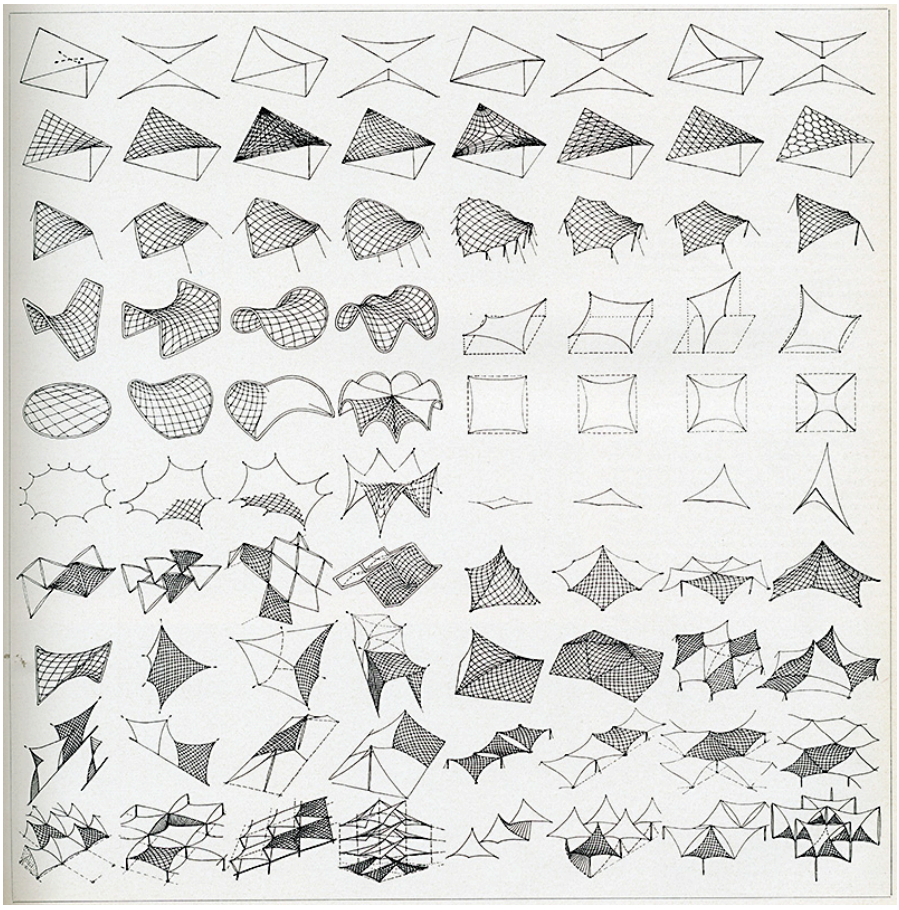

Figure 2.2: Frei Otto's tensile structure diagrams [25]

While Isler used physical form-finding to create compression-dominant concrete shell structures, Frei Otto applied these methods to develop tensile structures such as spatial cable nets and membrane structures [3]. As depicted in Figure 2.2, Otto conducted extensive studies on possible geometries for tensile structures. The illustrations showcase variations in membrane base shapes, ranging from straight to curvilinear outlines and their combinations. Additionally, the diagrams explore different support conditions, including point-supported cable-stayed supports and line supports. While Isler's shapes, shown in Figure 2.1, are predominantly synclastic, Otto's tensile structures, depicted in Figure 2.2, are anticlastic. Besides studying individual geometries, Otto also explored modular combinations, demonstrating the possibilities that arise if composed structures are considered.

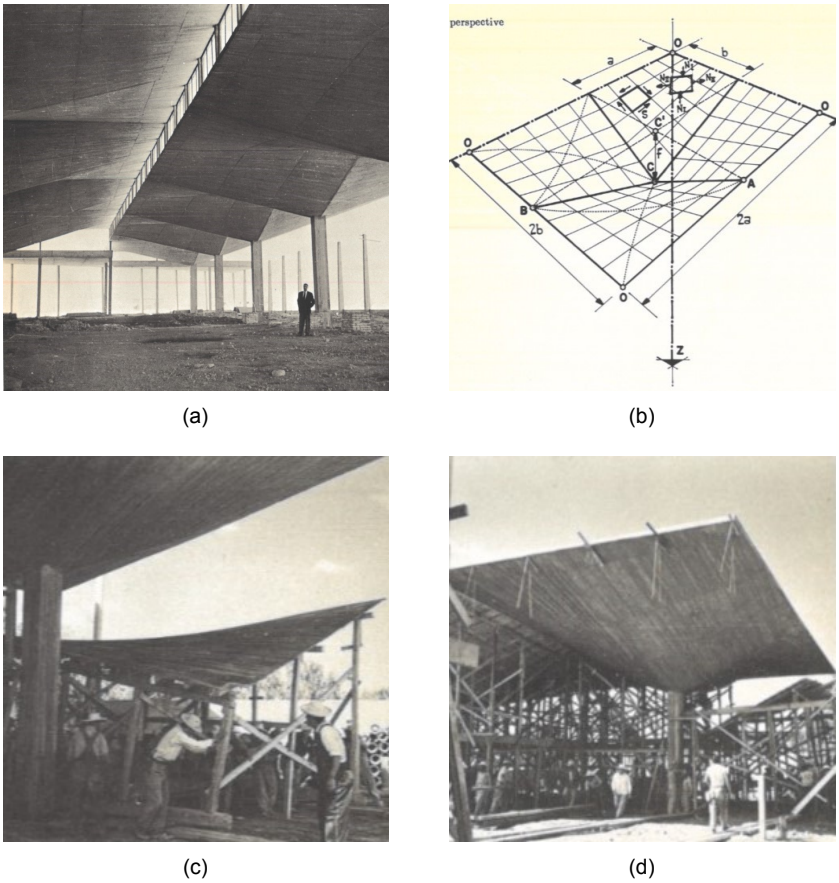

(a) (b)

(c) (d)

Figure 2.3: Construction of Candela's Rio's warehouse, 1954: (a) Finished structure, (b) geometry of the umbrella roof elements, (c) and (d) formwork and construction of the roof structure [10]

Unlike Isler and Otto, who made use of form-finding to derive structurally efficient shapes, Felix Candela's shell structures were geometrically designed, to meet practical construction requirements. As a key feature in his work, he utilized ruled surfaces, which is a type of surface that can be generated by moving a straight line through space. Ruled surfaces, such as hyperbolic paraboloids, are not only structurally efficient due to their double curvature, but also simpler to construct because they allow for the use of straight formwork. This method simplified the fabrication process, as straight wooden planks could be used to create complex curved surfaces, reducing both time and cost. This geometric approach enabled Candela to create intricate forms while ensuring they could be practically realized [10]. This approach stands in contrast to Isler's and Otto's form-finding techniques, which prioritize organic, naturally derived shapes that require more complex and costly formwork solutions. An example of Candela's trademark hypar (hyperbolic paraboloid) umbrella structures is the in Figure 2.3 shown Rio's warehouse.

Both Heinz Isler and Frei Otto historically demonstrated the value of physical modeling and form-finding in creating efficient and elegant structures. Their innovative work laid the foundation for modern form-finding and design exploration tools, setting a precedent for successful experimental approaches to the design of complex shell and tensile structures [3]. In contrast, Candela's work serves as an example for structurally efficient but fabrication aware geometric design, that considers construction constraints.

2.2. Flexible formwork

Fabric formwork is a construction technology that employs structural membranes as the primary material for concrete molds [36]. Unlike traditional rigid formwork, which typically uses materials such as timber or steel, it leverages the inherent flexibility of these membranes to achieve free-form and doubly curved geometries. Such complex shapes, if made with conventional formworking technologies, are

highly resource-intensive, wasteful, and complicated to construct [36, 24]. The concept of fabric formwork in concrete construction dates back to the late 1800s and early 1900s. Over the decades, fabric formwork has been adapted for various structural applications and can be found in a broad spectrum of structures, including shells, floors, beams, columns, walls, foundations, and many other forms as shown in Figure 2.4 [14, 38]. A detailed overview of historical and contemporary examples of flexible and fabric formwork applications can be found in the works of Hawkins [14] and Veenendaal [36]. These studies present the history as well as numerous case studies and projects where fabric formwork has been successfully implemented, showcasing its advantages in terms of efficiency, sustainability, and design innovation.

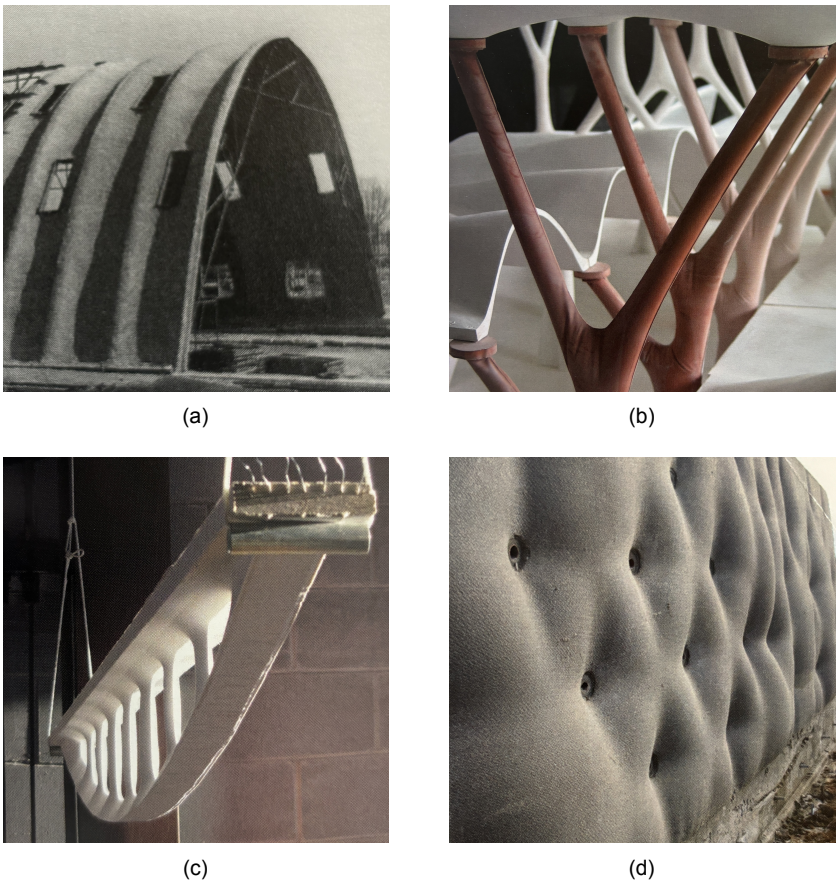

(a) (b) (c) (d)

Figure 2.4: Historic examples of applications of fabric formwork: (a) Ctesiphon shell by James Waller (1948), (b) retaining wall by Wilf Meynell and Alan Chandler(2011), (c) branched column model, (d) truss model [38]

Recent research projects have introduced innovative approaches to flexible formworking systems that will be discussed in the following paragraphs.

One of the formworking systems relevant to this study is the adaptive mold system, as presented in [33]. This system facilitates the fabrication of doubly curved geometries using a membrane supported by height-adjustable piston fixing points, which are computer-controlled to assume a prescribed shape (Figure 2.5). The ability of this system to adapt to various shapes without permanent modifications to the formwork allows for its reuse in producing elements not only with same but also with different geometries. Limitations of this technology include the overall dimensions of the elements that can be produced, maximum inclination angles, and minimum curvature radii. These constraints are introduced by the limited flexibility of the membrane, the height adjustment range of the piston fixing points, the rheological properties of the casting material, and other factors. In addition to the conventional workflow described in [33], this technology supports alternative fabrication workflows, such as deforming the concrete into its final shape after casting, rather than casting it into its final shape initially [13].

Figure 2.5: Example of an adaptive mold system: Adapa Adaptive Mould D200 [1]

Another example of reusable flexible formworking systems is the F.A.B Shell (Fabric-Arch-Base Shell) developed at École des Ponts ParisTech [37]. This system uses a fabric membrane in combination with telescopic steel arches to create doubly curved concrete shell structures. In the demonstrator shown in Figure 2.6, the fabric membrane is tensioned between three arches, with the two outer arches tensioned to the ground with cables to create the prestressing of the membrane. A notable feature of this system is the telescopic mechanism of the arches that support the fabric, which allows them to be retracted, making the formwork demountable after the construction of the permanent shell. This capability opens up the possibility of reusing the same formwork for constructing multiple structures, significantly enhancing the economic and environmental efficiency of the system. The F.A.B Shell demonstrates a promising approach to shell construction using flexible formwork systems, highlighting the importance of (dis-)assembly considerations. While the system enables the reuse of formwork, it is limited to structures of the same geometry, making it particularly suitable for modular building structures that combine multiple repetitive units. Due to the customized cutting pattern and the fabric fabrication involving the permanent welding together of multiple fabric patches, it lacks the adaptability to different shapes that is possible with the adaptive formwork system mentioned in the previous paragraph.

Figure 2.6: F.A.B. Shell by ENPC, 2020: Assembled formwork prototype [37]

The KnitCandela shell by Block Reasearch Group at ETH Zürich shown in Figure 2.7, employs a fabric shuttering installed on a cable net structure as the primary load-bearing, stay-in-place formwork [29]. This system is supported and tensioned within a steel and timber frame. The project utilizes the same custom weft-knitted fabric that will be used in this study's investigations. The KnitCandela prototype effectively demonstrates the application of a knitted textile and cable net formworking system on an architectural scale. The KnitCandela project highlights several advantages of weft-knitting, including the ability to create complex doubly curved geometries without the need for intricate cutting patterns or the assembly of multiple fabric patches. This method allows for precise control of surface geometry and curvatures through local manipulation of the knit properties. Additionally, the project incorporates features for guiding and inserting the supporting cable net directly through the fabric. By using computational

custom tailoring, channels for cables and openings for inflatables were seamlessly integrated into the fabric, eliminating the need for post-production adjustments such as gluing, welding, or stitching parts together. To ensure the fabric had sufficient stiffness to support the load of the concrete cast onto it, a thin stiffening coating of fast-setting cement paste was applied. However, due to the permanent nature of this stiffening layer and its design as a stay-in-place formwork, the fabric cannot be removed from the finished structure and reused for constructing further structures. The successful construction of the KnitCandela prototype showcases the potential of knitted textiles in flexible formwork systems, offering significant benefits in terms of efficiency, sustainability, and the ability to achieve complex geometries with minimal material waste.

(a)

(b)

Figure 2.7: KnitCandela shell by Block Research Group and the Computational Design Group of Zaha Hadid Architects, 2018: (a) Construction and (b) finished shell structure (Photo credits: (a): Mariana Popescu, (b): Angelica Ibarra)

Ongoing research on the formworking system employed in the KnitCandela project has explored the use of weft-knitted textile formwork without applying a stiffening cement-paste layer [17]. This approach introduces new challenges in predicting the deformation behavior of the knitted textile formwork due to its high flexibility. However, it also opens up new design possibilities, leveraging the fabric's inherent flexibility. Additionally, by eliminating the stiffening steps during construction, the fabric can be removed from the structure after the concrete has cured, offering the potential for reuse.

2.3. Research gap

The presented literature and examples of innovative formworking technologies highlight their potential for the sustainable fabrication of complex-shaped structures, utilizing digital design and fabrication methods. Adaptive mold systems, as described in [33], offer significant design freedom for shaping

freeform panel elements and enable the fabrication of multiple elements using the same formwork. However, this system is limited in terms of the overall dimensions of the produced elements, as well as achievable curvatures and inclination angles. The fabric-arch-base formwork system [37], can be reused to create modular structures by combining identical units. However, due to the customization of the fabric patches, this technology is restricted to producing identical elements and is not adaptable to different geometries. The KnitCandela project, presented in [29], showcases a promising approach for constructing complex double-curved structures using a flexible cable-net and CNC-knitted textile shuttering. Although this technology offers significant design freedom, it is designed as a stay-in-place formwork, which prevents its reuse.

These benefits and drawbacks leave open questions regarding the design space of structures using flexible formwork and the reuse of flexible formworks for shell structures of different geometries. Recent advances in knitted textile formworks, as explored in [17], offer promising possibilities for reuse and adaptability which have not yet been explored. In creating these structures, the design process involves multiple stages, combining tensile structures, similar to those of Otto [3], with gravitationally loaded membranes, similar to Isler's hanging cloth models [4, 3] during the casting process. The result is the creation of hybrid shell structures that are not only fabrication-informed but also structurally efficient, similar to Candela's shell structures [10].

3

Methodology

In this section, the conceptual framework and the research methods, that will be employed in this study, will be described. As briefly introduced in Section 1.5, the structure of this research consists of three key elements, that are discussed in detail in the following. Figure 3.1 illustrates these three elements.

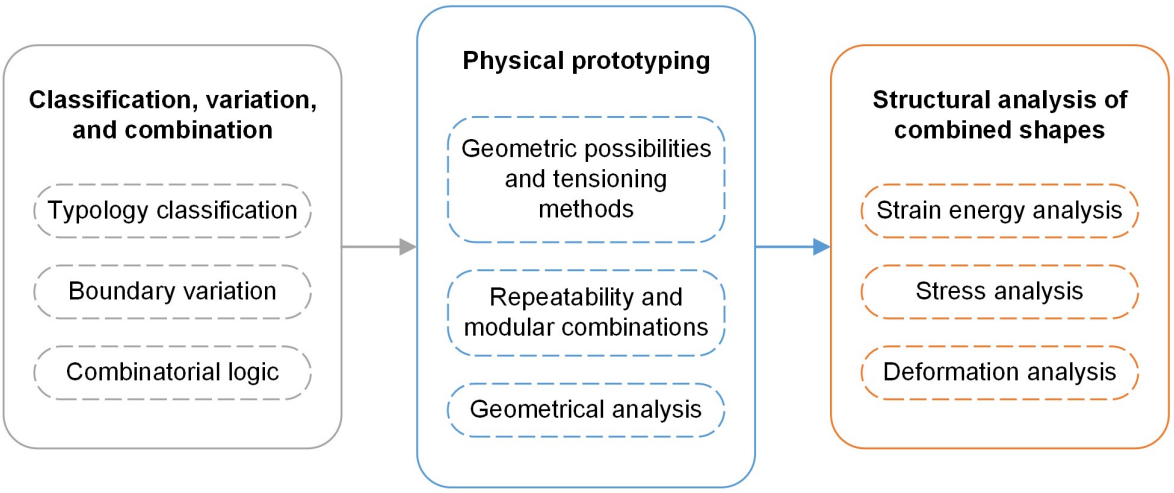

Figure 3.1: Overview of the conceptual framework that is applied throughout the study

3.1. Classification, variation and combination

Before initiating the physical prototyping and structural analysis phases, essential cornerstones are established. These include the classification of typologies, a structured evaluation of potential support configurations for a specific case, and the definition of a logical approach to the combination of shapes.

3.1.1. Typology classification

Different characteristics of a structure such as the ones investigated in this study can be identified. To provide an overview over the different typologies of shapes that can be investigated, a classification of shape characteristics is provided in Figure 3.2.

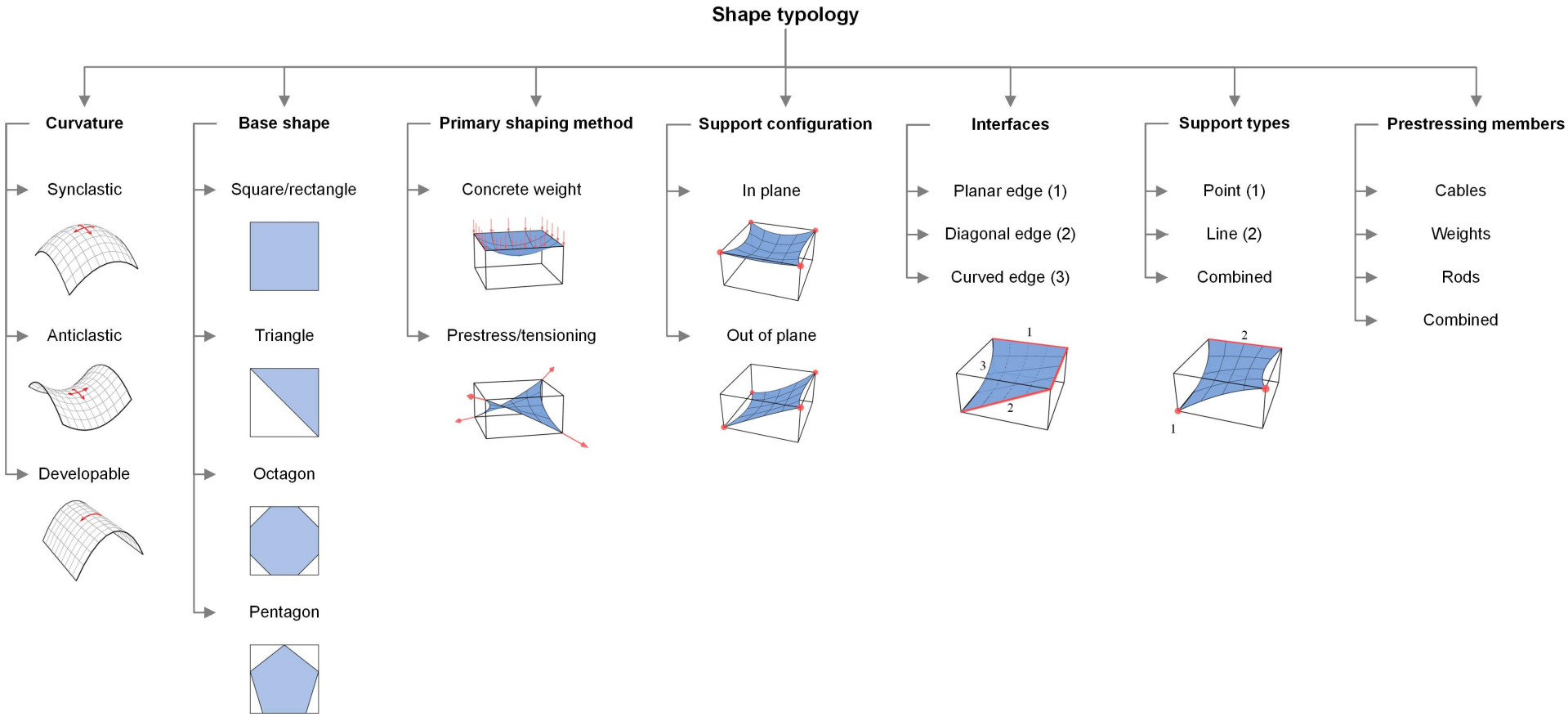

Figure 3.2: Classification of shape characteristics and typologies for flexibly formed shell elements

3.1.2. Boundary variations

Naturally, the possibilities for base geometries, tensioning, supporting, loading, etc. and their respective combinations are infinite. In order to create a comprehensive set of boundary variations, the following limitations are introduced:

- square base geometry
- either point supports or line support
- no additional cables, rods, weights or intermediate supports

Figure 3.3 shows the possible shapes that result from the variation of boundary configurations under the aforementioned limitations. The visualization is divided into point support of the corners or line support of the edges, and further subdivided into the number of edges that is supported in the case of line supports. Moreover, it is divided into how many corner points are supported in plane or out of plane. The asterisk indicates if the configuration is dependent on the direction of the loading. In the case of configurations that have one or more corners supported out of plane, and in which the ”top” supports differ from the ”bottom” supports, the direction of the loading influences the resulting shape of the structure.

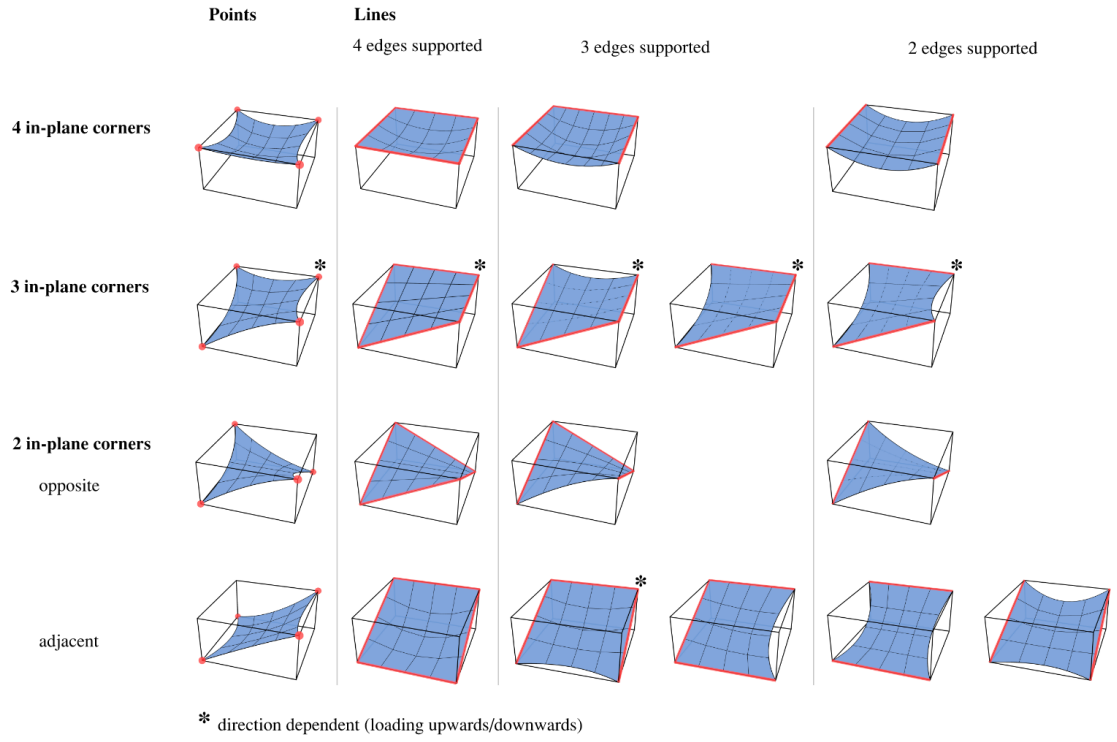

Figure 3.3: Variation of boundary supports (points or lines) for square fabric elements in a supporting frame

Figure 3.4 illustrates examples of boundary configurations and resulting shapes that are achievable when the restriction of using only one support type is removed, allowing the combination of point and line supports.

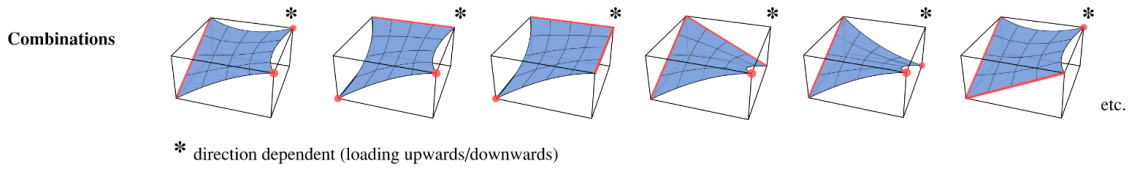

Figure 3.4: Examples of boundary support variations (combinations of points and lines) for square fabric elements in a supporting frame

3.1.3. Combinatorial logic

The geometries resulting from the boundary variations presented in Section 3.1.2 can be combined in various ways. Assuming that only straight edges (planar or diagonal) are connected, the number of possible horizontal combinations can be determined as follows:

With:

- E_i is the number of straight (or compatible) edges of element i
- *n* is the total number of elements that are connected
- n_{comb} is the resulting number of possible configurations

the number of possible configurations n_{comb} becomes:

$$n_{\text{comb}} = E_1 \cdot E_2 \cdot 2, \quad \text{for } n = 2 \tag{3.1}$$

and

$$n_{\text{comb}} = E_1 \cdot E_2 \cdot 2 \cdot \left(\left(\sum_{i=1}^{2} E_i \right) - 2 \cdot (3-2) \right) \cdot E_3 \cdot 2 \ldots \cdot \left(\left(\sum_{i=1}^{n-1} E_i \right) - 2 \cdot (n-2) \right) \cdot E_n \cdot 2, \quad \text{for } n \geq 3 \tag{3.2}$$

or

$$n_{\text{comb}} = 2^{\text{n-1}} \cdot \prod_{i=1}^{n} E_i \cdot \prod_{j=2}^{n-1} \left(\sum_{k=1}^{j} E_k - 2(j-1) \right), \quad \text{for } n \geq 2 \tag{3.3}$$

The concept is applied below using the example of three elements that are connected to each other. The three elements chosen for this example are shown in Figure 3.5.

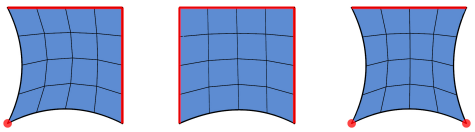

Figure 3.5: Plan view of the example elements (left to right: Element 1, Element 2, Element 3)

With:

- Number of elements: $n = 3$
- Number of compatible edges of Element 1: $E_1 = 2$
- Number of compatible edges of Element 2: $E_2 = 3$
- Number of compatible edges of Element 3: $E_3 = 1$

the number of possible configurations becomes:

$$n_{\text{comb}} = 2 \cdot 3 \cdot 2 \cdot ((2+3) - 2 \cdot (3-2)) \cdot 1 \cdot 2 = 72 \tag{3.4}$$

The number of combinations can be shown by combining the elements step by step and evaluating the number of configurations after the addition of each element. Combining Element 1 and Element 2, yields the following 6 possible configurations:

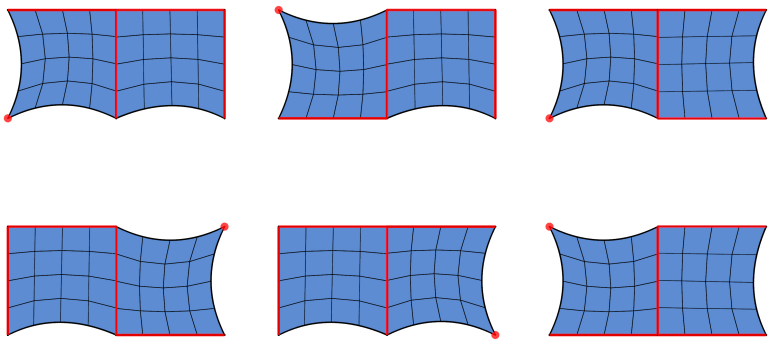

Figure 3.6: Plan view of possible configurations of Element 1 and 2

Furthermore, Element 1 (or 2) can also be flipped upside down, doubling the number of configurations:

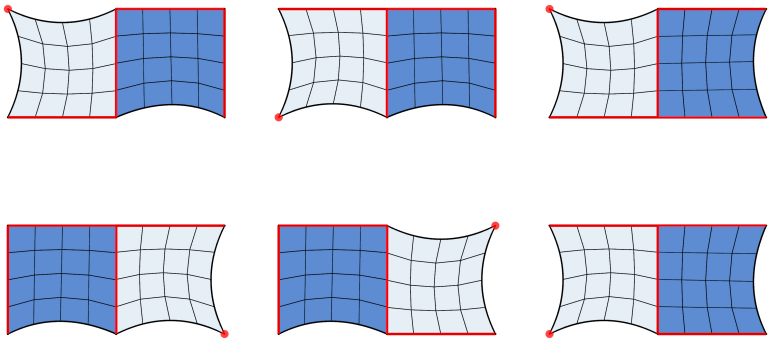

Figure 3.7: Plan view of possible configurations of Element 1 and 2 if Element 1 is flipped upside down

Therefore, there are 12 possible configurations of Element 1 and 2. Element 1 and 2 together have $E_{\text{total}} = E_1 + E_2 = 2 + 3 = 5$ compatible edges, leaving the system with $E_{\text{free}} = E_1 + E_2 - 2(n-1) = 2 + 3 - 2 * (2-1) = 3$ free compatible edges to which Element 3 can be connected. Therefore, each of the 12 possible configurations of the previous step provides 3 possible connections of Element 3, yielding $12 * 3 = 36$ possible configurations. Considering, that Element 3 can be flipped, the number of possible configurations doubles again, resulting in a total number of $36 * 2 = 72$ possible configurations.

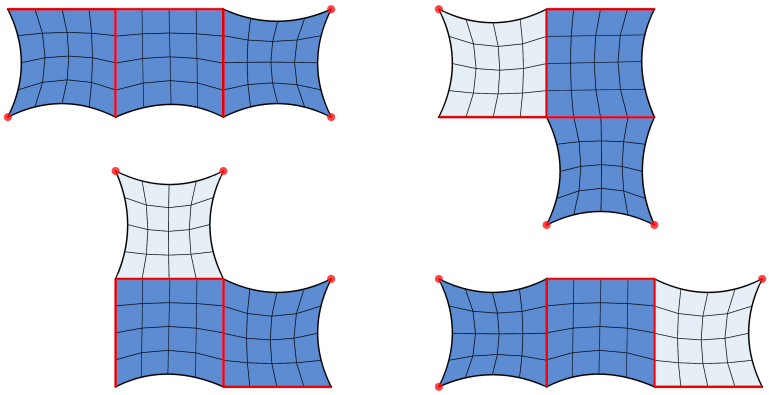

Figure 3.8: Examples of the 72 possible configurations of Elements 1, 2, and 3

3.2. Physical prototyping

During the physical prototyping phase, small scale prototypes are built to evaluate design parameters, repeated use of the fabric formwork and combinations of geometries. An iterative approach will be employed, involving three iterations of the design - construction - evaluation cycle as illustrated in Figure 3.9. In each iteration, the prototypes to be constructed will be designed, as well as the respective fabrication workflow and necessary tools, such as the fabric layout and supporting frame. Following the construction of the prototypes, both the prototypes and the fabrication workflow will be evaluated. This evaluation will inform and update the design for the subsequent iteration. Each iteration will not only implement the findings from the previous cycles but will also focus on different aspects for deeper investigation. The first iteration will concentrate on exploring geometries and evaluating different tensioning methods (3.2.1). The second and third iterations will focus on the repeatability of geometries and modular combinations of geometries (3.2.2). In the context of the repeatability of geometries, 3D scans of the physical prototypes are produced to analyze their geometric accuracy and the influence of tensioning and material weight on the final forms.

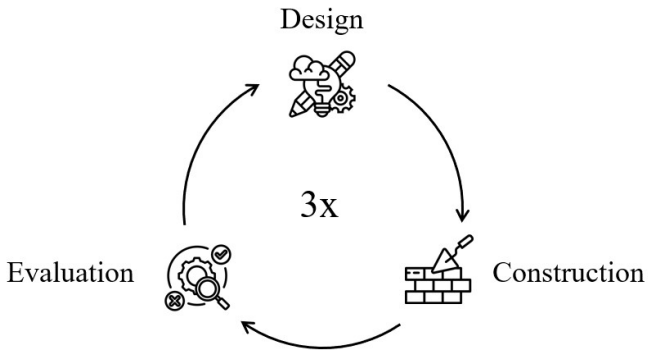

Figure 3.9: Schematic representation of the prototyping cycle: Design - Construction - Evaluation

3.2.1. Geometry exploration and tensioning methods - Iteration 1

In this phase of physical prototyping, various tensioning methods will be applied to investigate their possibilities, limitations, feasibility, and resulting shapes. Additionally, the adaptability of a single fabric layout to accommodate different tensioning methods will be assessed to determine its overall versatility.

Anticipated geometries, tensioning, loading and supports

Different tensioning methods as well as different support configurations will be tested. The tested tensioning methods include rods, cables and weights. The fabric is supported by steel bars that are fed through channels around the edges of the fabric and loaded by the self-weight of the plaster material

cast on top of it, in addition to its prestensioning. The anticipated test configurations are shown in figure Figure 3.10.

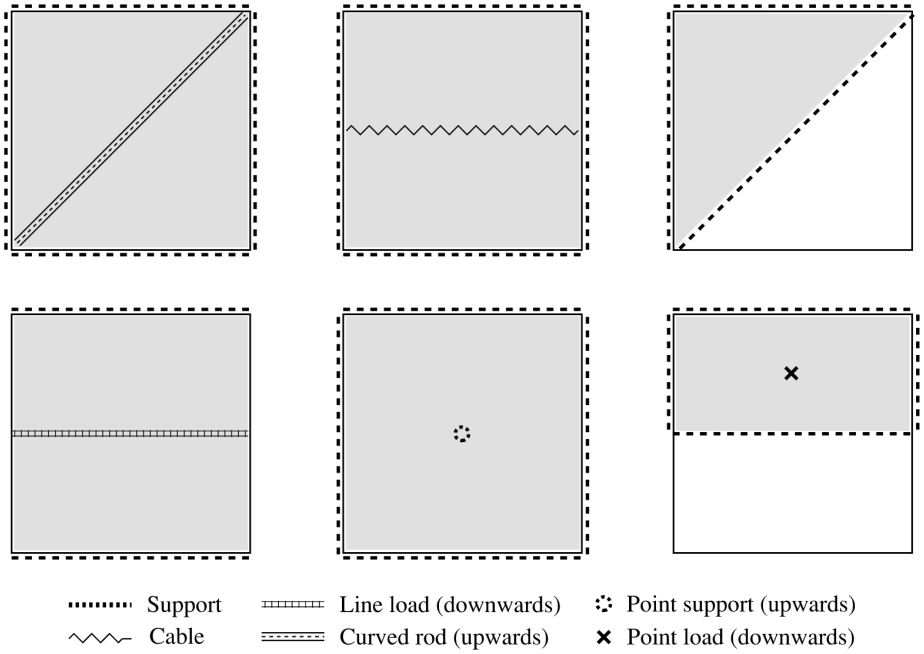

Figure 3.10: Support and loading configurations for the first iteration of physical prototypes

3.2.2. Repeatability and modular combinations - Iteration 2 & 3

Following the exploration of different tensioning strategies in 3.2.1, this phase of the physical prototyping aims to investigate the repeatability of geometries using the same fabric sample and study the geometric possibilities that arise from modular combinations of these geometries.

Chosen geometries

For this part of the investigations, two geometries from the boundary variation in 3.1.2 have been chosen. Examples of composed structures from Heino Engel's book "*Tragsysteme - Structure Systems*" [9] shown in Figure 3.11 served as reference.

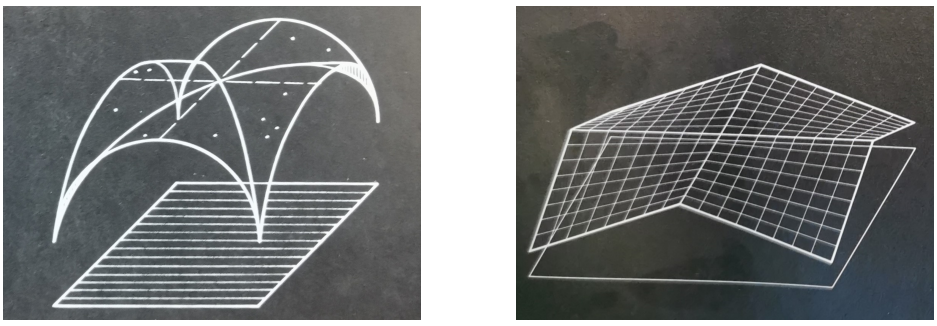

(a) (b)

Figure 3.11: Examples of structures composed of repeated geometries from Heino Engel's "Tragsysteme - Structure Systems" [9]

Translated into the definitions of boundary variations shown in 3.1.2, the two shapes that result, are shown in Figure 3.12. Geometry 1 (Figure 3.12 (a)) represents a more complex geometry with two

curved edges that result from tensioning the fabric at one corner out of plane, while the opposing two edges are continuously supported in plane. Geometry 2 (Figure 3.12(b)) on the other hand, while still being doubly curved, represents a geometry with more simple boundaries that is continuously supported, resulting in four straight edges.

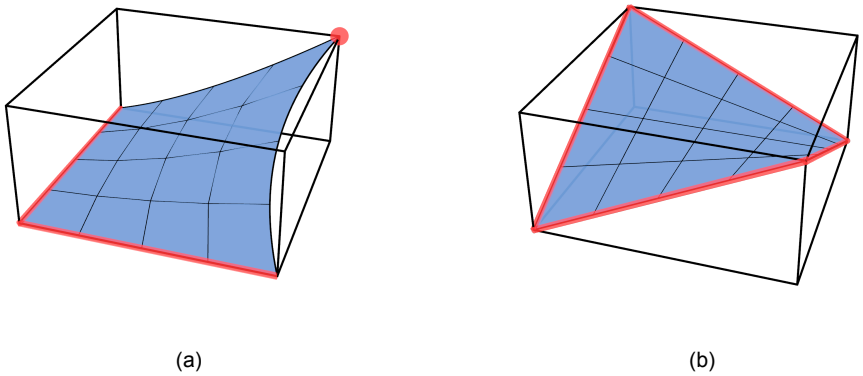

(a) (b)

Figure 3.12: Geometries chosen for the further investigations and physical prototyping: (a) Geometry 1, (b) Geometry 2

In order to assess the repeatability of the same geometry using one fabric sample and to produce modular combinations of shapes, Geometry 1 will be produced four times and Geometry 2 will be produced once.

Fabric reuse

While multiple fabric samples will be used for the fabrication of the prototypes presented in Section 3.2.1, only one fabric sample will be used for this set of prototypes. This approach aims to test the reusability of the fabric by evaluating plastic deformation and the occurrence of defects. Investigating plastic deformation is crucial because it affects the load-bearing capacity and deformation behaviour of the fabric in subsequent uses. Development of defects, such as tears or unraveling, can significantly compromise the fabric's performance and durability. Understanding these factors is essential to determine the fabric's longevity, and practicality for repeated use in prefabrication applications. By examining these aspects, an informed decisions can be made about the feasibility of reusing the fabric.

3.2.3. Patterns and fabric fabrication

The fabric is produced using an industrial CNC flat-bed knitting machine (*Steiger Vega T 3.130*) available in the TU Delft Stevin II laboratory. The primary pattern that is used for all textile samples is the ”hexagonal” pattern as investigated in [16], due to its relatively balanced Poisson's ratio and Young's modulus compared to other knit patterns [16]. The pattern is shown in Figure 3.13. For the channels implemented in the fabric, an ”interlock” pattern is used.

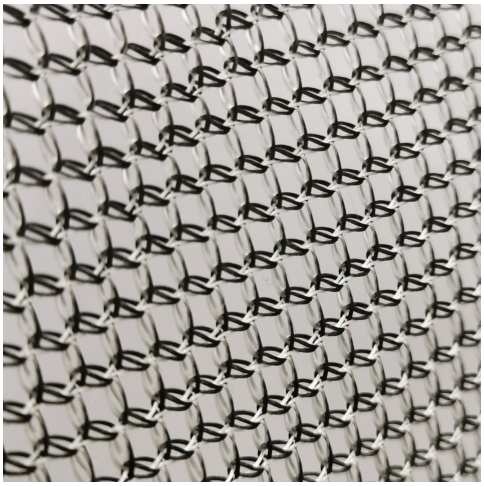

Figure 3.13: Hexagonal knit pattern used in the fabric samples

3.2.4. Plaster material

Throughout the physical prototyping, two different types of plaster materials are used. The first material, is a unreinforced mortar mix (M40) developed in [16] and the second material is a Strain Hardening Cementicious Composite (SHCC) as presented in [22], that utilizes PVA fiber reinforcement to provide tensile capacity.

An overview of the mixture compositions of both materials is shown in Table 3.1.

Material [kg/m^3]	M40	SHCC
Water	254	390
CEM III B	634	790
Limestone powder	-	790
PVA fibers	-	26
Superplasticizer	-	2.13
Fine aggregates 0.125 – 0.25 mm	88	-
Fine aggregates 0.25 – 0.5 mm	131	-
Fine aggregates 0.5 – 1 mm	263	-
Fine aggregates 1 – 2 mm	394	-
Fine aggregates 2 – 4 mm	701	-

Table 3.1: M40 mortar and SHCC mixture composition [16, 22]

The mixing procedures for the two mix designs are as follows:

M40 [16]:

1. Mixing of dry fine aggregates for 1 minute at low speed
2. Adding of cement powder and mixing for 1 minute at low speed
3. Gradually adding water and mixing for 2 minutes (1 minute slow, 30 seconds fast, 30 seconds slow)

SHCC [40]:

1. Mixing of cement powder and limestone powder for 1 min at low speed
2. Adding water and superplasticizer at slow mixing rate (superplasticizer already mixed in water)
3. Mixing at slow speed for 1 min and at high speed for 2 minutes
4. Adding fibers
5. Mixing for 2 minutes on high speed after fibers are added

For both mixing approaches, a *Hobart N50* mixer with a capacity of 5 liters is used. Furthermore, the plaster material is applied on the fabric within 15 minutes of completing the mixing process to prevent premature hardening.

The material properties of the SHCC, that are used in later analysis steps are shown in Table 3.2.

Density [kg/m^3]	E-modulus [GPa]	Compression f_c [MPa]	Tension f_t [MPa]
2025	18.5	63	3.5

Table 3.2: Mechanical properties of the SHCC material [22]

3.2.5. General fabrication workflow

Two different fabrication workflows of the prototypes will be tested throughout the study. The workflows consist of the following steps:

General workflow

1. Installation and tensioning of the fabric samples into the support frames
2. Mixing of the respective plaster material (according to 3.2.4)
3. Casting (plastering) of mortar onto the fabric formwork
4. Curing of prototype for 2 days
5. Demoulding of prototype

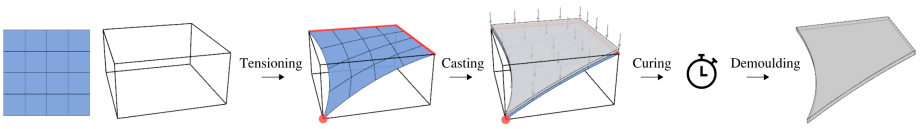

Figure 3.14: Visualization of the general fabrication workflow of the physical prototypes

Alternative workflow

1. Installation of the fabric samples into the support frames in flat configuration
2. Mixing of the respective plaster material (according to 3.2.4)
3. Casting (plastering) of mortar onto the flat fabric formwork
4. Tensioning fabric including mortar into final configuration
5. Curing of prototype for 2 days
6. Demoulding of prototype

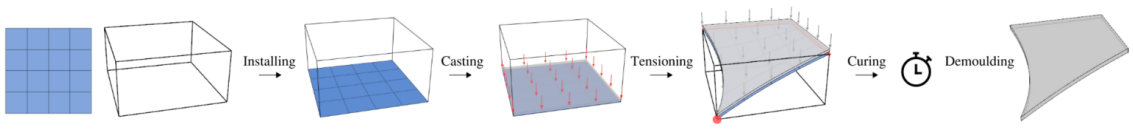

Figure 3.15: Visualization of the alternative fabrication workflow of the physical prototypes

In both fabrication workflows, the plaster material is applied on the fabric within 15 minutes of completing the mixing process to prevent premature hardening.

To restore the original geometry of the fabric samples, they are back-tensioned after demoulding and removal from the prototypes. The fabric is back-tensioned by inserting steel rods into two opposing channels and pulling them in opposite directions. This is done for both directions repeatedly until a uniform shape is achieved.

3.2.6. Geometrical analysis

Geometrical accuracy is essential for modular construction. Ensuring consistent geometries is of highest importance in prefabrication applications [34]. To comprehend and assess the effectiveness of the proposed design and fabrication method, the factors that contribute to its performance are analyzed.

3D scanning

Throughout this study, 3D scanning is used to capture the geometry of the built physical prototypes and fabric configurations, and to translate these into computationally analyzable geometry models. The 3D scanning is carried out using an *iPhone 15* and the application *Scanniverse*, which applies *photogrammetry* as a means of 3D scanning. *Photogrammetry* utilizes principles of optics to reconstruct dimensions and positions of objects by overlapping images. It thereby enables precise measurements of three dimensional objects using a phone camera [15]. Upon scanning, the 3D geometry models are exported as an *.obj* file and imported into *Rhino3D* for further processing and analysis.

Accuracy of repeated geometries

Accuracy plays a key role in the application of formworking systems, such as the one investigated in this research, for prefabrication and modular construction. As a measure of geometric accuracy for repeated geometries, the vertical alignment of two identical physical prototypes will be evaluated. The 3D scans, described in the previous paragraph, are imported into *Rhino3D*, then manually trimmed and processed to obtain the lower face of the prototype, which was supported by the fabric. This surface is more uniform than the upper, unsupported surface, making it more suitable for comparison. Employing the plug-in *Grasshopper* for *Rhino3D*, points in a regular grid are projected onto both surfaces to measure their vertical distances. The mean deviation of all points is then calculated as a measure of accuracy.

Contributions of tensioning and loading to fabric deformation

Understanding the influence of fabric pretensioning in the support frame and the vertical load from plaster material on its final deflection, and consequently the final geometry of the produced element, is crucial for the design of such elements and structures. While exact predictions of fabric behavior and deformation under specific loading are beyond the scope of this study, contributing factors are evaluated to gain insights into the complex behavior of the fabric. To quantify these contributions, changes in surface area will be measured and compared between unstressed fabric, fabric tensioned in the support frame, and tensioned fabric loaded with the self-weight of the plaster material. By comparing the surface area at each step, the contributions of tensioning and plaster weight to the total deformation can be evaluated independently. Similar to the evaluation of the accuracy of repeated geometries described in the previous paragraph, geometry models obtained through 3D scanning will be used for this analysis. The same computational framework, utilizing *Rhino3D* and its plug-in *Grasshopper*, will be applied to analyze the surfaces of the deformed textile. In addition to measuring the vertical deflection of projected reference points, the surface areas will also be measured from the 3D geometry models.

Exact values of the Young's moduli of the knitted textile and its various patterns are not yet available for comparison and are the subject of ongoing research.

3.3. Structural analysis of combined shapes

To evaluate the feasibility and performance of the physically found combined shapes, structural analysis is performed. In this section, the different steps and tasks that are performed in the context of the structural analysis are described.

3.3.1. Software and general modeling concept

For the structural analysis of the combined structures and preliminary form-finding, the FEA software package *RFEM6* by *Dlubal*, as well as the FEA tool *Karamba3D* [32] and the toolkit *Kangaroo Physics* [27] for *Rhino3D*'s *Grasshopper* are used. The individual applications of the three programs are described in the following paragraphs.

The combined structures will be modeled as doubly curved surfaces loaded by their self-weight. Each structure is supported by pinned point supports that restrict translational degrees of freedom in the x-, y-, and z-directions while allowing free rotation around these axes. Different approaches will be employed and investigated for the connections between individual elements of the combined structures. These connections will be modeled as continuously connected (hinged or rigid), or with a gap between elements, connected at each end of the interface edges by rigid links (in *RFEM6*) or springs (in *Karamba3D*). The latter approach simulates the behavior of the connectors presented in 3.2.2. By introducing gaps at the interfaces between the individual elements, the elements are structurally uncoupled from each other along the length of the interface edges, being connected only at the ends of the edges where the connectors are placed in the physical models. The modeling approach for the links is similar to the approach described in [7]. It should be noted that the realistic behavior of these connectors is highly non-linear, as they do not transfer tensile forces perpendicular to the edges, and their friction shear capacity is relatively low. However, for simplicity, the connections are modeled linearly, and non-linear effects are neglected. The FE calculations are conducted geometrically linear and follow first-order theory.

The combined structures are modeled at an approximate scale of 15:1 compared to the physically built prototypes to simulate the behavior and forces acting on a full-sized structure. Consequently, the individual elements have dimensions of approximately 4 x 4 meters with a thickness of 5 centimeters.

3.3.2. Form-finding of base geometries

In the structural analysis of the combined shapes, simplified geometrical representations of the actual base shapes shown in Figure 3.12 in 3.2.2 are used instead of 3D scans to streamline the models. To ensure these models approximate the physical geometries accurately, the shapes are form-found using the form-finding tool *Kangaroo Physics* within Grasshopper. For the form-finding process, the configuration of the fabric supported in the frame is manually drawn in Rhino3D, similar to the images shown in Figure 3.12. This configuration is then transferred as a mesh to the *Kangaroo Physics* plug-in and loaded with a downward force. Subsequently, the magnitude of the force is adjusted until a satisfactory geometry is achieved.

3.3.3. Mesh analysis convergence

Before the detailed structural analyses are conducted, the mesh analysis convergence is evaluated to ensure, that the created models are not overly sensitive to changes in mesh density. Through this analysis, the required mesh density is determined, which provides sufficient precision for the application in this study while not making the models and calculations unnecessarily heavy through too high numbers of mesh faces [26].

For this analysis, the convergence of the strain energy contained in the system is observed while increasing the number of faces of the mesh. Strain energy refers to the energy stored in a structure as it deforms in response to an applied load. The work done by internal forces during the deformation of the structure can be quantified as the integral of the stress over the corresponding strain within the material [35].

The strain energy stored in the system is calculated using *Karamba3D* in *Grasshopper*. The number of mesh faces is then gradually increased by increasing the UV-count of the meshing of the surfaces and both values, the mesh face count and the total strain energy are recorded and stored. Subsequently, the development of the strain energy will be plotted over the number of faces. From the plot, the number of mesh faces that provide sufficient convergence of the strain energy is read [26]. The mesh analysis is performed for the first combined structure that is being considered in this section. For the subsequently following combined structures, the mesh density resulting from this analysis is used and considered as sufficient.

3.3.4. Strain energy analysis and optimization

To study the mechanical behavior of shell structures, such as those created in this work, various metrics and factors can be observed and evaluated. To gain qualitative insights into the structural performance of the investigated structures, their shell behavior will be analyzed. The strain energy stored in the system is used as a metric to quantify the shell behavior of the structures. To determine the extent to which the structures act like a shell or a plate, the ratio between axial strain energy and total strain energy is calculated. A higher ratio indicates a greater share of forces carried through membrane action instead of bending action [19, 26].

In addition to analyzing the shell behavior, the bending strain energy of the structures itself is also evaluated. Since the structures discussed in this research are intended for the application of concrete and concrete-like materials with high compressive strength and low tensile and bending strength [30, 22], bending strain energy is a relevant additional metric to analyze. As the combined structures potentially allow for different configurations of the elements within one combination, they will be optimized for their structural performance. Two objectives are considered as measures of structural performance and optimized for individually: maximum axial strain energy ratio and minimum bending strain energy. The two respective optimal solutions are then compared. This approach is inspired by the structural morphogenesis method, which uses minimal strain energy as an optimization objective [39]. To optimize the structures, the geometries will, if applicable, be defined parametrically in *Grasshopper* to enable iterative manipulations. The optimization parameters that are manipulated for the optimization are the rotation angles between the connected elements. The solution space of the optimization of a combination is, therefore, the spectrum of buildable configurations provided by the rotation of the individual elements around their connected edges. Buildable means that no surface intersections resulting from the element rotations are allowed. Furthermore, only symmetric manipulations are considered. This means that if multiple elements are rotated, all elements are rotated by the same angle.

3.3.5. Analysis of deformations and internal stresses

The aforementioned analyses of the shell behaviour of the combined structures provide a qualitative understanding of their structural performance and enable the optimization of their configurations. To analyze the structural behaviour of the different configurations more in-depth, the internal stresses and resulting deformations of the structures are examined using the FEA software package *RFEM6* by *Dlubal*. *RFEM6* is used for an improved display of the results compared to *Karamba3D*.

In preparation for the FE-analysis in *RFEM6*, the geometry of the structures is modeled in *Grasshopper* and transferred to *RFEM6* via the *Grasshopper-RFEM6* interface. As result of the FE-analyses, the deformations and governing tensile stresses are produced. The tensile stresses are compared with the tensile capacity of the SHCC material (3.2.4) used in the physical prototypes. Due to the typically high and therefore not governing compressive capacity of concrete-type materials, the compressive stresses are not evaluated as part of this study.

4

Results

4.1. Physical prototyping

4.1.1. Evaluation of geometry exploration and tensioning methods

Fabric geometry and layout

To realize the anticipated geometries described Section 3.2.1, a square base layout for the fabric is chosen. Channels are implemented into the fabric to facilitate the insertion of cables and rods, to support and tension the fabric sample. Openings are placed at the corners and at the ends of the central channel to allow for easy insertion and removal of the rods and cables.

The target size of the fabric samples is 25 x 25 cm, to provide pre-stressing when the fabric is tensioned in the supporting frame of dimensions 30 x 30 cm. The fabric layout as well as the produced fabric sample are shown in Figure 4.1.

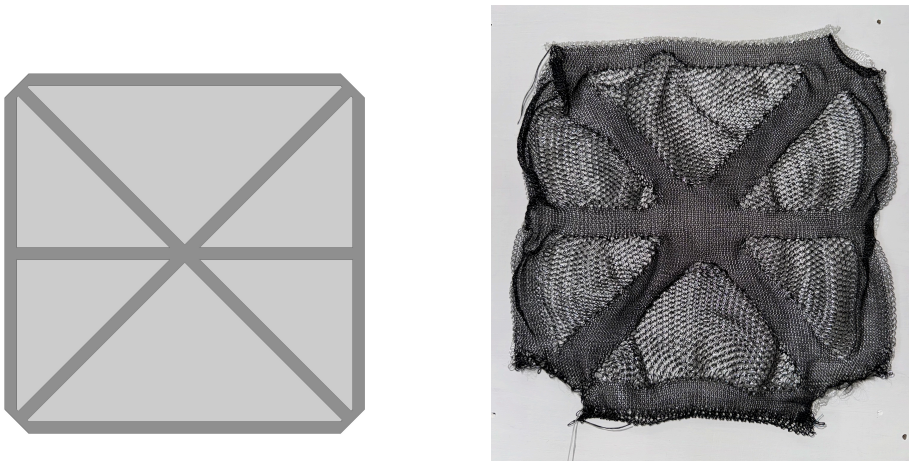

(a) (b)

Figure 4.1: Fabric sample used for evaluation of geometry exploration and tensioning methods: (a) Fabric layout and (b) produced sample

Frame design

Timber frames are constructed to serve as a supporting structure during the fabrication process. The frame set up is shown in Figure 4.2. Four frames are built, to allow for multiple prototypes to be cast simultaneously.

Through different pre-drilled holes in the timber columns, rods can be installed in the frame in different configurations. Besides the straight rods around the boundaries, that can be configured either as a

square, diagonal bars can be installed to either create a triangular base shape or, in case of a curved rod, tension the fabric upwards. Furthermore, by moving two of the columns further inwards, a rectangular geometry can be created.

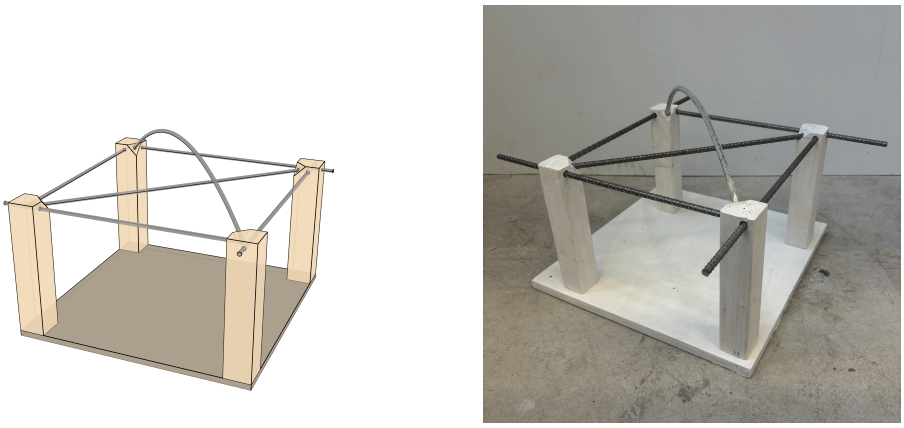

(a) (b)

Figure 4.2: Supporting timber frame used for evaluation of geometry exploration and tensioning methods: (a) Frame model and (b) built frame

Fabrication process

For the fabrication of the first set of geometries to explore the design spectrum of possible shapes, various tensioning methods and frame configurations were tested. The implementations of the anticipated test configurations shown in Figure 3.10 are depicted in Figure 4.3. These configurations successfully demonstrate the use of (a) bent rods, (b) cables, (d) straight rods, and (e) intermediate supports to create variations in pretensioning the fabric within the frames. Besides square base geometries, (c) triangular and (f) rectangular configurations were also realized.

The frame design has proven to be versatile, allowing for different fabric configurations and the implementation of the aforementioned pretensioning elements. However, installing the fabric presented some challenges. As the steel reinforcement bars are pushed through the fabric one after another during installation, the fabric becomes tensioned simultaneously. This prestressed state makes it quite difficult to insert the last bar through the fabric channel, requiring considerable force. Moreover, the rough and sharp texture of the reinforcement bars complicates the process of threading them through the tight channels.

Manually applying the mortar material by hand-plastering it onto the fabric poses difficulties in ensuring an even thickness of the applied layer. Due to the high flexibility of the fabric, significant deformation occurs during the mortar application, making it challenging to estimate the thickness accurately. This results in an uneven mortar distribution, which affects both the deformation of the fabric and the strength of the finished prototype.

Regarding the strength of the prototypes, the low tensile strength and brittleness of the M40 mortar material present issues for the handling of the finished prototypes. During the unmolding process, one prototype broke as the fabric was being removed, which shows the insufficient strength of the material.

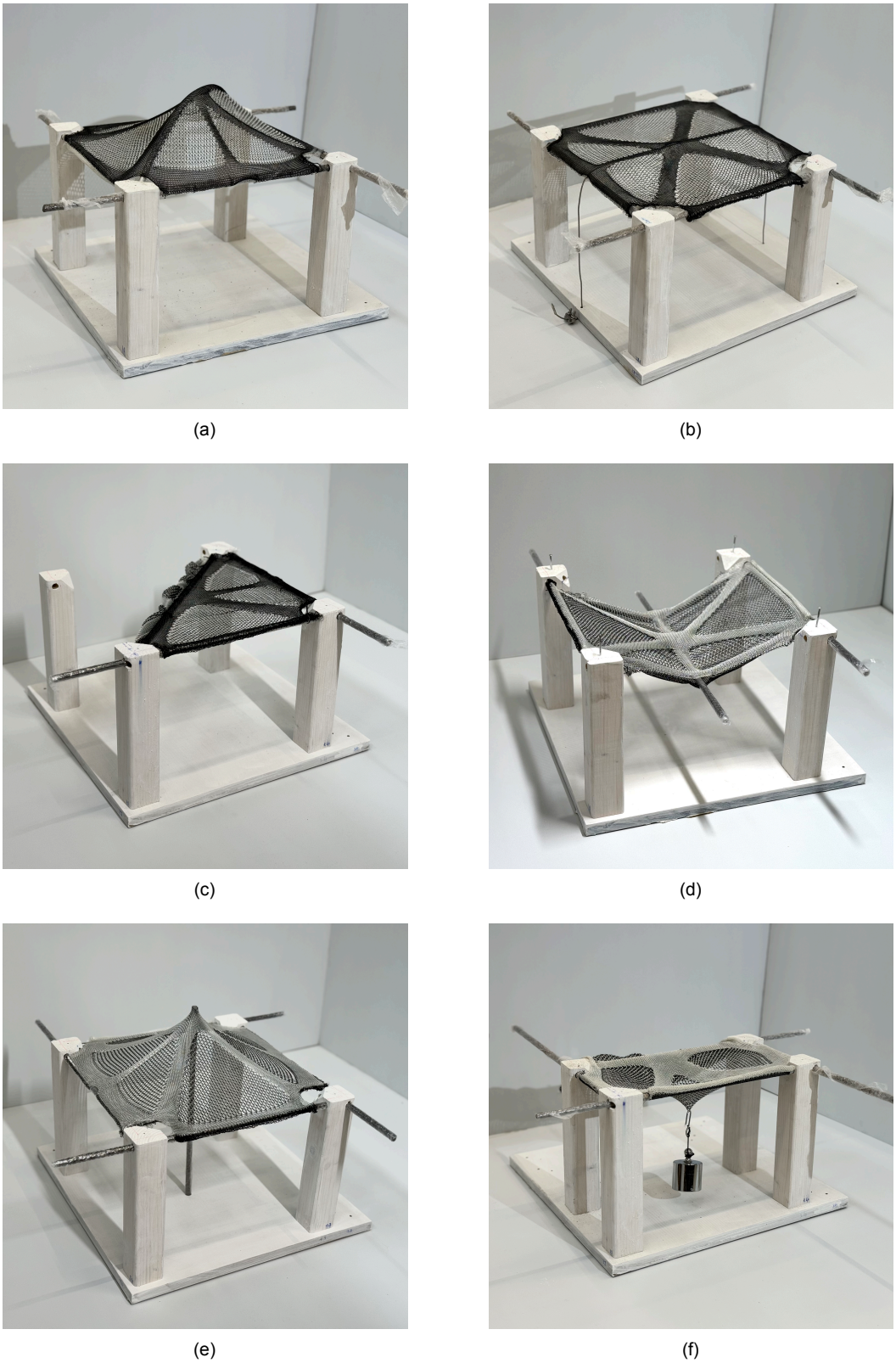

(a) (b)

(c) (d)

(e) (f)

Figure 4.3: Supporting frame and tensioning configurations of prototyping iteration 1: (a) Bent diagonal rod, (b) cable, (c) triangular, (d) straight rod and two free edges, (e) point support, (f) rectangular and point load (Photo credits: Anass Kariouh [17])

Finished prototypes

In Figure 4.4, the finished prototypes designed to explore possible geometries and tensioning methods are displayed. These prototypes demonstrate the successful realization of complex, doubly curved geometries across various typologies. The shapes exhibit diverse characteristics, including varying base geometries, articulated ribs, and different magnitudes of curvatures, among others.

One notable characteristic is the articulation of ribs resulting from the channels implemented in the fabric samples used. Specifically, the prototypes in Figure 4.4 (b) and (d) feature prominent ribs running diagonally between the corner points. This rib articulation is attributed to the higher stiffness of the knit pattern used in the channels compared to the surrounding fabric. The increased stiffness means that, under uniform stress, the fabric in the channels deforms less than the adjacent areas. This difference in deformation creates the ribbed surface observed in the prototypes. This phenomenon has potential for the use as a structural feature, potentially improving the stiffness and load transfer of the structures. By intentionally implementing channels or pattern variations with higher stiffness, the formation of ribs can be controlled and potentially used to create stiffening ribs that follow the flow of forces of the structure.

However, while the implementation of channels offers significant design potential, it also limits the fabric's versatility for use in structures with different geometries. Although ribs can be a desirable structural and aesthetic feature, they may have the opposite effect if a smoother surface is desired or if the rib formation is structurally unfavorable. Consequently, the use of channels or pattern variations restricts the design space to structures featuring ribbed or rib-like elements and does not allow for smoothly curved shapes. Therefore, an alternative approach to using channels to implement pre-stressing elements will be explored in the fabrication of the prototypes in Section 4.1.2.

Due to the support of the steel reinforcement bars in holes drilled into the timber columns, the corners of the fabric elements had to be cut out to prevent resting on or interfering with the columns. In configurations with released and unsupported edges, this results in an entire strip approximately four centimeters wide being almost entirely unsupported. This effect is visible in Figure 4.4 (d), where the unsupported edges deform significantly more than the center part of the fabric.

It should be noted that the inherent orthotropy of the fabric stiffness, along with the variance in stiffness between the channels and the remaining fabric, results in shapes that cannot be directly compared to hanging models such as those by Isler, Otto, or Gaudi [3]. Although the curved geometry of the elements enhances their structural performance by increasing the share of forces transmitted through membrane action rather than bending action, the resulting shapes do not translate into compression-only forms when the final element is flipped upside down following the principle of the catenary that is applied in the above mentioned examples.

(a) (b)

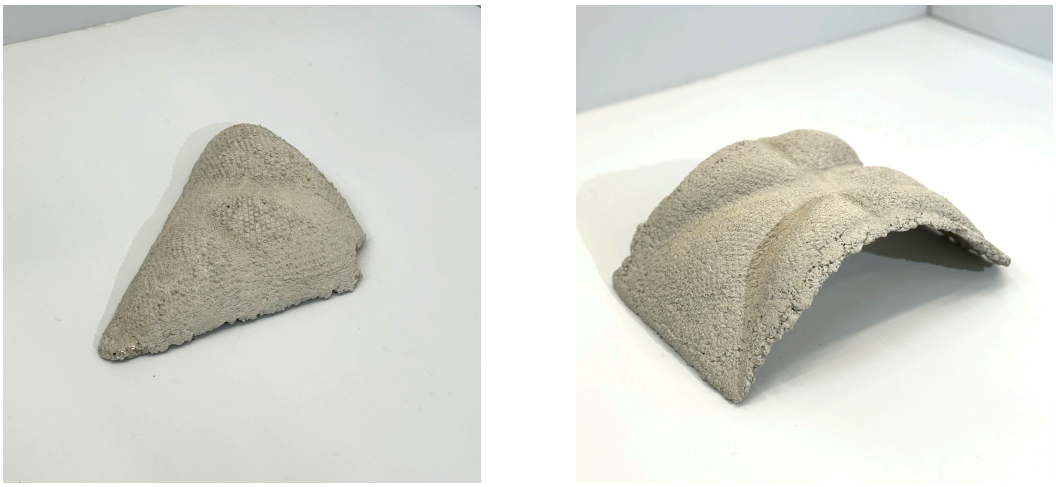

(c) (d)

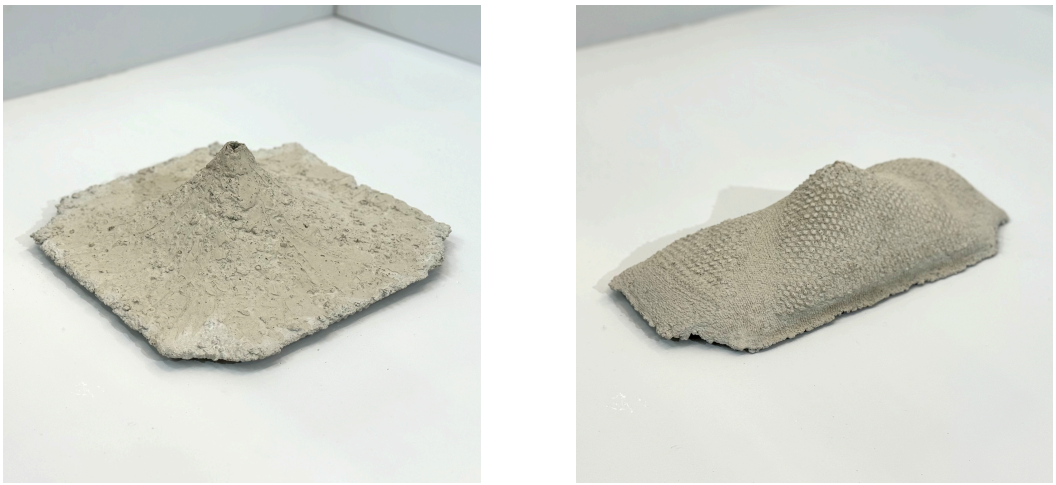

(e) (f)

Figure 4.4: Finished prototypes of prototyping iteration 1: (a) Bent diagonal rod, (b) cable, (c) triangular, (d) straight rod and two free edges, (e) point support, (f) rectangular and point load (Photo credits: Anass Kariouh [17])

4.1.2. Evaluation of repeatability and modular combinations

Fabric layout

The fabric layout for this set of geometries differs slightly from the fabric layout presented 3.2.1. The fabric has a base shape of approximately 26 x 28 cm, but has no channels crossing in diagonal or transversal direction. As opposed to the first fabric layout, the corners are closed and have openings on the sides to allow for the insertion and the removal of the supporting rods while being supported until the corner of the fabric.

The fabric layout as well as the produced sample are shown in Figure 4.5

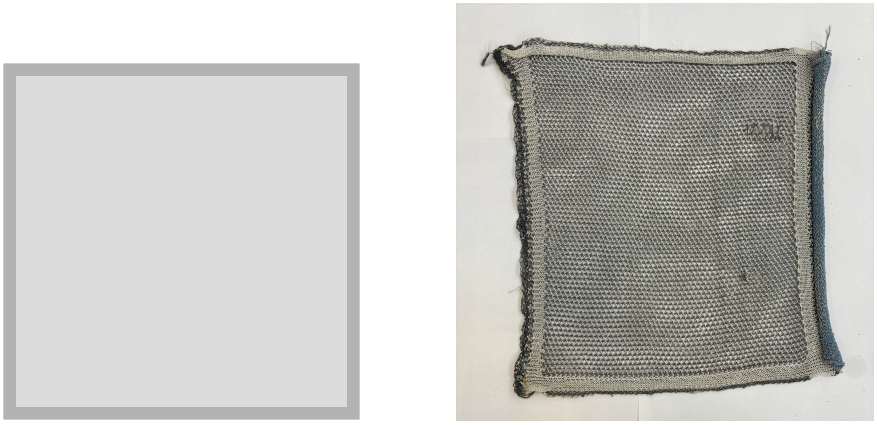

(a) (b)

Figure 4.5: Fabric sample used for evaluation of repeatability and modular combinations: (a) Fabric layout and (b) produced sample

Frame design

The frame setup (Figure 4.6 (a)) for fabricating the aforementioned set of prototypes is designed to offer greater adaptability and flexibility in configurations. The frame consists of four individual aluminum columns with steel baseplates, aluminum laboratory clamps and support steel rods with 3D printed PLA (polylactic acid) connectors. Due to the four individual steel base plates, the columns can be positioned independently from each another. The height-adjustable laboratory clamps thus allow the four corner points to be positioned freely anywhere in the space (Figure 4.6 (b)). Furthermore, the frame provides the option to either install supporting steel rods to continuously support the fabric (Figure 4.6 (c)) or to point-support the fabric directly on the lab clamp using a steel hook (Figure 4.6 (d)). However, It has to be noted, that for different set-ups with multiple steel rods, different 3D printed PLA connectors might be needed in order to accommodate the respective angle between the steel rods. For the two types of prototypes built using this frame, connectors were made for a 90° angle and a 75° angle.

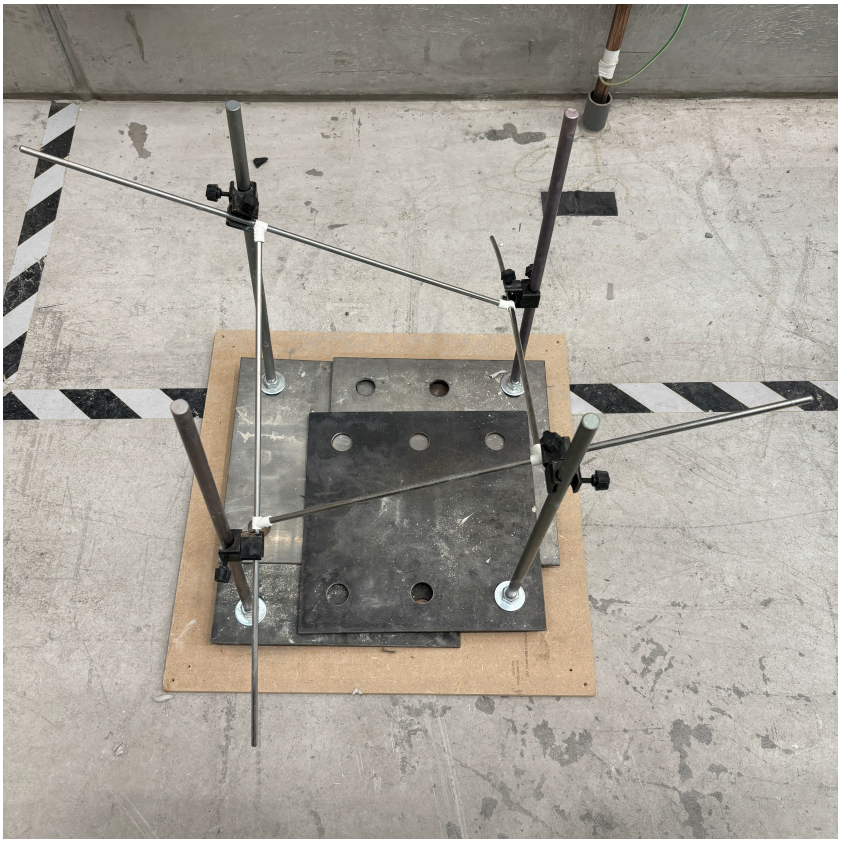

(a)

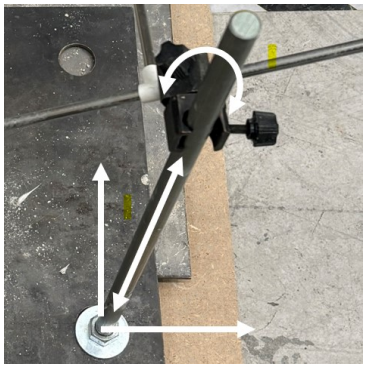

(b)

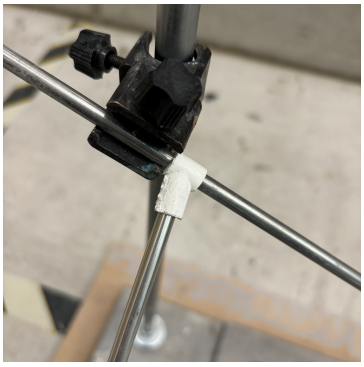

(c)

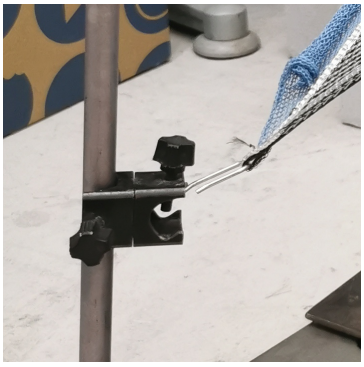

(d)

Figure 4.6: Supporting steel-aluminum frame used for evaluation of repeatability and modular combinations: (a) Assembled frame, (b) degrees of freedom per corner support, (c) 3D printed PLA connection piece and supporting rod, (d) point support

Fabrication process

In this section, the two different fabrication approaches that were applied are evaluated. Figure 4.7 illustrates the fabrication workflow used for the prototypes of *Geometry 1* and *Geometry 2*. Figure 4.8 depicts the alternative fabrication workflow implemented for the prototype of *Geometry 3*.

Compared to the fabrication of the first set of prototypes described in Section 4.1.1, the improved flexibility of the steel-aluminum frame significantly simplifies the installation and removal of the fabric and prototype from the frame. During the unmolding process, the steel bars supporting the fabric can be easily removed by opening the laboratory clamps and lifting the prototype, including the fabric and steel bars, out of the frame. Subsequently, the steel bars can be detached without any difficulty or damage to the fabric, as both the steel rods and fabric are no longer under stress once the structure is removed from the frame. After removing the steel bars, the fabric can be easily pulled off the element

without any damage.

While the aluminum columns in the current frame setup were manually threaded and connected to individual steel plates as footings, the design could be improved by using more precisely fabricated columns and a continuous baseplate, allowing flexible positioning of the columns. Additionally, the 3D printed elements used to connect the steel rods in the current setup have rigid angles, requiring individual connectors for configurations needing angles other than 90° or 75°. This issue could be resolved by incorporating a hinge into the connectors, which would involve a slightly more complex design.

As previously mentioned in the fabrication of the elements in Section 4.1.1, controlling the thickness during the application of the SHCC plaster material remains a challenge. Due to the high flexibility of the fabric and the doubly curved surface of the tensioned fabric, the thickness of the applied mortar layer can only be approximately controlled by manually spreading it evenly on the fabric.

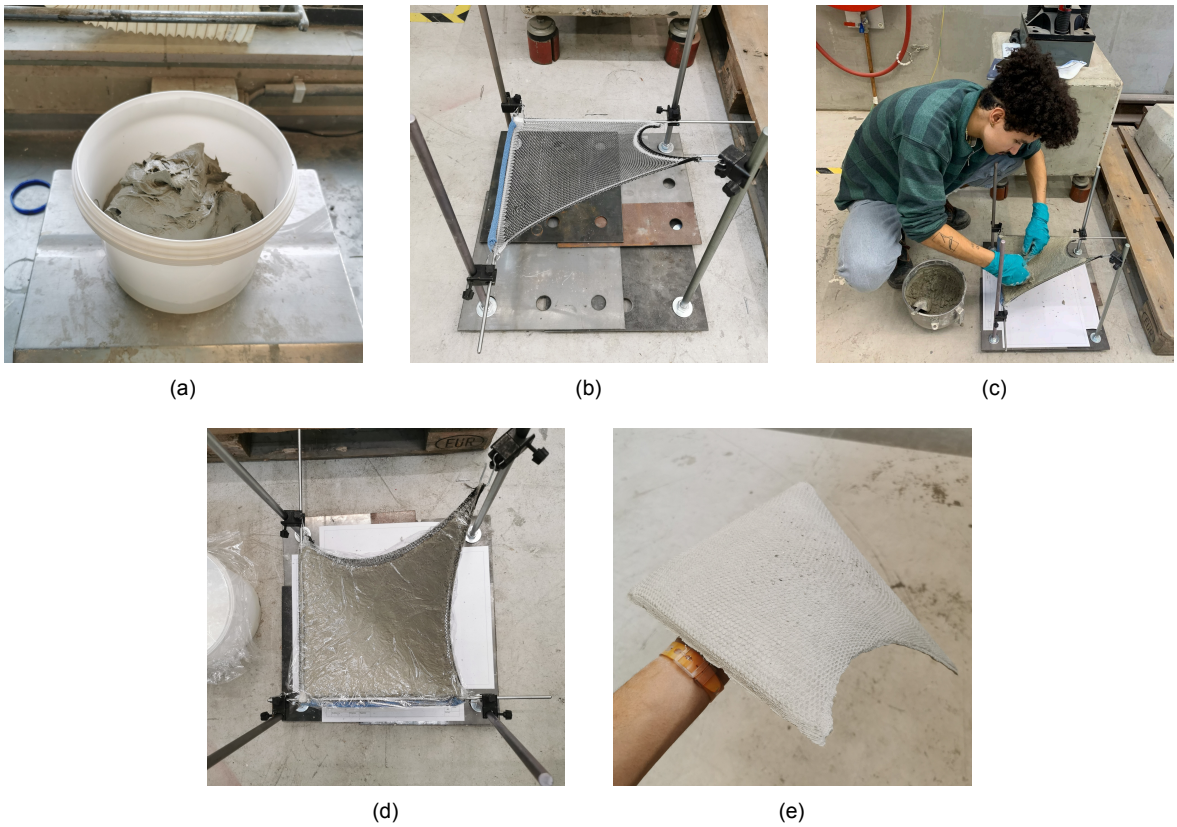

Figure 4.7: Fabrication of prototypes using the general fabrication workflow: (a) SHCC mix, (b) tensioning of the fabric, (c) casting, (d) curing, (e) demoulding

To reduce the inaccuracy in thickness control during the aforementioned fabrication process, an alternative workflow has been applied, as depicted in Figure 4.8. Instead of applying the mortar onto the fabric while it is tensioned in place, the mortar is applied to the fabric in a flat configuration, with continuous support provided by a wooden plate underneath (Figure 4.8 (d)). After evenly spreading the mortar, the fabric is lifted into its final position by moving the laboratory clamps upwards (Figure 4.8 (e)) and tensioning the pre-installed cable (Figure 4.8 (f)). The flat and even surface of the underlying wooden plate ensures a more uniform distribution of the mortar on the fabric.

However, lifting the fabric into its desired configuration presents challenges in precisely adjusting the laboratory clamps to achieve the intended shape. In the previous workflow, the exact configuration could be established before applying the mortar, whereas in this approach, adjustments need to be made with the mortar already in place. Additionally, due to the deformation of the fabric when lifting

and tensioning it, extra mortar needs to be added at the edges where the fabric was supported, as the initial sagging causes the mortar layer to shift inward.

Besides improving thickness control, the alternative fabrication approach also tested implementing a cable into the structure without a designated channel in the fabric. As shown in Figure 4.8 (b), the cable is threaded through the fabric at the supported edges and in the center to hold it in place and ensure precise positioning. This approach, which does not require a channel to feed the cable through, proved successful. The cable remained securely in its designated position and was easily removable during the demolding process.

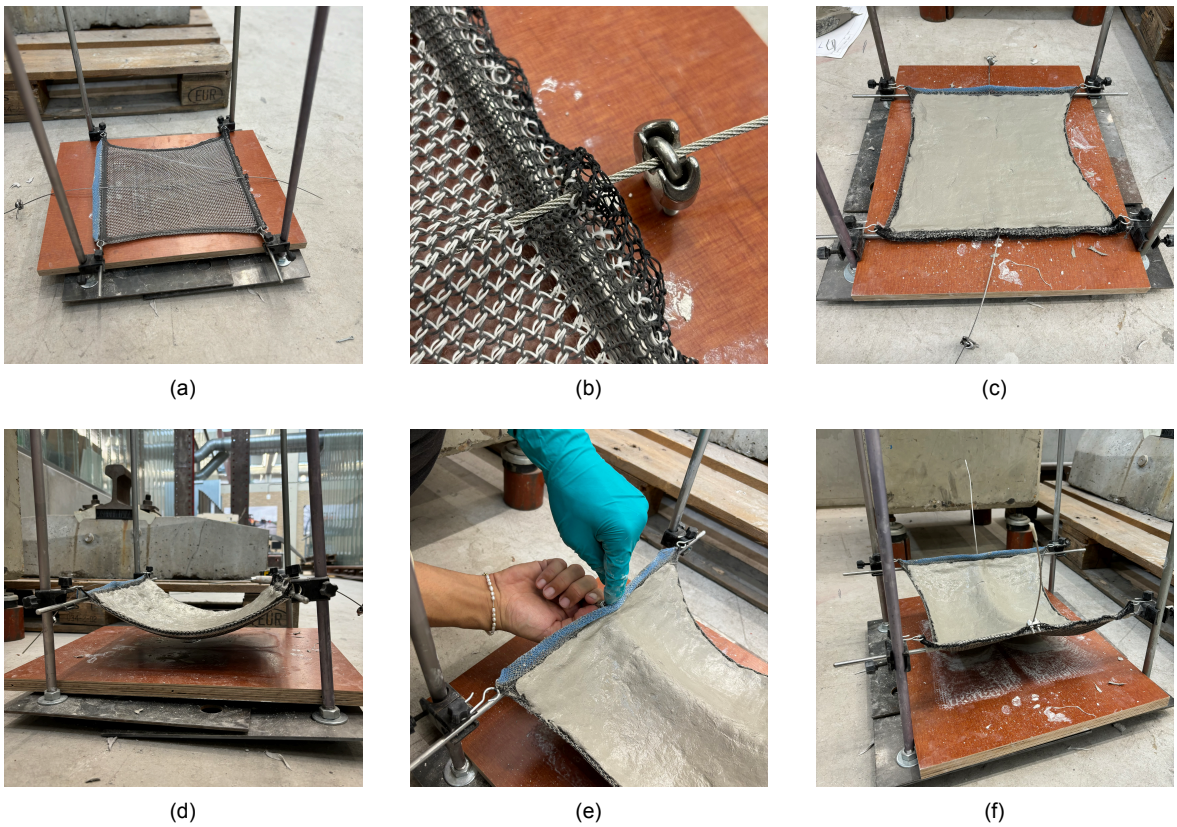

(a) (b) (c)

(d) (e) (f)

Figure 4.8: Fabrication of prototype using the alternative fabrication workflow: (a) Fabric installation, (b) implementation of cable, (c) casting flat on underlying plate, (d) lifting of supports, (e) tensioning of cable

Finished prototypes

In Figure 4.9 and Figure 4.10, the finished prototypes of Geometries 1, 2, and 3 are displayed. These prototypes demonstrate the successful construction of doubly curved structures with various boundary and tensioning configurations. The prototypes illustrate that, using the previously described methods, it is possible to construct structures with both line and point supports, in-plane and out-of-plane, with and without the use of cables, while reusing the same fabric sample and supporting frame for fabricating all elements.

In Figure 4.9, the finished prototypes of *Geometry 1* are shown. The leftmost prototype in Figure 4.9 (a) is made from the M40 mix, while all other prototypes are made from the SHCC mortar mix. Due to the fabric's asymmetry and orthotropic stiffness properties, the prototypes are not symmetric, as observed in Figure 4.9 (d). The surface of the prototypes, which has been supported on the fabric, clearly exhibits the fabric pattern imprinted in the surface, creating an interesting surface finish and texture. Additionally, the distorted pattern geometry of the fabric is visible in the texture. In areas where the fabric is predominantly tensioned uniaxially, the pattern geometry appears skewed and distorted. In contrast, in areas with more biaxial tension, the pattern remains even and uniform. This characteristic of the surface texture, resulting from the fabric formwork, offers potential for future research into ret-

rospective analysis of the internal fabric stresses inferred from the pattern geometry imprinted on the finished elements.

In Figure 4.9 (d), the surface finish and quality resulting from the two different mixes, M40 (on the left) and SHCC (on the right), can be compared. The surface finish (of the side with no fabric contact) of the prototypes using the SHCC mix is visibly smoother and more uniform compared to the prototypes using the M40 mix. Additionally, the edge finishing of the SHCC elements, shown in Figure 4.9 (c), is much smoother compared to the M40 mix. The SHCC mix, due to its fiber reinforcement and increased ductility, allows for a lower thickness in the prototypes compared to the M40 mix. The M40 prototypes displayed high fragility and brittleness at an approximate thickness of 1 cm, which led to the breaking of one prototype during the removal of the fabric, as discussed in Section 4.1.1. In contrast, the SHCC prototypes demonstrated much higher sturdiness and improved handling, even at a lower thickness of between 5-8 mm.

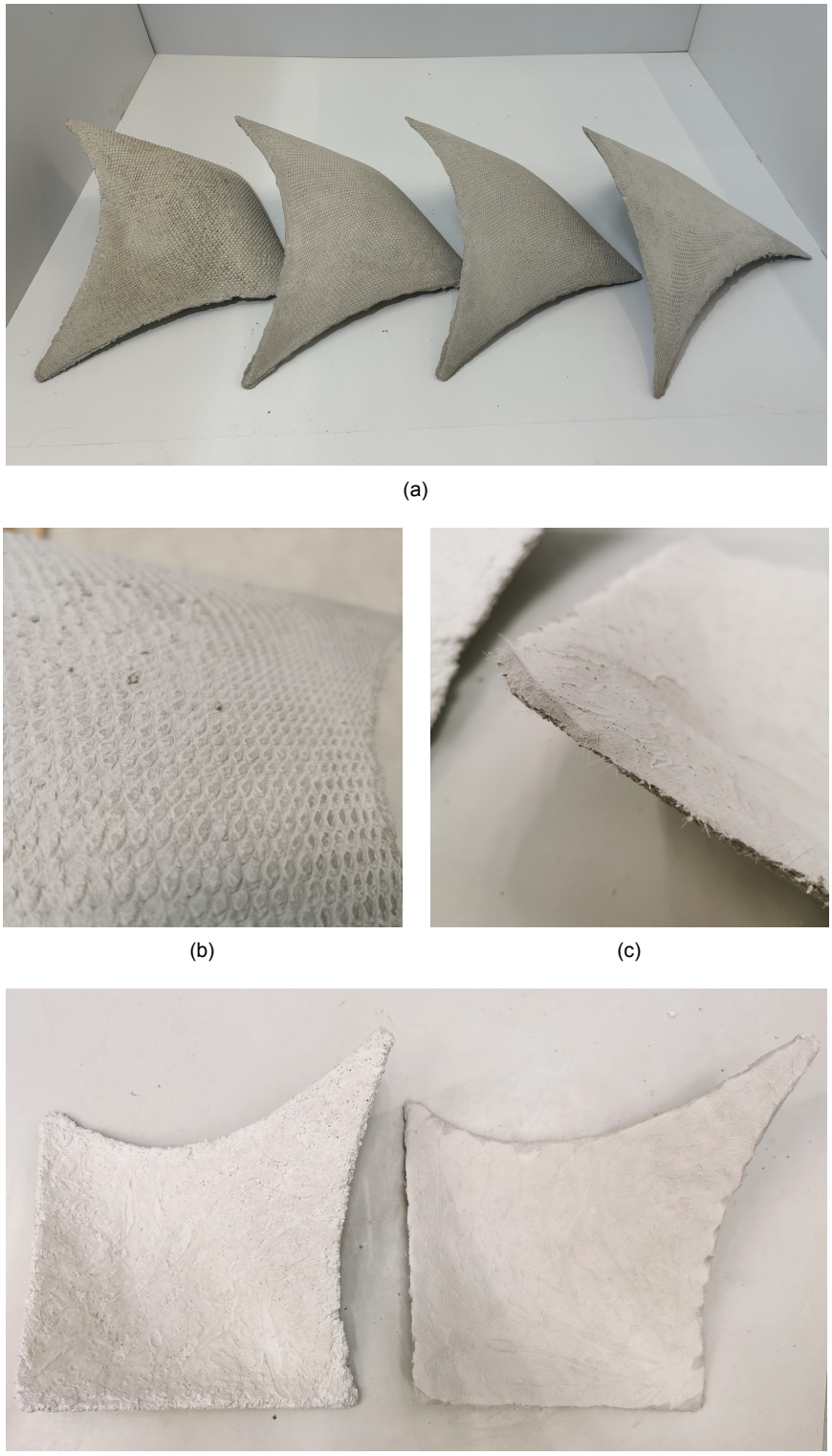

(a)

(b)

(c)

(d)

Figure 4.9: Finished prototypes of prototyping iteration 2: (a) Finished prototypes of Geometry 1, (b) surface quality, (c) edge quality, (d) M40 mix (left) & SHCC mix (right)

As mentioned in the previous fabrication section and shown in Figure 4.8, implementing the cable without a designated channel in the fabric was successful during the fabrication of the prototype of Geometry 3. This approach also proved effective in the finished prototype. The cable created a sharp

crease in the structure, dividing it into two sides as intended (Figure 4.10 (b)). Compared to the prototype shown in Figure 4.4 (b), which used a cable supported in a channel, the prototype of Geometry 3 demonstrates comparable results. This confirms the feasibility of including a cable as a prestressing member by threading it through the fabric itself, without the need for a dedicated channel.

Furthermore, the new fabric layout, which supports the full corners of the fabric, shows a significant improvement over the previous layout in Section 3.2.1, where the corners were cut out. In both of the prototypes shown in Figure 4.4 (d) and Figure 4.10 (b) (Geometry 3), two opposing edges are unsupported. However, in the prototype of Geometry 3, the two supported edges include the corners, whereas, in the prototype shown in Figure 4.4 (d), the corners were unsupported due to the fabric cutouts. The fully supported corners result in a much smoother and more evenly curved edge compared to the prototype with cut-out corners.

(a) Geometry 2 (b) Geometry 3

Figure 4.10: Finished prototypes of prototyping iteration 3: (a) Geometry 2 and (b) Geometry 3

Fabric reuse

In Figure 4.11, the fabric and its defects and plastic deformation after multiple reuse are shown. Upon fabrication of the fabric sample, the sample exhibited an initial defect, that is shown in Figure 4.11 (a). During the knitting, a needle missed a loop, which results in a ”free” loop, that is not secured in the fabric and which can cause the fabric to unravel. Defects like this one pose the risk of creating larger holes in the fabric over time. Despite this risk, the fabric sample with the initial defect was used, as these defects are possible in a realistic setting and therefore relevant to evaluate. In Figure 4.11 (b) the same defect is shown after reusing the fabric sample to fabricate a total number of six prototypes. Against the initial expectation, the defect did not propagate further through the fabric sample. Instead, the individual fibers of the yarn frayed, which appears to block the free loop from unraveling further, inhibiting the defect’s propagation. It can be concluded, that initial defects such as missed loops and initial points of unraveling do not pose a significant risk for fabric reuse.

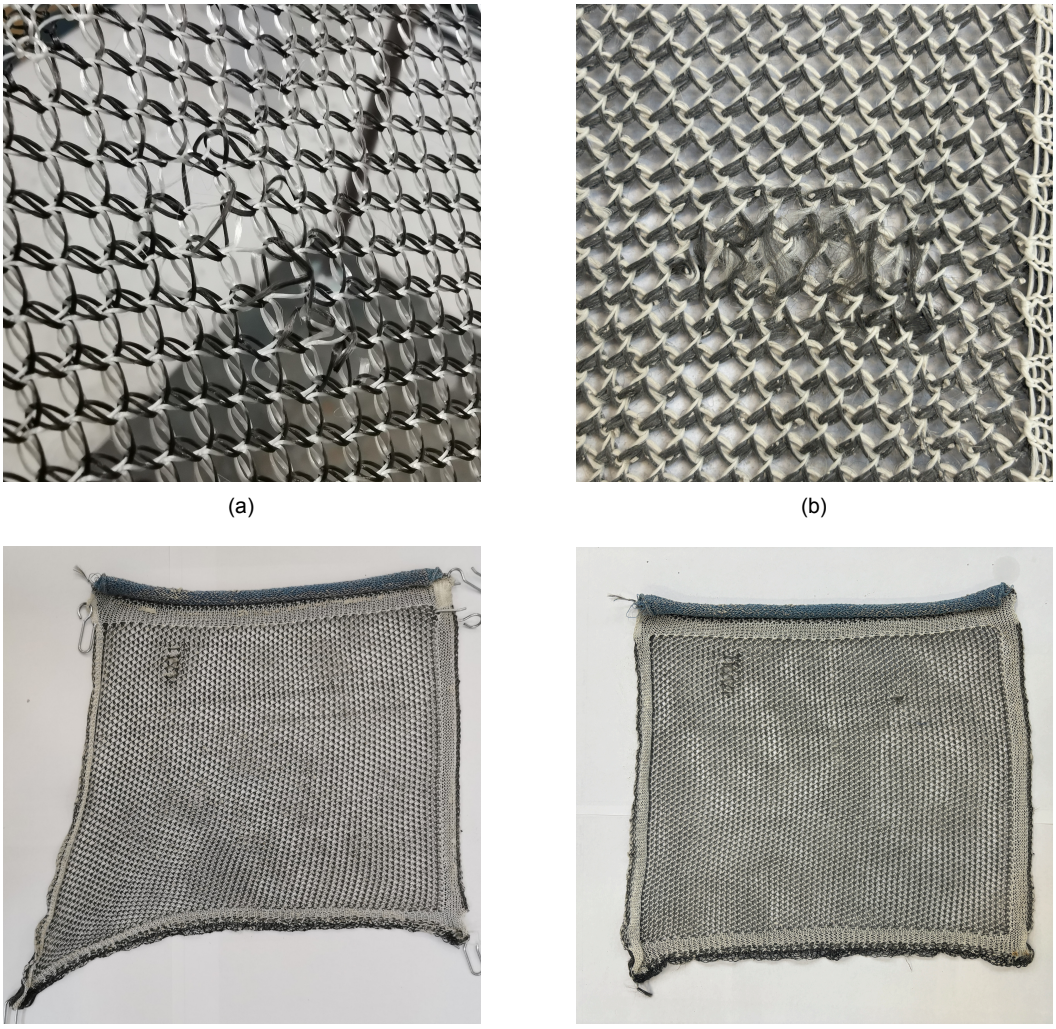

(a) (b)

(c) (d)

Figure 4.11: Fabric reuse: (a) initial defect, (b) defect after the fabrication of six prototypes, (c) deformed fabric after casting four identical prototypes, (d) fabric after tensioning it back into its original shape

Besides defects, plastic deformations are observed in the fabric after multiple reuse. Figure 4.11 (c) shows the fabric sample immediately after using it for the fabrication of four prototypes of *Geometry 1*. The fabric had been tensioned in the frame configuration shown in Figure 4.7 (b) for more than two weeks. The fabric sample exhibits significant deformation in the bottom left corner, resulting from being strongly tensioned upwards and maintained in that position for an extended period of time. In Figure 4.11(d), the fabric is shown after manually tensioning it back into a rectangular shape by pulling on the edges and ”massaging” the fabric to propagate the deformation back to its original shape. Despite initial significant plastic deformation from reuse, it is feasible to restore the fabric to its original shape. This can be attributed to the deformation stemming from distortion of the knit pattern geometry rather than plastic deformation of the yarn or fibers themselves. Therefore, it can be concluded that plastic deformation of the fabric can be reversed to a certain extent, restoring the fabric’s initial properties.

(a) (b)

Figure 4.12: Fabric reuse: Asymmetry of the prototype due to plastic deformation of the fabric after multiple reuse

While the fabric's original geometry can be mostly restored, some plastic deformation remains. Figure 4.12 shows a prototype of symmetric geometry (*Geometry 3*) built after fabricating four prototypes of *Geometry 1* and re-tensioning the fabric, restoring its original rectangular shape. Despite the symmetrical fabrication setup of the frame, the resulting prototype is slightly asymmetrical. In Figure 4.12 (a), the prototype is visibly skewed in the bottom left corner, coinciding with the large deformation of the fabric seen in Figure 4.11 (c). Additionally, the left side, where the skewed corner is, shows slightly higher deformation than the right side. However, considering that the process of restoring the fabric's original shape has potential for improvement in future research, it can be concluded that the effects of plastic deformation on the prototype's resulting geometry are minimal.

Resulting combined geometries

Exploring modular combinations of the created shapes is one of the key aspects of this section. To provide the necessary means of connecting individual prototype elements to each another, reversible connectors have been designed. A center piece (Figure 4.13 (a)), that allows up to four corner points of the elements to be connected and edge connectors (Figure 4.13 (b)), to connect the straight interface edges to each another.

Structurally, the combined systems rely on interlocking of the individual elements with each another. Through the connectors shown in Figure 4.13, the individual elements are held in place and can transfer forces. The forces to be transmitted through the connectors are predominantly compressive forces, out-of-plane shear forces and in-plane friction shear forces. Furthermore, the flanges of the connectors create a clamping effect, allowing moments to be transmitted to a limited extent. However, due to the low strength of the 3D printed material and the limited anchoring depth of the connectors on the element surfaces, this effect is minimal and negligible.

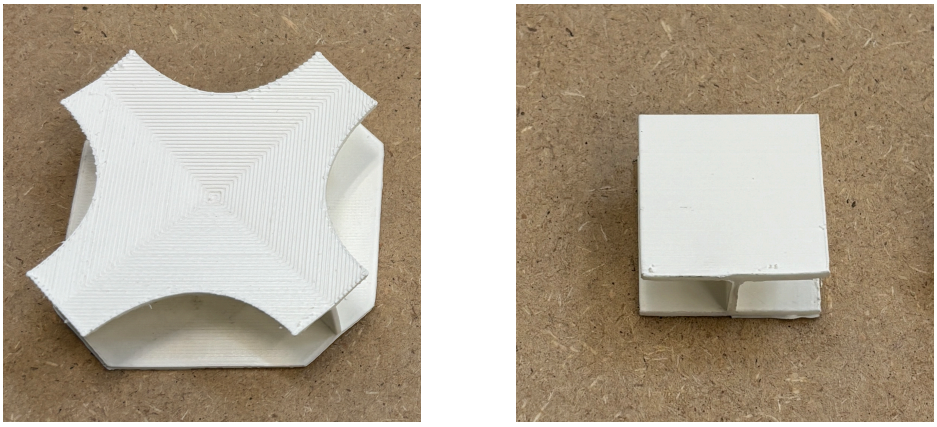

(a) (b)

Figure 4.13: 3D printed connectors for the assembly of combined shapes: (a) Center piece and (b) edge connector

In the following paragraph, the shapes that that arose from manually combining the previously built and presented prototypes are presented. Combinations of two, three, four, and five prototype elements were created. Figure 4.14 shows the combined structures that exclusively consist of prototypes of *Geometry 1*, while Figure 4.15 shows those, that incorporate prototypes of both *Geometry 1* and *Geometry 2*.

Combination 10 (Figure 4.14 (b)) shows the realization of the anticipated composed structure, that was inspired by the geometries shown in Figure 3.11 in Section 3.2.2, that served as a reference. The structure consists of four prototypes of *Geometry 1*, that are connected to each another at their straight edges and supported on the four elevated corner points. The elements are positioned upside-down compared to their fabrication configuration in the frame, as shown in Figure 4.7 (d), with all straight edges aligned in one plane. In the center of the structure, where the corner points of all four elements come together, they are connected through the 3D printed center piece (Figure 4.13 (a)). Additionally, at the ends of each connected straight edge, the elements are secured in place by an edge connector (Figure 4.13 (b)).

Combination 8 (Figure 4.14 (a)) and *Combination 6* (Figure 4.14 (c)) consist of three prototypes of *Geometry 1*, with different orientations of the top element. Instead of using edge connectors, *Combinations 8* and *6* rely on interlocking at three connecting corner points. The two bottom elements each rest on two of their corner points and lean against each other at the central corner point, connected through the center piece. The third element is supported by the two bottom elements, with the center piece preventing it from sliding downwards, and its lateral corner points resting on the upper corner points of the supporting elements. Stability is achieved by positioning the center of gravity of the top element beyond the lateral corner points, away from the supporting elements. This causes the top element to hinge around the axis between the two lateral corner points resting on the bottom elements. The center piece prevents the top element from rotating around that axis by keeping the central corner point in place. *Combination 4* (Figure 4.14 (e)) consists of two prototypes of *Geometry 1* and resembles *Combinations 8* and *6*, but without the top element.

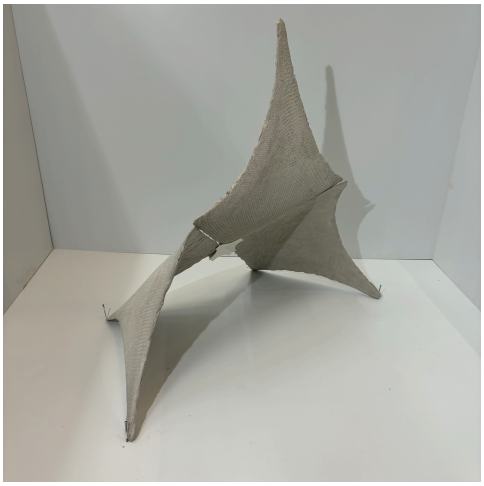

(a) Combination 8

(b) Combination 10

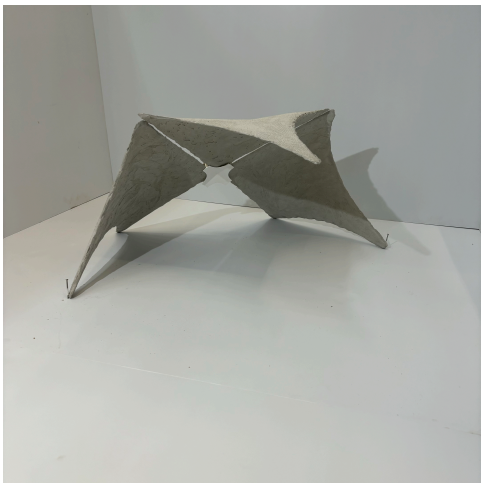

(c) Combination 6

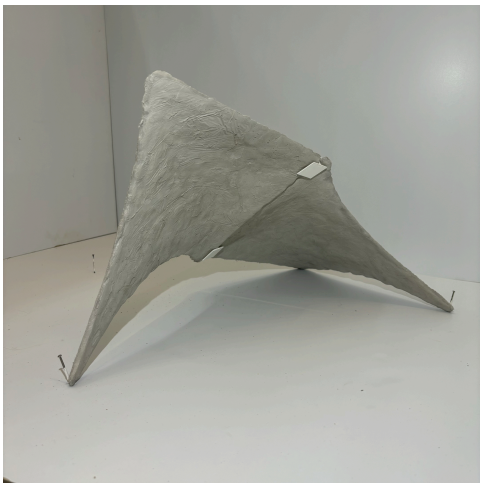

(d) Combination 5

(e) Combination 4

(f) Combination 7

Figure 4.14: Combined shapes composed of Geometry 1 prototypes: (a) Combination 8, (b) Combination 10, (c) Combination 6, (d) Combination 5, (e) Combination 4, (f) Combination 7

Combination 5 (Figure 4.14 (d)) and *Combination 7* (Figure 4.14 (f)) each consist of two elements

of *Geometry 1*, connected through edge connectors. In *Combination 5*, one element rests with two corner points on the ground, supporting the edge of the other element. In *Combination 7*, an additional column supports the structure at the backward corner (not visible in the figure). In both combinations, the elements are connected through edge connectors at opposing straight edges.

Combination 2.1 (Figure 4.15 (a)) and *Combination 2.2* (Figure 4.15 (b)) each consist of four elements of *Geometry 1* and one element of *Geometry 2* in the center. Since the *Geometry 2* element is centrally located in both combinations, no center piece connector is used. The structures are supported solely on the elevated corner points of the four *Geometry 1* elements. The *Geometry 2* element is entirely supported by the surrounding *Geometry 1* elements to which it is connected through edge connectors. In *Combination 2.1*, the central *Geometry 2* element is oriented with its primary curvature pointing upwards. In *Combination 2.2*, the *Geometry 2* element is flipped and rotated 90°, resulting in its primary curvature pointing downwards.

Combination 19 (Figure 4.15 (c) and (d)) consists of two supporting elements of *Geometry 1* and one central element of *Geometry 2*. In this structure, the *Geometry 1* elements rest on the ground with two corner points each, supporting the horizontally oriented *Geometry 2* element through edge connectors on their straight edges.

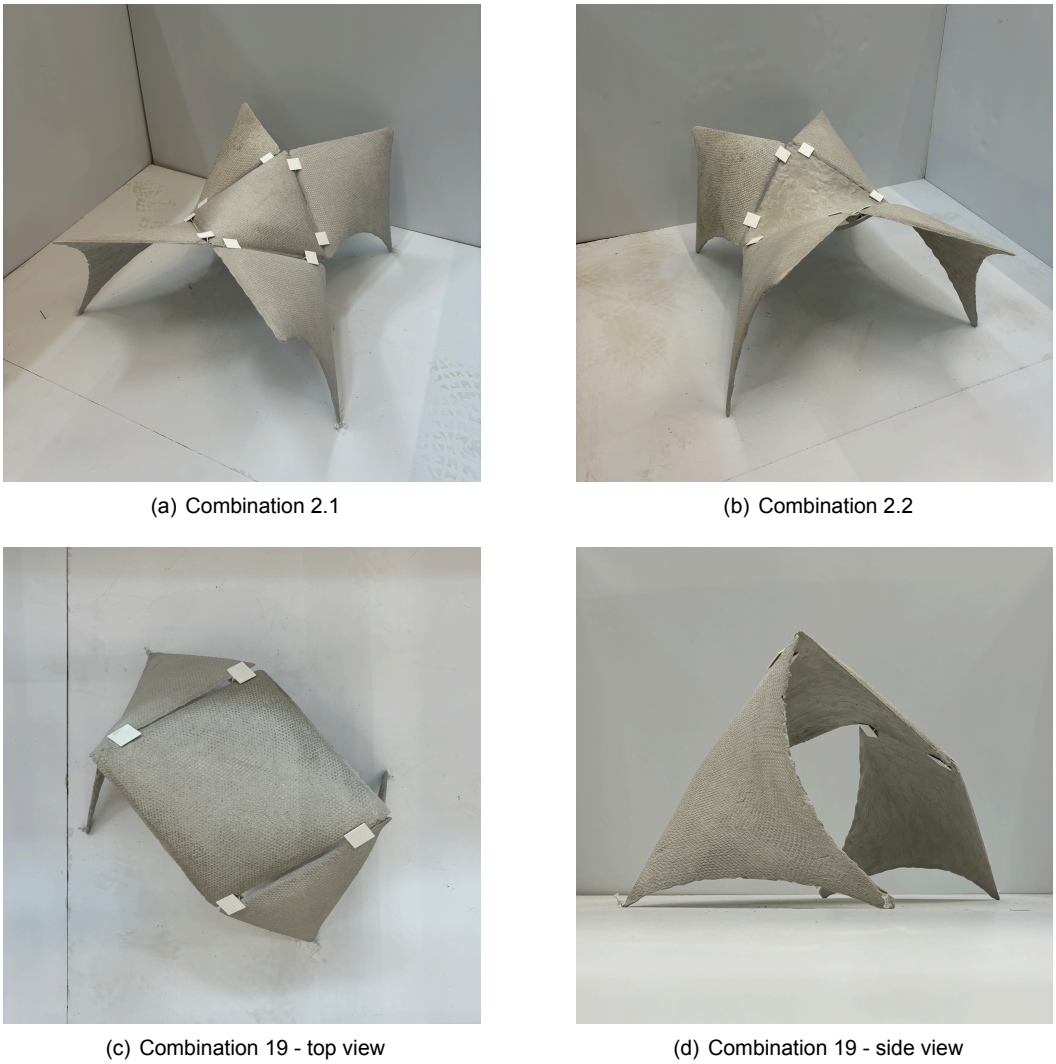

(a) Combination 2.1

(b) Combination 2.2

(c) Combination 19 - top view

(d) Combination 19 - side view

Figure 4.15: Combined shapes composed of Geometry 1 and 2 prototypes: (a) Combination 2.1, (b) Combination 2.2, (c) and (d) Combination 19

4.1.3. Geometrical analysis

3D scanning

Figure 4.16 presents the 3D scans of two prototypes of *Geometry 1* ((a) and (b)), and the tensioned fabric (c) and the tensioned fabric loaded with the SHCC plaster material (d) of *Geometry 2*. These scans provide a detailed visual representation of the geometries, which are used for further analysis in the subsequent paragraphs. The scans allow for precise comparison and evaluation of the deformation and surface characteristics of each prototype, offering valuable insights into the effects of tensioning and casting processes on the resulting structure and accuracy of the fabricated geometries.

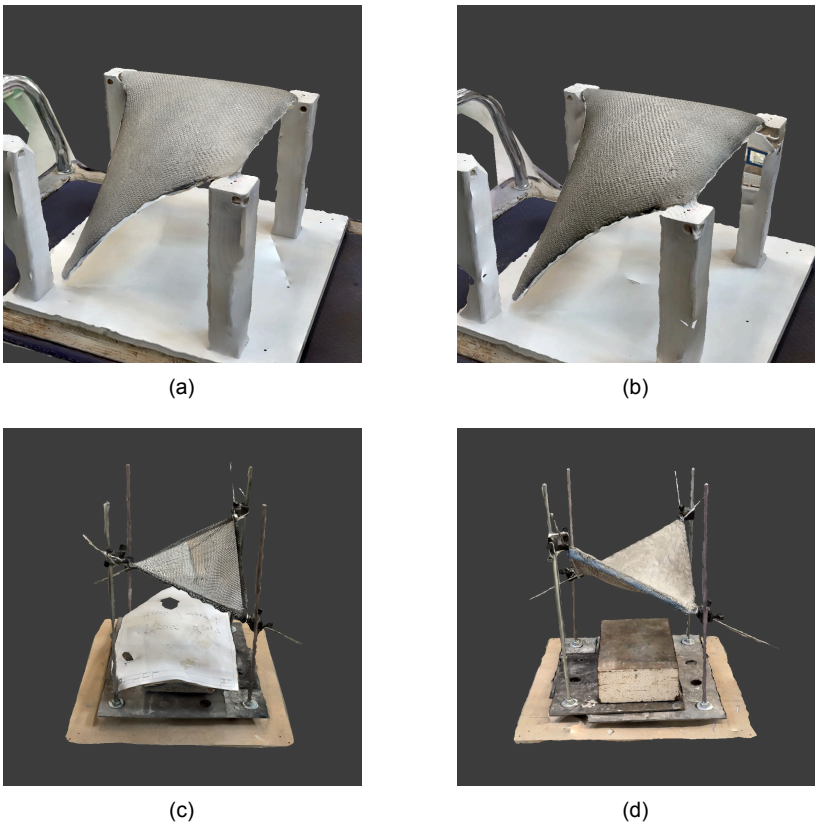

(a) (b)

(c) (d)

Figure 4.16: 3D scans for geometrical analysis: (a) and (b) identical prototypes of Geometry 1, (c) tensioned fabric installed in the supporting frame before casting, (d) fabric including plaster material after casting

Accuracy of repeated geometries

Repeatability of geometries and the required accuracy are important factors for this study. Figure 4.17 illustrates the manufacturing precision of two identical prototypes of *Geometry 1*. The manual method of applying the *SHCC* material onto the tensioned fabric, as discussed in Section 4.1.2, limits the accuracy in achieving an evenly distributed thickness. Due to these manual fabrication inaccuracies, one prototype has a total mass of 1.40 kg (orange) while the other has a total mass of 1.23 kg (green). Figure 4.17 shows the post-processed 3D scans of the prototypes as two overlaid surfaces. It is evident that in the region of the two line supports, the greater weight of the SHCC material of the heavier prototype (orange) resulted in higher vertical deformation of the fabric, while it was lifted upwards in the region of the point support in the upper left corner.

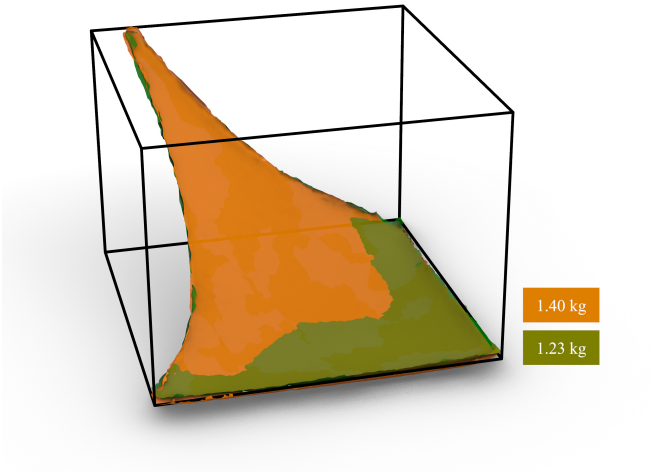

Figure 4.17: Overlay of the 3D scanned surfaces of two identical prototypes of Geometry 1 (green: 1.23kg, orange: 1.40 kg)

The prototypes exhibit an average vertical deviation of 3.27 mm from each other, as shown in Table 4.1. In the context of prefabricated concrete elements, a vertical deviation of 3.27 mm can be considered relatively small. According to current standards and studies on prefabricated concrete components, acceptable dimensional deviations typically fall within a few millimeters [21]. Taking into account the overall dimensions of the prototypes, approximately 30 x 30 x 20 cm, this results in a relative deviation of about 1.10%. Considering the deviation in weight between the elements of about 14%, (1.23 kg vs. 1.40 kg), the relative vertical deviation of only 1.10% indicates a high degree of robustness of the formworking method to inaccuracy in the fabrication process. Given the manual methods employed in the fabrication process, which leave room for improvement, the results of the accuracy analysis are satisfactory.

Overall dimensions	ca. 30 x 30 x 20 cm
Average vertical deviation	3.27 mm
Relative deviation (w.r.t overall dimensions)	ca. 1.10 %

Table 4.1: Vertical deviation between two identical prototypes of Geometry 1, extracted from 3D scans

Contributions of tensioning and loading to fabric deformation

This paragraph presents the results from the investigation into the contributions of tensioning and loading on fabric deformation. As described in Section 3.2.6, the fabric geometries were 3D scanned and evaluated in *Grasshopper* after tensioning in the frame and again after loading by casting the *SHCC* onto it. This analysis determined the changes in surface area and vertical deformation.

Using the total weight of the prototype and its surface area, the approximate uniformly distributed load on the fabric was calculated as follows:

$$\text{Total weight: } G = 1.22\,\text{kg} \tag{4.1}$$

$$\text{Surface area: } A = \text{ca. } 800\,\text{cm}^2 \tag{4.2}$$

$$\text{Uniformly distributed load: } g = 1.22\,\text{kg} \,/\, 800\,\text{cm}^2 \cdot 9.81\,\text{kg} \cdot \text{m/s}^2 = \text{ca. } 0.15\,\text{kN/m}^2 \tag{4.3}$$

Under the load of the *SHCC*, the fabric exhibits a maximum vertical displacement of *39 mm* compared to the tensioned but unloaded fabric. This occurs over a diagonal span of *40 cm*, resulting in a deflection-to-span ratio of approximately *1:10*. These results are shown in Table 4.2. Additionally, the vertical

displacement between the loaded and unloaded fabric is illustrated in Figure 4.18, where the sizes of the dots represent the magnitude of the deformation, and the red dot indicates the point of maximum displacement.

Load	ca. 0.15 kN/m^2
Max. deflection (before/after casting)	39 mm
Diagonal span (edge length 28cm)	40 cm
Deflection-span ratio	1:10

Table 4.2: Geometrical analysis of Geometry 2: Vertical load from self-weight of the plaster material and resulting vertical deflection

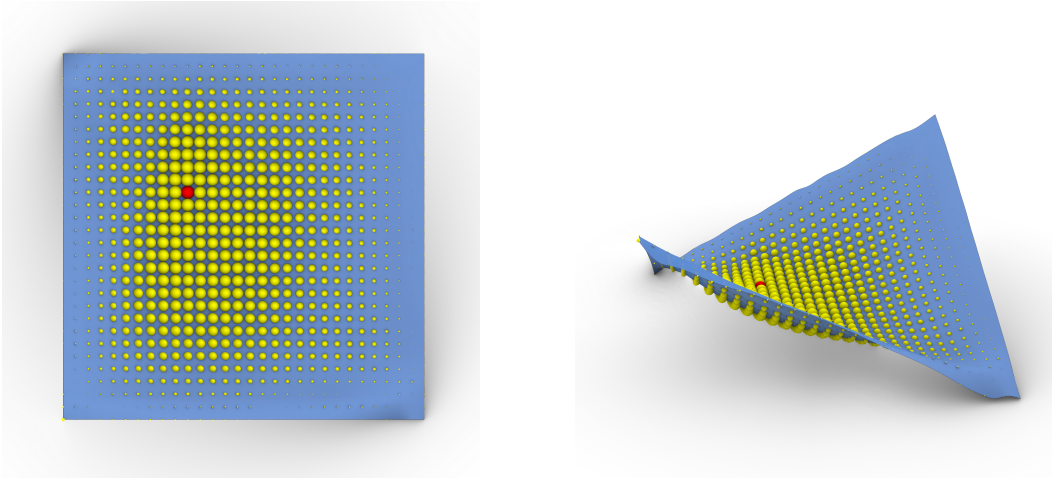

(a) Top view (b) Perspective view

Figure 4.18: Geometrical analysis of Geometry 2: Vertical displacement of fabric between unloaded and loaded state (the sizes of points indicate the magnitude of displacement, maximum in red)

Table 4.3 presents the results of comparing the surface areas under different loading and tensioning conditions. The surface areas of the *tensioned* and *total* states were determined from the 3D scans shown in Figure 4.16 (c) and (d) using *Grasshopper*. The strains of the fabric in both the *tensioned* and *total* states were calculated based on these fabric areas relative to the unstressed area. The strain due solely to the *casting* of the *SHCC* was determined by subtracting the strain from *tensioning* from the *total* strain. Subsequently, the proportional contributions of each state to the total strain were calculated to quantify their respective impacts.

State	Edge length [cm]	Area [cm^2]	Average strain [-]	Contribution [%]
Unstressed	26 x 28	728	-	-
Tensioned	28 x 28	749	0.029	28
Total (tensioned + cast)	28 x 28	804	0.104	100
Cast (total - tensioned)	28 x 28	-	0.075	72

Table 4.3: Geometrical analysis of Geometry 2: Comparison of the surface area of Geometry 2 in different fabrication states

The results presented in Table 4.3 indicate that, in the tested configuration, the contribution of fabric

tensioning to the change in surface area is relatively small at *28%* compared to the *72%* contribution from loading the tensioned fabric with SHCC. This is primarily due to the minimal pretensioning of the fabric in the frame (only *2.9%* strain compared to the flat, untensioned fabric) to match the target edge length of 28 cm, ensuring compatibility with other prototypes of *Geometry 1* fabricated in Section 4.1.2. As shown in the 3D scan of the fabric tensioned in the frame (Figure 4.16 (c)), the fabric exhibits wrinkling in some areas due to the low pretensioning and previous loading during prototype fabrication. Additionally, the inherent asymmetry of the fabric (unstressed dimensions approximately 26 x 28 cm) results in asymmetric pretensioning, leading to asymmetric deformation behavior.

While this is a predictable result, it would be interesting to compare this configuration, where the fabric is minimally pretensioned, with a configuration where the fabric is highly pretensioned before casting. Furthermore, a back-calculation of the Young's moduli from the deformed fabric and a comparison with experimentally determined Young's moduli from ongoing research could yield valuable insights.

The asymmetric behavior is also reflected in the vertical displacement of the fabric under loading. As shown in Figure 4.18, the maximum displacement does not occur at the center of the fabric, as might be intuitively expected, but is shifted to one of the bottom corners. This can be explained by referring to the evaluation of fabric reuse in Section 4.1.2. One relevant factor contributing to the observed asymmetric deformation is the slightly rectangular shape of the unstressed fabric sample. Another factor, as previously mentioned, is the plastic deformation of the fabric due to previous loading and the fabrication of five prior prototypes. The corner that appears strongly stretched outwards in Figure 4.11 (c) in Section 4.1.2 coincides with the corner where the maximum vertical deformation occurs. This suggests that due to preexisting deformation in this area, the fabric was less tensioned, leading to higher deformation.

4.2. Structural analysis of combined shapes

In the following section, the results of the structural analysis of the combined structures are presented. The analysis includes representative examples from various configurations of the elements. Combinations comprising only Geometry 1 elements are evaluated through examples with four elements (Combination 10), three elements (Combinations 8 and 6), and two elements (Combination 5). Additionally, for combinations integrating elements from both Geometry 1 and Geometry 2, Combinations 2.1, 2.2, and 19 are evaluated.

4.2.1. Form-found geometry models

Figure 4.19 shows the form-found geometry models of Geometry 1 and Geometry 2, which are used for the subsequent structural analysis of the combined structures presented in Section 4.1.2 and depicted in Figure 4.14 and Figure 4.15. As described in Section 3.3, the geometry models are form-found using the Grasshopper plug-in *Kangaroo Physics* and are derived from the manually drawn 3D models shown in Figure 3.12. In the form-finding, Geometry 1 is continuously supported at its two straight edges at the bottom and point supported at the upper corner point. Geometry 2 is continuously supported around all of its four edges. The geometries are described by meshes of 2500 faces each. Both geometries are loaded with a downward-facing unary force which is applied at the mesh vertices to represent the self-weight of the mortar on the fabric. It must be noted, that the applied load does not account for the tributary area of the individual mesh vertices, as equal point loads are applied to the mesh vertices.

These 3D models of Geometry 1 and Geometry 2 serve as the building blocks for the digital models of the combined structures, which were physically created by manually combining the prototypes, as described in Section 4.1.2. The digital models of these combined structures are shown in Figure 4.20.

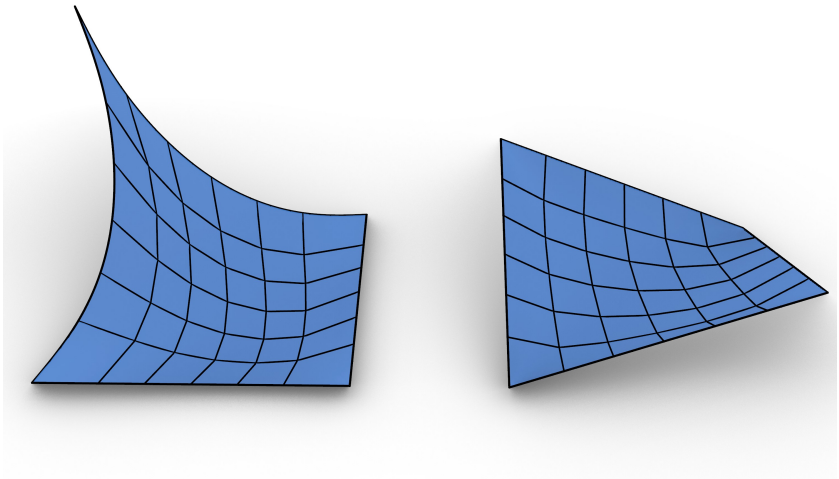

Figure 4.19: Geometry models of Geometry 1 (left) and Geometry 2 (right), form-found using Kangaroo Physics

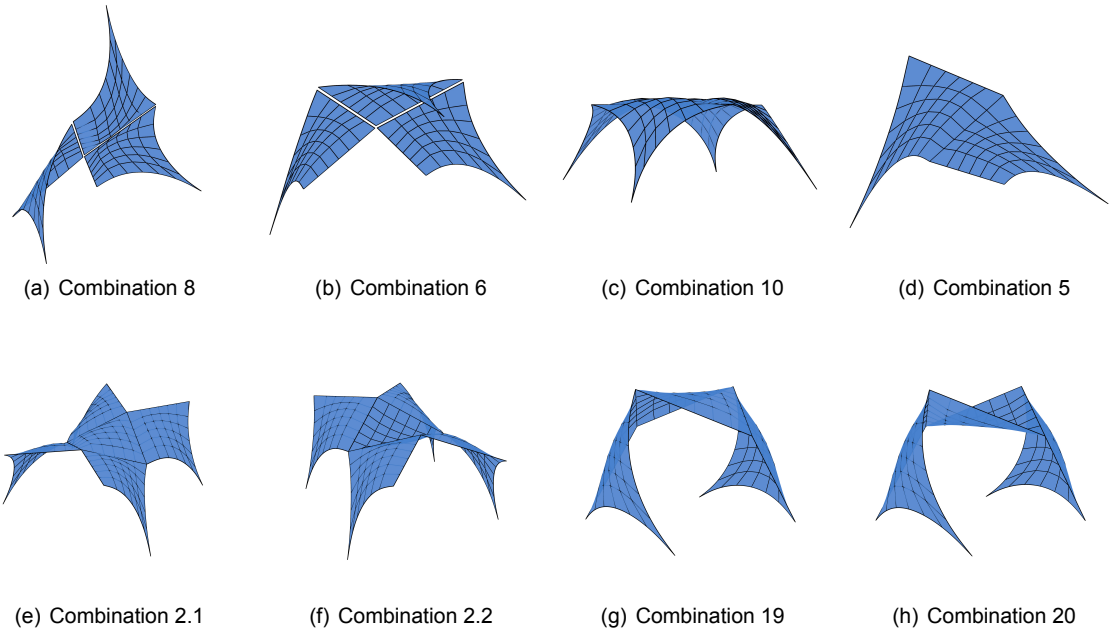

(a) Combination 8 (b) Combination 6 (c) Combination 10 (d) Combination 5

(e) Combination 2.1 (f) Combination 2.2 (g) Combination 19 (h) Combination 20

Figure 4.20: Geometry models of combinations of Geometry 1 and 2

4.2.2. Mesh analysis convergence

The results of the mesh analysis convergence are presented below. The mesh analysis convergence has been conducted on Combination 8, with the connection between the three elements modeled as rigid links, representing the connectors in the as-built physical prototype.

Figure 4.21 (a) shows the progression of the total strain energy in the system as the number of mesh faces in the model increases. The plot indicates that beyond approximately 30,000 mesh faces, the strain energy in the model stabilizes and converges to a value of around 0.35 kNm. For the subsequent analyses, a mesh with 38,400 faces is selected as it offers a compromise between model precision and computational efficiency. This corresponds to a UV count of 80 (with subsequent triangulation) for each of the three elements. The resulting mesh density of the structure is visualized in Figure 4.21 (b).

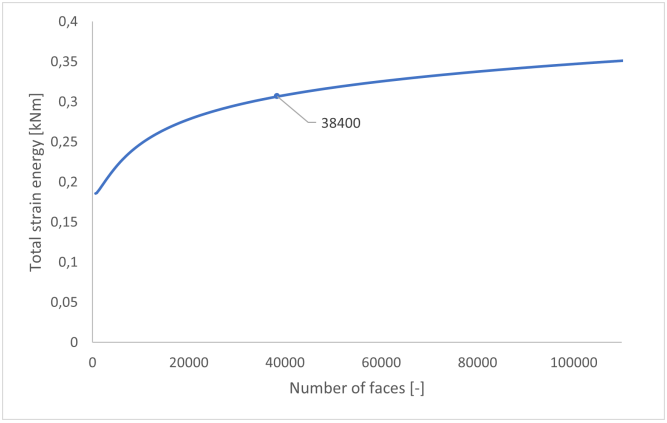

(a)

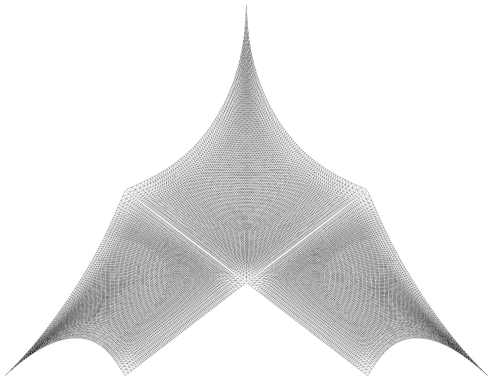

(b)

Figure 4.21: Mesh analysis convergence: (a) Plot of the total strain energy over the number of faces, (b) chosen mesh density (38,400 faces)

Although not significant, a remaining upward trend is observable in the plot, indicating that the model's precision still improves with an increasing number of mesh faces. This can be explained by the method of meshing the surfaces. The surfaces are meshed using a UV-mesh, created from curves that lie in two different directions (U and V), intersecting to form a closed mesh. In regions of higher curvature, the UV-mesh density increases to accurately describe the surface geometry, while in areas of lower curvature, the mesh density decreases. Therefore, increasing the UV-count primarily increases the mesh density in areas of greater curvature, with less impact on areas of smaller curvature.

In the investigated model, this results in a denser mesh in the more strongly curved center of the elements, and a less dense mesh in the less curved corner points. However, due to the modeling of the connection of the elements as rigid links at these corner points, the stress variations in the system are highest in these regions and lower in the center of the elements. Thus, further increasing the UV-count, and thereby the mesh density, still improves the precision of the model as the stress distribution in the corner points is described more accurately. The described phenomenon is illustrated in Figure 4.22, which shows the mesh faces with their corresponding first principal stress vectors (in the middle layer). The size of the vector arrows corresponds to the magnitude of the stress. The figure clearly indicates a lower mesh density in the corner regions, where large stress variations occur, and a higher mesh density towards the center of the elements, where only low stress variations occur.

As a result, the total strain energy does not fully converge, since the mesh density increases primarily in the center of the elements, where it has less influence, and less in the corner points, where the increased density significantly affects the calculation results.

This issue could have been addressed by applying mesh refinement techniques or more targeted mesh-

ing of the surfaces. However, for the purposes of the analyses, led in the following sections, the chosen mesh density can be considered sufficient.

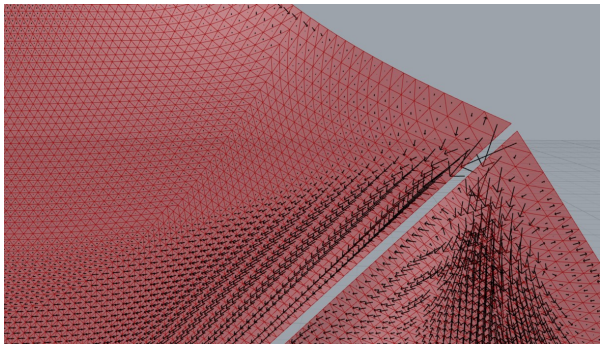

Figure 4.22: First principal stress vectors and corresponding mesh density in the corner regions of the surfaces

4.2.3. Connection modeling

For the structural analysis of the combined structures, the FEA software package *RFEM6* by *Dlubal*, as well as the FEA tool *Karamba3D* [32] are used.

The combined structures are loaded by their self-weight. Each structure is supported by pinned point supports that restrict translational degrees of freedom in the x-, y-, and z-directions while allowing free rotation around these axes. The combined structures are modeled at an approximate scale of 15:1 compared to the physically built prototypes to simulate the behavior and forces acting on a full-sized structure. Consequently, the individual elements have dimensions of approximately 4 x 4 meters with a thickness of 5 centimeters.

The FE calculations are conducted geometrically linear.

As described in Section 3.3, various connection types between the individual elements are investigated. In addition to rigid and hinged continuous line-joint connections, linked connections will be tested to simulate the edge connectors used in the physical prototypes presented in Section 4.1.2. To simulate the behavior of the connectors as hinged local connections, they are modeled as seven ”rigid-hinge” couplings, each 5 cm in length, distributed over a total length of 15 cm at each connection point. A 5 cm gap between the elements prevents their structural interaction. The described modeling concept of the linked connection is shown in Figure 4.23.

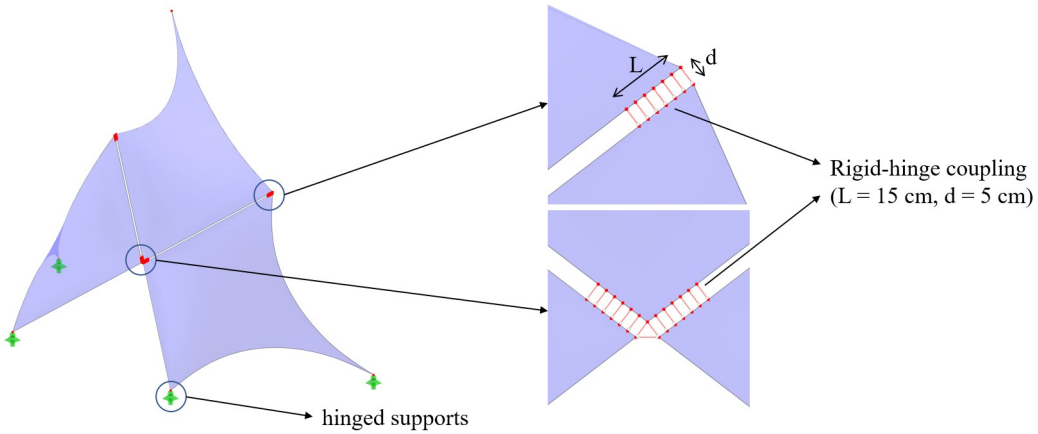

Figure 4.23: Modeling concept of supports and the linked connection variant

4.2.4. Combined structures

In the following section, the results of the structural analysis of the combined structures are presented. The analyses cover strain energy, stress, and deformation. For Combination 8, the results are discussed in detail, including the values and subdivision of the strain energy analysis based on model parametrization and different connection variants. Both the relative values of the axial strain energy ratio and the absolute values of the total strain energy are provided, along with the respective contributions of axial and bending strain energy. Detailed deformation and stress analysis results for the hinged connection variant are presented for three relevant element configurations.

The remaining combinations are analyzed using the same methodology, with only the key findings highlighted. Detailed results for the remaining combinations are compiled in Appendix A and a detailed analysis is provided in Appendix B.

Combination 8

In the following paragraphs the results of the structural analysis of Combination 8 are presented.

Parametrization Due to the configuration of the three elements, Combination 8 allows for parametrization by varying the angle between the elements. As illustrated in Figure 4.24, the elements are rotated around the axis of their connected edges (shown in red). While different rotation angles for the two axes are possible, equal angles are chosen to achieve a symmetric structure. Adjusting these angles results in either the ”opening” or ”closing” of the panels. When the panels open, the front supporting points move away from each other while when they close, the front supporting corner points move towards each other. In the ”planar” configuration, a rotation angle of 0° indicates that all corner points connected to the elements’ straight edges are in one plane. A negative rotation angle indicates an ”opening” of the structure, while a positive rotation angle indicates a ”closing” of the structure.

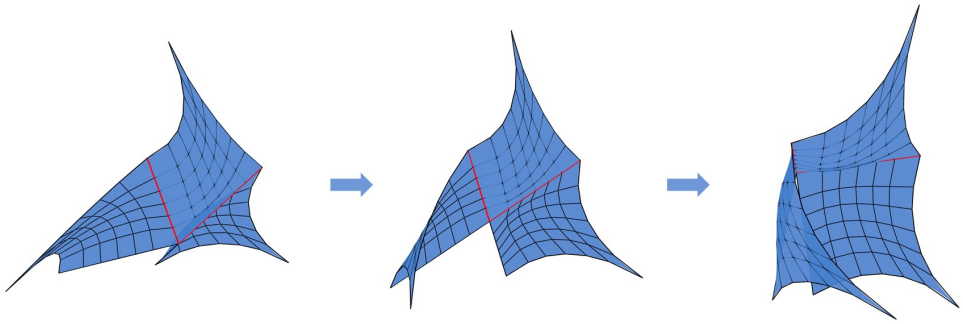

Figure 4.24: Combination 8: Parametrization of the element configurations from ”open” (left) to ”closed” (right) and rotation axes in red

Strain energy analysis and optimization The results of the strain energy analysis are shown in Figure 4.25 and Figure 4.26 for the three connection types. Three distinctive rotation angle configurations of the structure are discussed and analyzed more in detail.

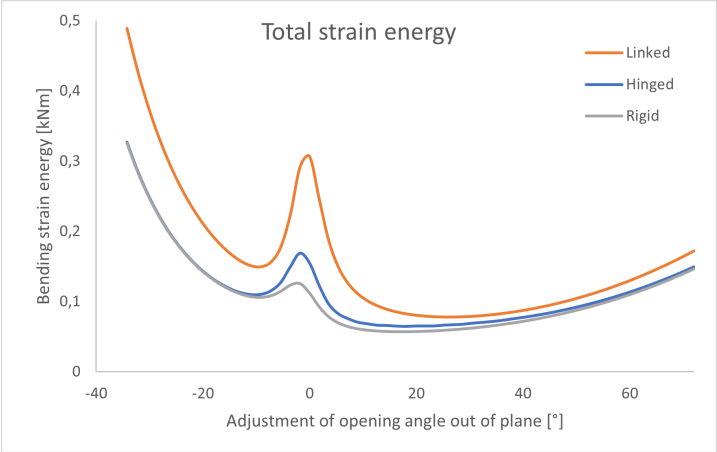

(a) Total strain energy (total = axial + bending)

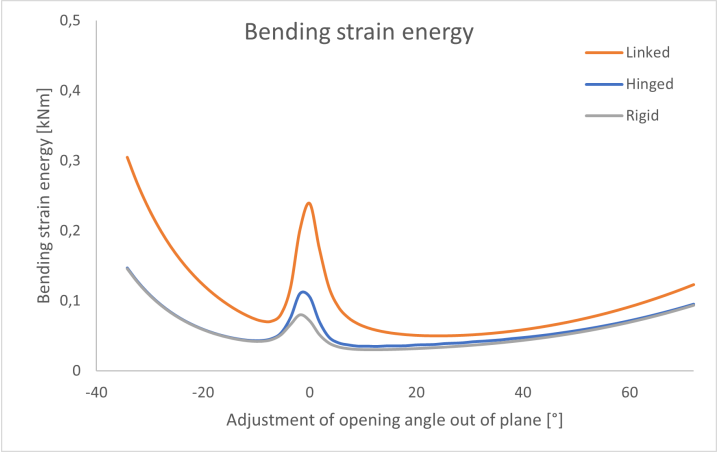

(b) Bending strain energy (bending)

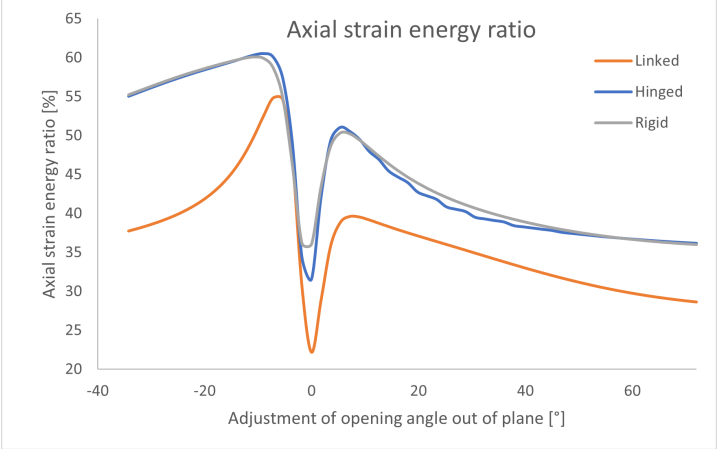

(c) Axial strain energy ratio (ratio = axial / total)

Figure 4.25: Combination 8: (a) Total strain energy, (b) bending strain energy, and (c) axial strain energy ratio depending on angle variation and for different connection types

The plots in Figure 4.25 show that regarding the minimum total strain energy and minimum bending strain energy, as well as regarding the maximum axial strain energy ratio, the linked connection variant performs worst, while the hinged and rigid connection variants perform similar, with the rigid connection variant performing slightly better. Furthermore, the plots reveal a similar behaviour of the total strain

energy and the bending strain energy, both exhibiting a peak at a rotation angle of 0° and local minima at small negative and positive rotation angles.

In the plots of the axial strain energy ratio, distinct peaks are observed at negative rotation angles (-7.2° for the linked connection, -9.0° for the hinged and rigid connection). At these angles, the membrane behavior of the structures is maximized, resulting in the highest proportion of forces being transferred through axial forces, with a maximum axial strain energy ratio of 55% for the linked connection and even higher values of 60% and 61% for the hinged and rigid connections respectively. Although the most membrane-like behavior is achieved at these rotation angles, they do not correspond to the minimum total strain energy.

The minimum bending strain energy for all three connection types occurs in a more ”closed” configuration at a rotation angle of 23.4° for the linked connection and 12.6° for the hinged and rigid connections. This deviation from the angles of maximum axial strain energy ratio can be explained by the different contributions of bending and axial strain energy to the total strain energy in the system in different configurations. The contributions of bending and axial strain energy to the total strain energy are shown in Figure 4.26. Particularly in the hinged and rigid connection variant, the plots show, that at negative rotation angles, the axial strain energy has a larger contribution to the total strain energy than the bending strain energy, while at positive rotation angles, the bending strain energy dominates. This results in the axial strain energy ratio and therefore the membrane behaviour being higher at negative rotation angles. In contrast, the plots show, that the bending strain energy in the system is generally lower at positive rotation angles. This circumstance leads to the difference in ”optimal” configurations regarding the maximum axial strain energy ratio and the minimum bending strain energy.

In the ”planar” setting with a rotation angle of 0°, where the straight edges are aligned in one plane, the axial strain energy ratios show significant dips in all connection types, while the bending strain energy spikes. In these configurations, the structures exhibit their lowest axial strain energy ratios of 22% (linked), 32% (hinged), and 36% (rigid), indicating that bending stresses dominate. This is confirmed by the peaks in the bending strain energy plots for these configurations.

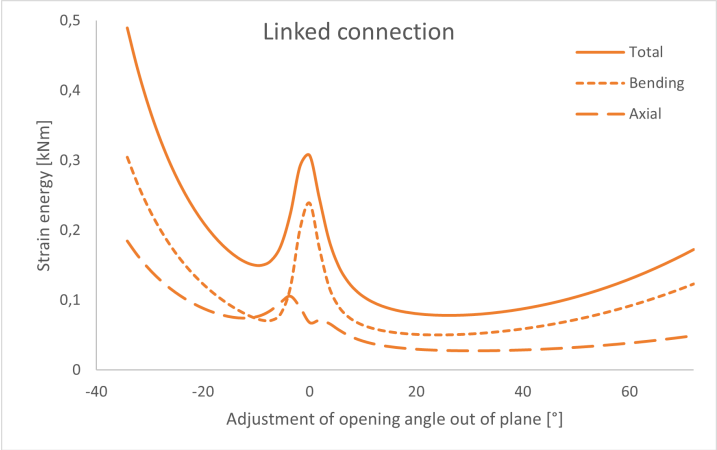

(a) Total strain energy contributions - linked connection

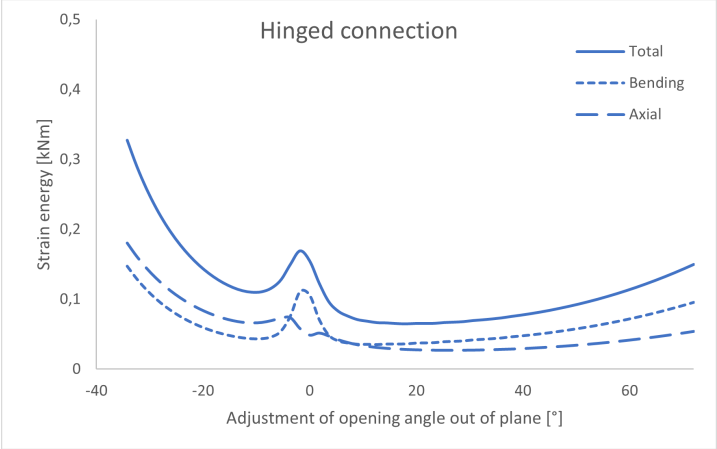

(b) Total strain energy contributions - hinged connection

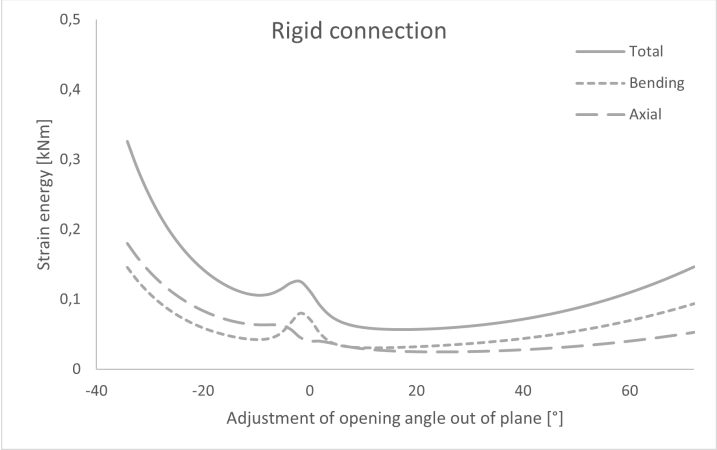

(c) Total strain energy contributions - rigid connection

Figure 4.26: Combination 8: Contributions to the total strain energy for (a) linked connection, (b) hinged connection and (c) rigid connection depending on opening angle

The spiking behavior of the total and bending strain energy plots shown in Figure 4.25 (a) and (b) and Figure 4.26 indicate the occurrence of a mechanism-like effect in the ”planar” configuration at a rotation angle of 0°. In this configuration, the joints between the individual elements lay in the same plane as the regions of the surfaces, that exhibit predominantly single curvature. These regions have

low stiffness around the axes on which the surface has no or very low curvature, which consequently act as additional hinges. Are those additional hinges aligned in one plane with the planar joints between the elements, a mechanism-like effect occurs.

In terms of the overall magnitudes of bending strain energy and axial strain energy ratios for the different connection types, the plots indicate that the rigid connection type performs best, exhibiting the lowest bending strain energy. This is followed by the hinged connection type, and lastly, the linked connection type. Given the increased complexity of realizing a rigid moment-resisting connection between the elements in practice, the hinged connection type appears to be the most promising for Combination 8. Its performance in terms of total and bending strain energy as well as axial strain energy ratio is intermediate, between the rigid and linked connection types. Therefore, the hinged connection type will be evaluated in the following detailed FE-analysis of the structure, although in practice the connection (such as a grouted connection) will likely perform in between a rigid and hinged connection. For a better understanding of the analyzed configurations, they are visualized in Figure 4.27.

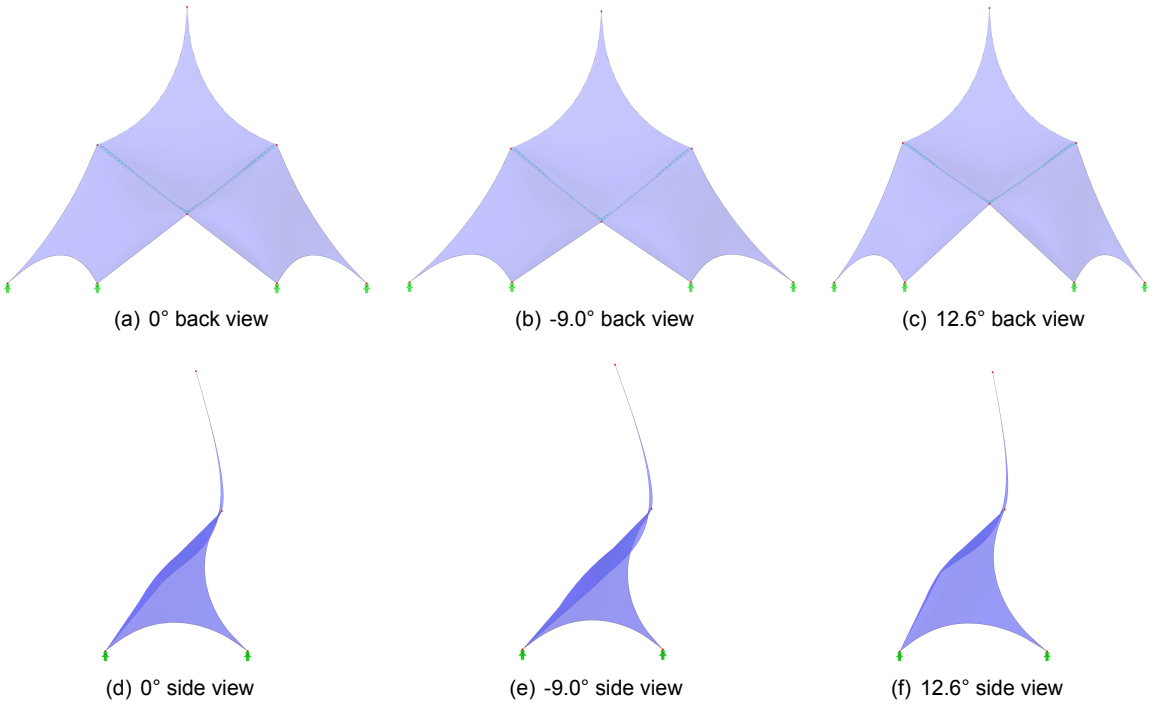

Figure 4.27: Combination 8: Configurations of the hinged connection variant that are evaluated in detail

Deformation analysis of the hinged connection variant The observations regarding the structure's behavior under different rotation angle configurations are supported by the deformation analysis results. The deformations for the three configurations at 0°, -9.0°, and 12.6° are shown in Figure 4.28. The planar configuration at 0° (a) exhibits very large deformations, measuring 119 mm at the top and 106 mm in the center of the structure. Given the overall width of the structure, approximately 12 meters, these deformations are to be considered large, resulting in a span-deformation-ratio of about $L/100$. This observation confirms the occurrence of a mechanism-like effect in the structure in a planar configuration, and suggests, that the assumption of small deformations for the geometrically linear FE-calculation is not valid, and non-linear calculations would be necessary to accurately describe the structure's behaviour.

In contrast, the maximum deformations are significantly smaller in the -9.0° (b) and 12.6° (c) configurations, measuring 30 mm and 23 mm respectively. This indicates that the planar configuration exhibits deformations that are four to five times larger than those in the out-of-plane configurations. These observations confirm the stiffening effect of the configurations under both positive and negative rotation angles.

The deformation plots for the configurations at -9.0° (b) and 12.6° (c) illustrate the different behavior between the more ”open” and more ”closed” configurations. In the -9.0° configuration, the tip of the top element deforms upwards, whereas in the 12.6° configuration, it deforms downwards. Both configurations show large outwards-pointing deformations at the slender parts of the supporting elements, which in the case of the 12.6° configuration is the location of the maximum deformation. Generally, the 12.6° configuration exhibits larger deformations in the center of the structure and smaller deformations at the tip. In contrast, the -9.0° configuration shows smaller deformations in the center and larger deformations at the tip of the top element.

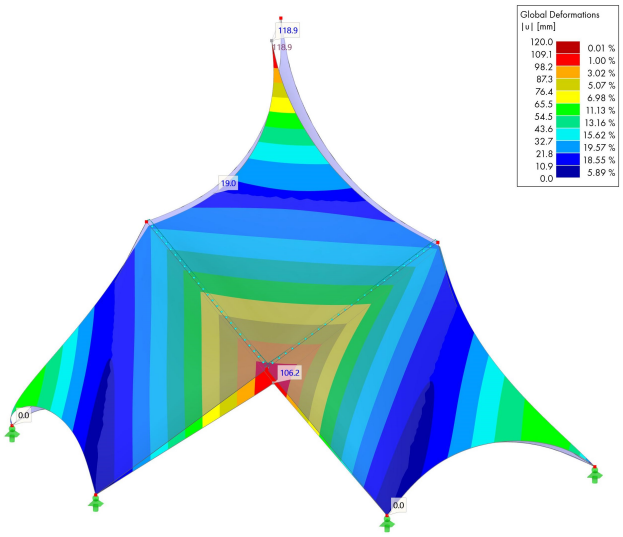

(a) 0°

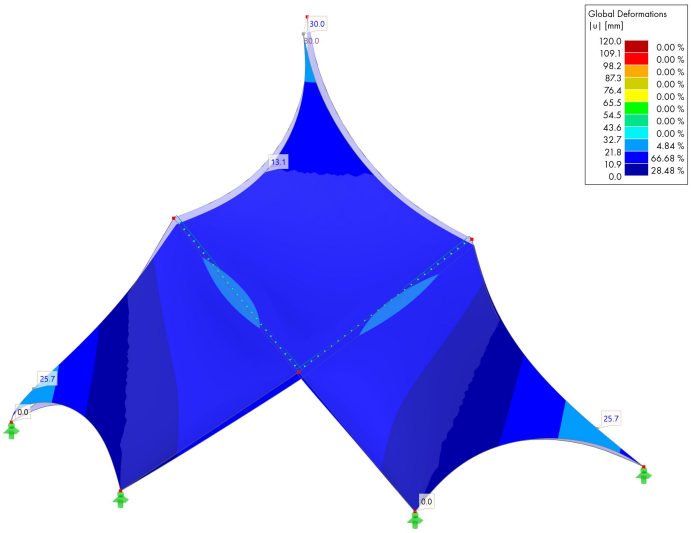

(b) -9.0°

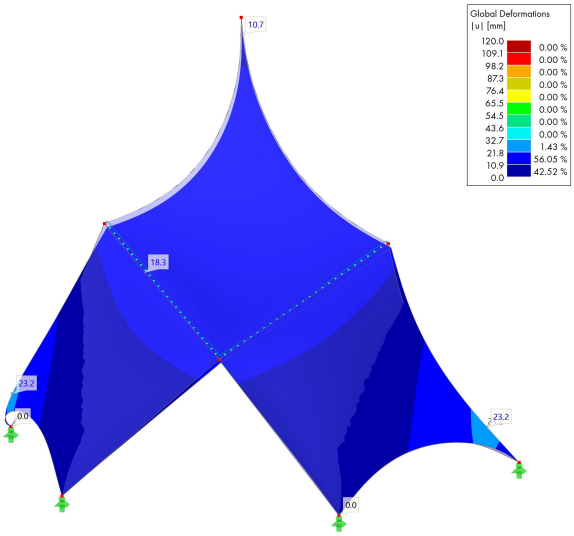

(c) 12.6°

Figure 4.28: Combination 8: Deformation under self-weight for rotation angles (a) 0°, (b) -9.0°, and (c) 12.6°

Tensile stress analysis of the hinged connection variant The results of the tensile stress analysis of the hinged connection variant of Combination 8 are presented in Figure 4.29. The plots show the first principal stresses in the structure in either the top or bottom layer of the surfaces, that result in the governing tensile stresses. To provide insightful and comparable visualizations, the plots show tensile stresses on a color scale from blue (lowest) to dark red (highest), while compressive stresses in the structure are not shown and appear as white areas in the plots. The scale ranges from 0 N/mm^2 to 3.5 N/mm^2, with values above 3.5 N/mm^2 collectively appearing in dark red. Additionally, the plots show the percentages of surface area that lay within the different ranges of stresses. The plots thereby provide more exact insight into how much of the surface is in compression, how the tensile stresses are distributed over the structure and what parts of the structure exceed the value of 3.5 N/mm^2. The value of 3.5 N/mm^2 has been chosen as a reference value, as this denotes the maximum tensile strength of the used SCHH material, as presented in Table 3.2.

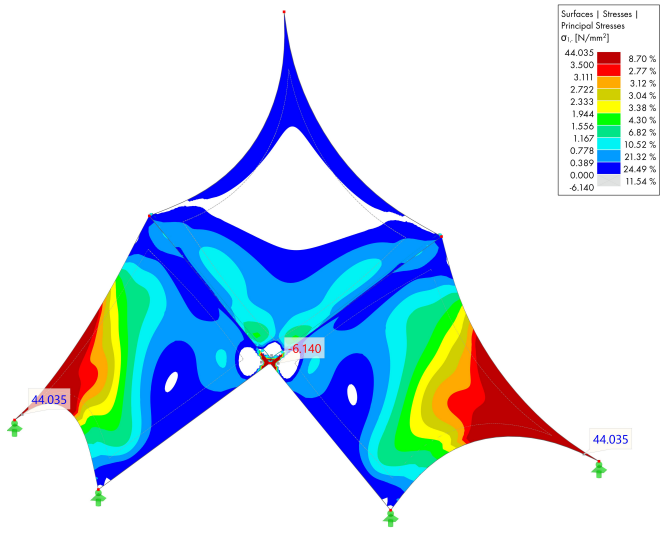

(a) 0°

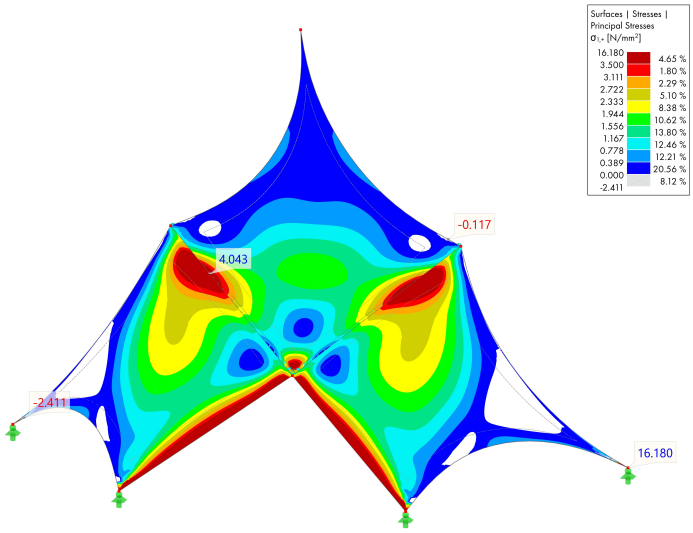

(b) -9.0°

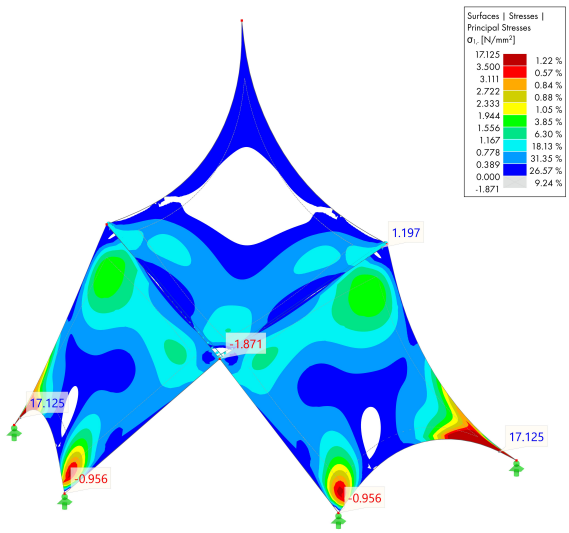

(c) 12.6°

Figure 4.29: Combination 8: Tensile stresses under self-weight for rotation angles (a) 0°, (b) -9.0°, and (c) 12.6°

The plot of tensile stresses in the 0° configuration, shown in Figure 4.29 (a), shows significant tensile stresses within the structure. The highest tensile stresses occur in the top layer of the surfaces, particularly in the two bottom elements in the regions of the lateral supports. According to the color scale, 8.7% of the surface area exceeds the tensile limit of 3.5 N/mm^2, reaching up to 44.0 N/mm^2. In contrast, the -9.0° configuration (b) exhibits much lower tensile stresses throughout the structure. The maximum tensile stresses in this configuration are found in the bottom layer of the surfaces, mainly along the free straight edges of the bottom surfaces. This region coincides with the center of the structure, which also shows significant deformations as discussed in the previous section. Overall, only 4.7% of the surface area exceeds the tensile limit of 3.5 N/mm^2, with a maximum stress of 16.2 N/mm^2. The 12.6° configuration (c) shows the lowest tensile stresses, with high tensile stresses in the top layer occurring very locally at the four point supports. Only 1.2% of the total surface area exceeds the tensile limit of 3.5 N/mm^2, with a maximum stress of 17.1 N/mm^2.

It can be concluded that the observed stresses in the different configurations are consistent with the results from the strain energy analysis. While the 0° configuration exhibits significant tensile stresses, the -9.0° and 12.6° configurations show relatively low tensile stresses. This observation aligns with the low bending strain energy observed in the latter configurations.

Key findings of remaining combinations

In the following paragraphs, the key findings of structural analysis of the remaining Combinations 6, 10, 5, 2.1, 2.2, 19 and 20 are presented.

Combination 6 Combination 6 follows the same parametrization concept as Combination 8. As described in Section 4.1.2, Combination 6 is essentially the same as Combination 8, with the exception that the top element is flipped, resulting in a larger cantilever. This structure allows for the same rotational adjustment of the elements around the axes of the connected edges between the bottom elements and the top element, as described for Combination 8. This rotation results in an ”open” form for negative rotation angles and a ”closed” form for positive rotation angles. The geometry and the axes, around which the elements are rotated are shown in Figure 4.30.

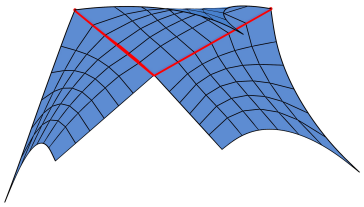

Figure 4.30: Combination 6: Geometry and axes around which the elements are rotated

As illustrated in the plot of the total strain energy in Figure 4.31, Combination 6 exhibits behavior similar to Combination 8, with a peak at a rotation angle of 0°, indicating the occurrence of a similar mechanism-like effect. However, in Combination 6, this effect is notably less pronounced, being only slightly present in the hinged connection variant and almost negligible in the rigid connection variant. Additionally, it is important to note that the overall magnitude of the total strain energy in this system is higher than in Combination 8. This increase can be attributed to the large cantilever resulting from the orientation of the top element.

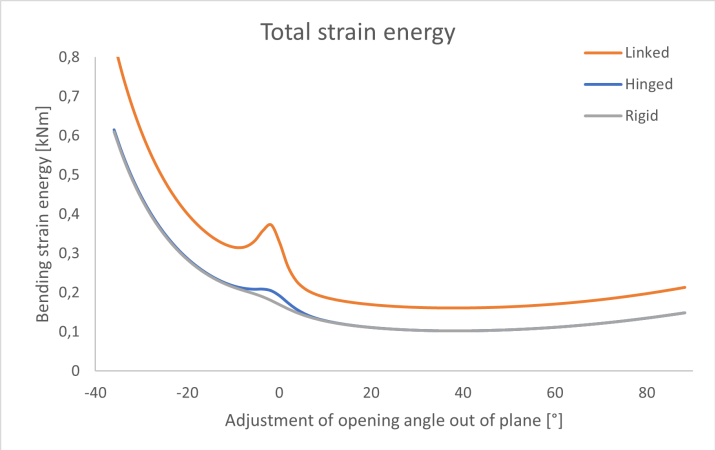

Figure 4.31: Combination 6: Total strain energy (total = axial + bending) in the system depending on the rotation angle and connection type

Combination 10 Combination 10 consists of four elements from Geometry 1, configured to form a system that is double-axisymmetric. Since this is the only system with double-axisymmetry amongst the presented combinations, parametrizing the rotation of angles between individual elements is not considered, as it would compromise this symmetry. Instead, the different connection types (linked, hinged, and rigid) are evaluated in detail and compared to one another.

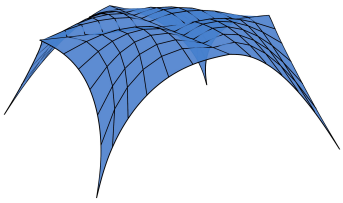

Figure 4.32: Combination 10: Geometry model used for the FE-analyses

The results of the strain energy analysis for Combination 10 are presented in Table 4.4. In previous analyses of Combinations 8 and 6, the most significant differences in strain energy between various connection variants were observed at a rotation angle of 0°, where mechanism-like effects occurred. In Combination 10, the joints between elements lie in one plane with the single-curvature regions of the surfaces, which exhibit low stiffness. When these joints are connected non-rigidly, the hinges align with the low-stiffness regions, creating a mechanism-like effect similar to those observed in Combinations 8 and 6. This effect is confirmed by the strain energy values, with significantly higher total strain energy for the linked (0.82 kNm) and hinged (0.63 kNm) connection variants compared to the rigidly connected variant (0.10 kNm). This pattern is also reflected in the remaining strain energy values and the axial strain energy ratio. These findings indicate that, for configurations like Combination 10, where joints between elements are in the same plane as regions of single curvature and low surface stiffness, a rigid connection is necessary for achieving sufficient structural performance.

Connection	Total SE [kNm]	Bending SE [kNm]	Axial SE [kNm]	Axial SE ratio [%]
linked	0.82	0.68	0.14	17
hinged	0.63	0.52	0.11	17
rigid	0.10	0.06	0.04	41

Table 4.4: Combination 10: Results of the strain energy (SE) analysis for the linked, hinged and rigid connection variant

Combination 5 Combination 5 consists of two elements of Geometry 1 and allows for parametrization by rotating the two elements relative to each other at their connected interface edge, shown in red in Figure 4.33. The first element, supported at two points, rotates around the axis between these support points, while the second element rotates around the axis of the interface edge accordingly. A rotation angle of 0° represents the lowest configuration, in which the free, straight edge of the first element (supported on two points) lies in the same plane as the support points.

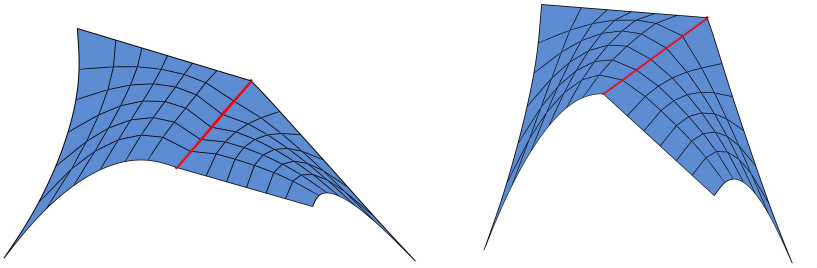

(a) ”Flat” configuration (37.8°) (b) ”Optimized” configuration (84.6°)

Figure 4.33: Combination 5: (a) ”Flat” and (b) ”optimized” geometries and axes around which the elements are rotated

The plot of the total strain energy for the three connection variants as a function of the rotation angle between the two elements is shown in Figure 4.34. All connection variants exhibit a minimum strain energy at a rotation angle of 84.6°. The as-built ”flat” configuration, corresponding to a rotation angle of 37.8°, and the ”optimized” configuration with minimum total strain energy are visualized in Figure 4.33. It is evident that the ”optimized” configuration is much steeper and covers a smaller area compared to the ”flat” configuration. This suggests that the lower strain energy in the ”optimized” configuration results from the reduced span of the structure. Additionally, for ”flatter” configurations, the linked connection variant exhibits significantly higher strain energy than the rigid and hinged connection variants. However, for steeper configurations beyond the ”optimized” configuration, both the hinged and linked connection variants show higher strain energy compared to the rigid connection variant. At the ”optimized” configuration, all three connection variants perform similarly.

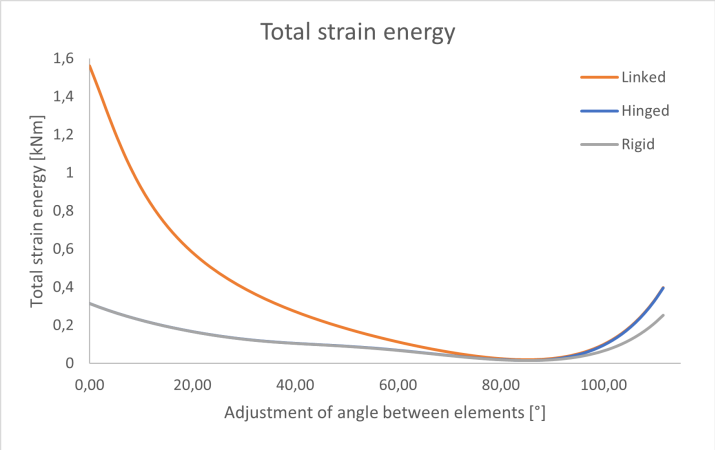

Figure 4.34: Combination 5: Total strain energy (total = axial + bending) in the system depending on the rotation angle and connection type

Combinations 2.1 and 2.2 Combinations 2.1 and 2.2 are analyzed together, and the results are presented in the following paragraphs. In both combinations, the element of Geometry 2 is located at the center of the structure and supported by four elements of Geometry 1. In Combination 2.1, the Geometry 2 element is flipped upside down compared to its fabrication setup, resulting in an upward curvature. In Combination 2.2, the central Geometry 2 element remains in its original orientation, resulting in a

downward curvature. By combining five elements to one structure, Combinations 2.1 and 2.2 are the largest combinations tested in this study. Again, the structures are parametrized with regards to the rotation of the elements against each another around the connected edge between them, while keeping the symmetry of the structure.

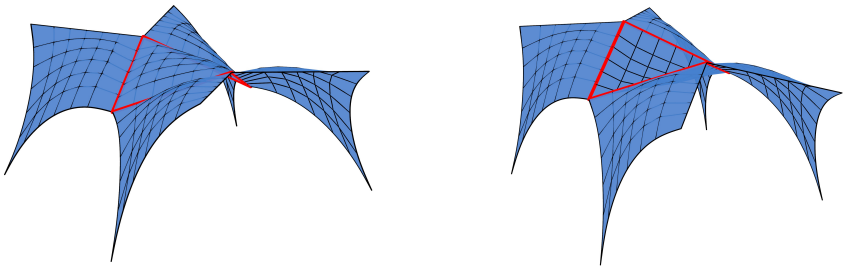

(a) Combination 2.1 (b) Combination 2.2

Figure 4.35: Combination 2.1 & 2.2: Geometries in their configurations of minimum strain energy and axes around which the elements are rotated

The plots of the strain energy analysis in Figure 4.36 illustrate the distinct behavior of the two combinations. Combination 2.1 exhibits the lowest total strain energy at wider spanning configurations, with positive rotation angles of 27.0°, 18.9°, and 21.6° for the linked, hinged and rigid connection variants respectively. In contrast, Combination 2.2 shows better performance in total strain energy at narrower configurations, with negative rotation angles of -9.9°, -0.9° and -9.0°, for the linked, hinged and rigid connection variants respectively. Furthermore, the analysis indicates that Combination 2.2 performs generally better than Combination 2.1, showing lower minimum values of the total strain energy for each of the three connection variants.

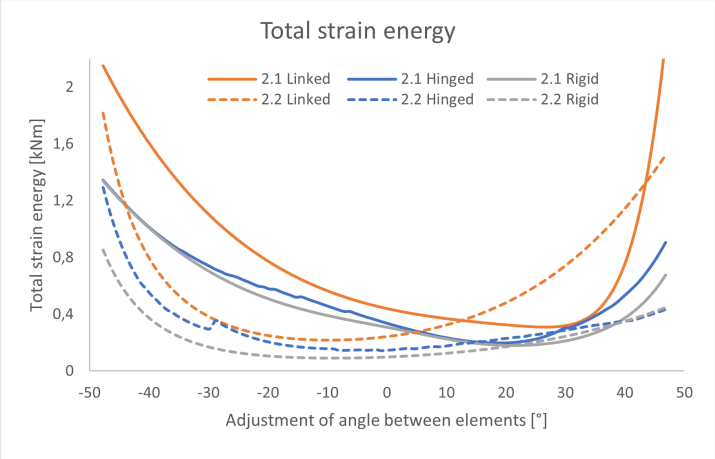

Figure 4.36: Combination 2.1 & 2.2: Total strain energy (total = axial + bending) in the system depending on the rotation angle and connection type for

Combinations 19 and 20 In this section, the analysis results of the Combinations 19 and 20 are presented. Combination 19 consists of two supporting elements of Geometry 1 and one element of Geometry 2, which spans between them and which is inverted compared to its fabrication configuration. Combination 20 is similar, except the central Geometry 2 element is not inverted. Due to the requirement of symmetry and having all four support points in one plane, these configurations do not allow for parametrization in the analyzed configurations. Therefore, the combinations are presented together, and their performance is compared.

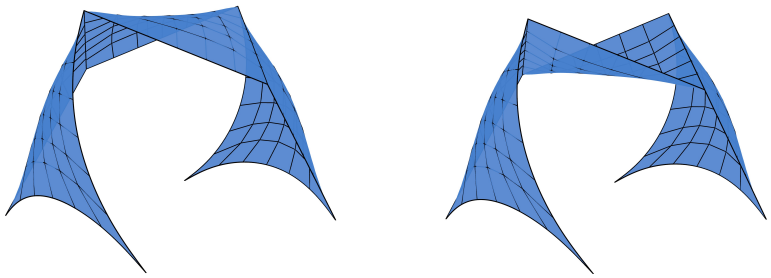

(a) Combination 19 (b) Combination 20

Figure 4.37: Combination 19 & 20: Geometry models used for the FE-analyses

The results of the strain energy analysis of Combinations 19 and 20 are shown in Table 4.5. In both combinations, the axial strain energy ratio does not differ drastically between the different connection types. The axial strain energy ratios of Combination 19 are 47.9%, 49.7%, and 49.5% for linked, hinged, and rigid connections, respectively. Combination 20 performs slightly better with axial strain energy ratios of 54.0%, 54.7%, and 55.2% for linked, hinged, and rigid connections. In contrast, the total strain energy stored in the systems differs significantly, especially between the linked and hinged/rigid connection variants. In Combination 19, the linked connection variant, with a total strain energy of $1.79 * 10^{-2}$ kNm, is almost twice as high as the hinged and rigid connection variants, which have $9.94 * 10^{-3}$ kNm and $9.84 * 10^{-3}$ kNm, respectively. Combination 20 shows a similar pattern with $2.02 * 10^{-2}$ kNm for the linked, $1.26 * 10^{-2}$ kNm for the hinged, and $1.18 * 10^{-2}$ kNm for the rigid connection variant. This can be interpreted as resulting from different bending behaviors between the connection variants. In the hinged and rigid variants, the central element is supported along the length of the two opposing edges, leading to predominantly uniaxial bending in the central element. In contrast, in the linked connection variant, the central element is supported only at its four corner points, resulting in biaxial bending. Furthermore, the linear connections in the hinged and rigid variants allow for a more distributed load transfer through the two supporting elements, while in the linked variant, stress concentrations occur at the four connecting points.

No.	Connection	Total SE [kNm]	Bending SE [kNm]	Axial SE [kNm]	Axial SE ratio [%]
19	linked	$1.79 * 10^-2$	$9.32 * 10^-3$	$8.57 * 10^-3$	47.9
	hinged	$9.94 * 10^-3$	$5.00 * 10^-3$	$4.94 * 10^-3$	49.7
	rigid	$9.84 * 10^-3$	$4.97 * 10^-3$	$4.87 * 10^-3$	49.5
20	linked	$2.02 * 10^-2$	$9.27 * 10^-3$	$1.09 * 10^-2$	54.0
	hinged	$1.26 * 10^-2$	$5.69 * 10^-3$	$6.87 * 10^-3$	54.7
	rigid	$1.18 * 10^-2$	$5.28 * 10^-3$	$6.51 * 10^-3$	55.2

Table 4.5: Combination 19 & 20: Results of the strain energy (SE) analysis for the linked, hinged and rigid connection variants

5 Discussion

The results of the research presented in Section 4 of this thesis provide valuable insight into the possibilities and the limitations regarding the design space provided by the presented formworking technology. Moreover, they give information on the reuse potential for the creation of different geometries and modular combinations of these. The structural analyses provide an understanding of the mechanical behaviour of combined structures and give insight into how it can inform their design. The implications of these results are further discussed in the following sections.

5.1. Physical prototyping

The first set of prototypes created during the physical prototyping phase showcased the extensive design spectrum of shapes achievable using various support and pre-stressing strategies. They demonstrated that the integration of articulated features into the final structure can be controlled by adjusting the level and direction of pre-stressing, implementing specific features in the fabric, and configuring the textile supports.

The successful fabrication of prototypes using cables, bent rods, intermediate point supports, weights, and various support configurations only provides a glimpse into the possibilities. It not only showcases the versatility of these methods but also inspires further exploration into what can be done with additional tensioning techniques and the combination of even more boundary configurations, such as those explored in the second set of geometries.

While integrating features into the fabric allows for the incorporation of tensioning elements such as cables and rods, it also restricts the fabric's flexibility for configurations where these elements are not used. When implemented intentionally and strategically, integrated textile features like different patterns and channels can serve as valuable design parameters. However, a balance between customization and flexibility must be considered. Features such as channels impact the geometry of the resulting element due to their differing stiffness, as demonstrated in the prototypes. Additionally, the implementation of channels affects the overall dimensions of the fabric as different patterns result in different dimensions. Here, the warp/weft direction of the fabric needs to be considered, as the relative dimensions in these directions vary from pattern to pattern. These considerations regarding the influence of patterns and their combinations are subject to ongoing research and addressed in [11].

The updated frame design, utilizing steel and aluminum, demonstrated the value of an adaptable support system to utilize the fabric's ability to adapt to various shapes. The investigations into possible boundary variations, achieved with the designed frame system and built prototypes, showcased the additional design space that emerges from out-of-plane configurations of the fabric boundaries. Future research can potentially combine the spatial variation of boundary configurations with further tensioning provisions, such as those previously mentioned, to expand the range of achievable geometries.

The concept of the spatially adaptable frame has the potential for integration into a more automated workflow for adjusting the positioning of support rods or points. Inspired by the operation of common 3D

printers, the horizontal positioning of the frame columns and the vertical adjustment of the support points on the columns could be motorized and controlled according to a predefined configuration. Automating this process would not only streamline the setup and adjustment of the casting configuration but also enhance the accuracy and repeatability of the geometries produced.

The accuracy of the created second set of prototypes showed promising results. Despite variations in thickness throughout the surface and overall mass differences, the resulting geometries had a high degree of accuracy. As an approach towards improving fabrication accuracy, the alternative fabrication workflow presented in Section 4.1.2 showed promising results. The casting of the mortar in a flat configuration enabled a more uniform and even application of the plaster material. However, the fabrication workflow introduced difficulties with regard to the lifting of the fabric into its final configuration, and the need of adding mortar around the edges due to the deformation of the fabric. The fabrication accuracy can as well be enhanced by further improving the mortar application method. One potential application method could be automated robotic concrete spraying, which has already been used in combination with adaptive mould systems in the ACORN project in [23].

The repeated creation of prototypes using the same piece of fabric successfully demonstrated the reuse potential of the fabric and the system, significantly enhancing its sustainability. Although the fabric exhibited plastic deformation after multiple uses, it was possible to tension it back to nearly its original, unstressed shape. Further research could focus on optimizing the process of restoring the fabric's original shape to mitigate the effects of plastic deformation even more effectively. Additionally, the study found that defects were less critical than initially assumed, indicating the system's robustness against production inaccuracies and imperfections.

The process of manually assembling the individual prototypes into larger combined structures underlined the value of physical modeling. By introducing a haptic and spatial component to the design process, physical modeling facilitated the intuitive creation of complex structures and enabled the finding of not anticipated geometries. Additionally, it provided a preliminary understanding of the structural behavior of the combined structures and the connections between the elements. Future research should explore combinations consisting of a higher number of elements. Due to limitations regarding the size of producible elements, their handling, and transport, a full-scale structure will likely consist of more elements than those tested in this study. The increasing of the number of elements will have implications on the structural performance of the structures and the connection design between the elements, which needs to be investigated.

The connection design between the elements requires particular attention. While the connectors designed in this study were effective during the physical prototyping, a full-size structure will require more detailed connection designs. Although a friction/interlock system, such as the one used here, allows for simple assembly and disassembly, its suitability for full-scale structures is questionable. Besides the potential use of wet joints with grout for connecting elements, dry connections could be particularly interesting, especially in the context of circularity and potential demountability. Future research could explore the incorporation of steel connectors into the edges of the structure during casting.

As briefly mentioned in Section 4.1.2, the textured surface finish of the prototypes not only provides architecturally interesting possibilities but also offers potential for retrospective analysis of stresses in the fabric. In regions of predominantly biaxial stress, the pattern imprinted on the surface remains uniform, whereas it becomes distorted in areas of uniaxial stress. Additionally, it may be possible to infer the magnitude of the stresses by measuring the deformation of the pattern. This could be achieved, for example, by applying a specific type of paint to the surface that accumulates in the pattern's imprints, which can then be scanned and evaluated computationally.

The geometrical analysis provides insights into the accuracy of the built prototypes, and sheds light on the contributions of fabric tensioning and the load of the plaster material to the overall deformation and resulting shape of the structure. In the tested example, the majority of deformation resulted from the weight of the plaster material, due to the low degree of pretensioning of the fabric in the frame. However, it would be interesting to evaluate how this behavior changes with different levels of prestressing in various configurations. Furthermore, comparing the observed deformation behavior with results from ongoing research on the Young's modulus and Poisson's ratio of different fabric patterns could help validate these findings and test their accuracy in different settings.

Additionally, the combined effects of mechanical prestressing and the loading from plaster weight result in interesting effects in the final shape. In stay-in-place applications of the investigated formwork technology, such as the KnitCandela demonstrator, the fabric was stiffened after casting, preventing the plaster material's weight from influencing the geometry [29]. In such exclusively mechanically tensioned structures, without the impact of gravitational or pneumatic loads, only anticlastic shapes can be created. However, by allowing the fabric to deform under the load of the plaster material, new possibilities for the resulting curvatures are introduced. This approach enables the creation of synclastic structures and even structures with both negative and positive Gaussian curvatures, significantly expanding the design spectrum.

5.2. Structural analysis of combined shapes

To design efficient combined structures, it is necessary to understand their mechanical behavior. The structural analysis presented in Section 4.2 significantly contributes to this understanding. As an initial indication of structural performance and an optimization objective, the strain energy stored in the structures was evaluated. Specifically, the ratio between axial strain energy and total strain energy, as well as the bending strain energy, were assessed. While the axial strain energy ratio is a common measure of shell-like behavior, the results indicated that for the analyzed combined structures, this ratio alone cannot serve as a sole performance indicator. In most cases, the configuration with the maximum axial strain energy ratio did not coincide with the one having the minimum total or bending strain energy. Moreover, the findings revealed that the configuration with the minimum bending strain energy generally performed better in terms of limiting tensile stresses compared to the configuration with the maximum axial strain energy ratio. A high axial stress combined with high bending stresses can result in a higher axial strain energy ratio than a configuration with lower bending stress but also lower axial stress, making this indicator less significant on its own. Therefore, it is important to evaluate the bending strain energy alongside axial and total strain energy to identify efficient structural solutions.

For the evaluated combined structures, hinged connections generally appear to be the most suitable. Structurally, they perform significantly better than linked connections and, in most cases, only slightly worse than rigid connections. Moreover, hinged connections are easier to implement in practice compared to rigid connections, which, in the case of in-situ mortar joints, would require connecting reinforcement to transfer moments between the elements. Hinged connections could be realized with simpler in-situ connections or potentially with temporary connectors.

Although the hinged connection variants performed well, they are only possible in configurations, in which the occurrence of mechanism-like effects is prevented. In configurations such as Combination 10, or the ”planar” configurations of Combinations 8 and 6, rigid connections are necessary to ensure the stability of the system. Generally, the results show, that in the design of combined structures, attention must be paid to the avoidance of alignment of flexible joints between elements and regions of single-curvature and low stiffness to prevent mechanism-like effects.

In flexibly formed structures such as those presented in this research, it may seem likely to assume a compression-only structure after inverting the cast form. However, this assumption is not valid for the structures discussed here due to the mechanical properties of the fabric, the combination of mechanical tensioning and mortar weight, the support conditions, and the additional tensioning measures. This is particularly visible in the results of Combinations 2.1 and 2.2. Although one might expect Combination 2.1 to perform better due to the inverted central element, both combinations exhibited similar tensile stresses and Combination 2.2 performed notably better regarding overall deformation. This example suggests that the stiffening effects of the element orientation along its strong axis outweigh the effects of the reversed ”hanging cloth.”

Moreover, a ”vertical stacking” of elements appears to be favorable for the structural performance of the overall combined system. In the tested systems, the performance improved when the supporting elements were oriented as vertically as possible, allowing them to transfer vertical forces from self-weight within their plane. This suggests, that it can be acceptable for one element to act in bending if this orientation allows other supporting elements to transfer loads more effectively in their plane. This effect seems to outweigh the shell behavior of the systems, which can be achieved in more planar configurations of the elements.

5.3. Computational combination

The primary method for producing combined geometries in this research has been the manual combination of the physical prototypes that have been built. In addition to this manual approach, two computational approaches are proposed, and the requirements for their implementation in future work are evaluated. The proposed approaches are described in the following paragraphs.

"Forward": Computational implementation of combinatorial logic

The "*forward*" approach aims to implement the combinatorial logic presented in Section 3.1.3. For this, a *Grasshopper* script has been created, that allows to permute the configurations of a given set of three geometries. The combination of the elements is implemented in a serial way. Firstly, the orientation in space of the first element (E1) is set. Then the edge of the first element, on which the second element (E2) should be connected is chosen as well as the to be connected edge of the second element. Subsequently, the rotation of the second element around the connecting edge is set. Lastly, the process is repeated for the third element (E3) and can potentially be extended and repeated for additional elements. Figure 5.1 illustrates the described process.

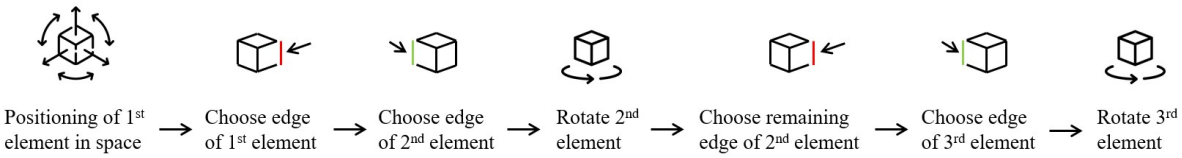

Figure 5.1: "Forward" approach for the computational combination of shell elements

Although the presented implementation allows only for the combination of a specific set of geometries in a given order, it provides a vast range of geometric possibilities. As shown in Figure 5.2 (b) and (c), the design space includes both feasible and unfeasible configurations. While the combination in Figure 5.2 (b) is potentially feasible, the one in (c) is not, as the surfaces intersect and only two corners are on the ground level. This implementation demonstrates the potential of a computational combination approach. Future work can further refine and rationalize this approach by incorporating constraints such as ensuring a sufficient number of supporting corners and preventing surface intersections. For the combination shown in (b), this was partly achieved by optimizing the rotation of the elements to minimize the vertical coordinate of the four supporting corner points.

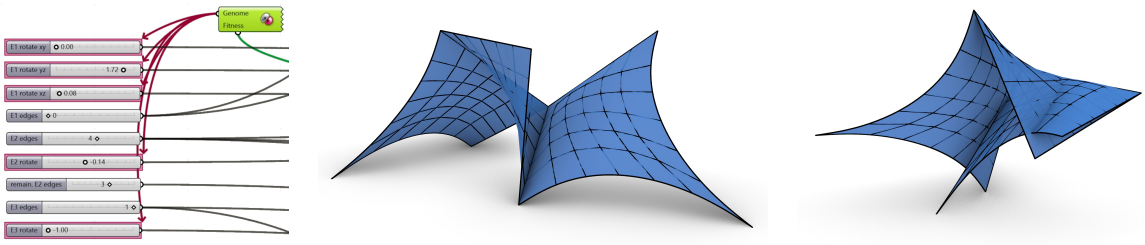

(a) Control parameters (b) Feasible combination (c) Unfeasible combination

Figure 5.2: "Forward" combination approach: (a) Control parameters of the implementation in Grasshopper and (b) feasible and (c) unfeasible resulting combinations

"Backwards": Constraints extracted from frame set up for segmentation

For the "*backward*" approach, the supporting frame presented in Section 4.1.2 is taken as a starting point, and its constraints and parameters are extracted. The constraints are divided into continuous and discrete constraints. The identified continuous constraints, shown in Figure 5.3, involve the spatial positioning of the supporting corner points. The in-plane xy-position of the corner points can be adjusted by moving the columns of the frame, which influences the pre-stressing and sag of the fabric, and which is limited by its maximum stretching capacity. Additionally, the height of the corner points (z-position)

can be adjusted through the laboratory clamps attached to the columns, which influences the curvature of fabric and the load direction relative to the fabric.

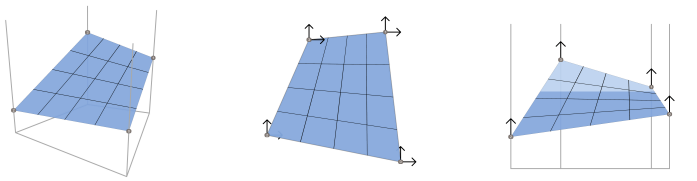

(a) corner points (b) in-plane xy-position (c) vertical z-position

Figure 5.3: Continuous constraints for the ”backwards” approach extracted from the supporting frame

The discrete constraints, extracted from the frame, are the support conditions at the boundary edges and corner points. If point and line supports are considered, the six configurations shown in Figure 5.4 can be realized. In future work, the described continuous and discrete constraints can potentially be used to rationalize the computational segmentation of a geometry that is to be constructed using the fabrication methods and set up presented in Sections 3.2.2 and 4.1.2.

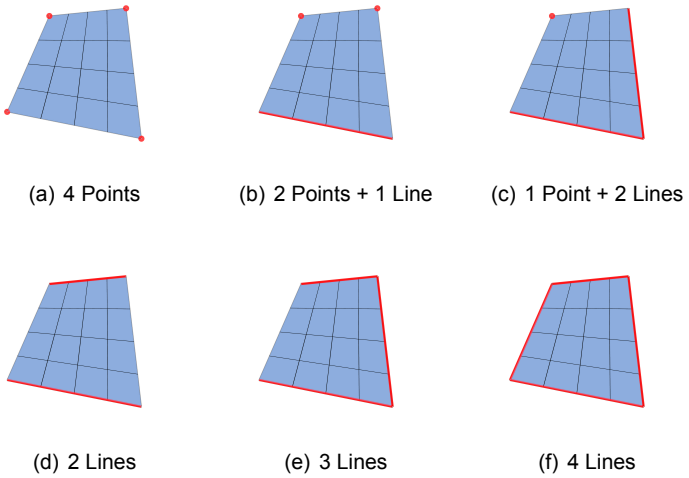

(a) 4 Points (b) 2 Points + 1 Line (c) 1 Point + 2 Lines

(d) 2 Lines (e) 3 Lines (f) 4 Lines

Figure 5.4: Discrete constraints for the ”backwards” approach extracted from the supporting frame

6

Conclusion

This research has successfully demonstrated the potential of reusing a single piece of knitted textile formwork to create a variety of structures with different geometries. By manipulating boundary conditions and support configurations, and using tensioning methods such as cables, rods, and weights, a wide range of shapes can be achieved, significantly expanding the design space for fabric formwork applications. The experimental investigations have shown that complex geometries, with articulated features such as ribs and varying curvatures, can be realized using the same fabric sample. The ability to reuse the fabric formwork for different geometries challenges the conventional application of formwork as a single-use, geometry-specific technology and opens up new possibilities for the shape adaptive fabrication of complex structures.

The repeated reuse of the same fabric sample for casting multiple prototypes demonstrated the material's potential for reducing material consumption. While some plastic deformation was observed after multiple uses, it was found to be mostly reversible, allowing the fabric to be restored to its original shape. Additionally, minor defects in the fabric did not significantly affect its performance or lead to further damage during reuse. These findings highlight the durability and reusability of knitted textile formwork.

Furthermore, the research highlights the importance of considering the interaction between formwork, geometry, and structural performance. The observed variations in structural behavior across different modular configurations emphasize the need for careful consideration of these factors in the design process. The results of this research contribute to the development of a design methodology for combined, modular structures that utilize elements fabricated with the formworking technology presented here. By analyzing the structural behavior of various combined shapes, this study offers valuable insights into the preferable configuration, orientation, and connection of individual elements. These insights can inform the design process, enabling the creation of structurally efficient combined structures. The findings of this research can serve as a foundation for further exploration and refinement of design methodologies for modular construction using flexible formworking technologies.

6.1. Limitations

While this research has yielded promising results, certain limitations have been identified. The accuracy of the built prototypes was limited due to the manual fabrication method, resulting in slightly varying thicknesses of the surfaces, which in turn influenced the resulting shape of the prototypes. Furthermore, the chosen support strategy of the fabric, using rods fed through channels, made it difficult to quantify the tensioning of the fabric precisely. The mortar and SHCC material used in this study, while suitable for small-scale prototypes, would need to be improved and potentially combined with additional reinforcement for larger-scale applications. To gain better insight into the feasibility of upscaling the proposed technology, larger prototypes and combined structures need to be built and tested.

In this research, computationally form-found models were used for the structural analysis of the combined structures. While this approach offered a simplified representation of the physical prototypes,

utilizing for example 3D scans could provide more realistic results, especially in areas prone to stress concentrations, such as the slender support corners of the Geometry 1 elements. These stress concentrations due to idealized point supports and connections in the models, could be avoided by using rounded or angled corners and distributed supports. Additionally, the linear elastic analysis employed in this study, does not provide reliable results for the cases, in which large deformations occur, and can not describe buckling or the non-linear behaviour of the interlocking system applied in the physical prototypes. Furthermore, the current analysis focused solely on self-weight loading, not taking into account other potential load cases such as lateral wind loads or localized live loads.

6.2. Summary of future work

Building upon the findings of this research, various possibilities for future work and further investigations were identified. These include testing more tensioning methods and boundary/support variations to further explore the design space of fabric formwork. Additionally, conducting further investigations into the behavior of different knit patterns regarding the resulting dimensions of the knitted elements and their deformation behavior is necessary to better predict resulting geometries. Related to this, methods to restore the fabric's original shape more effectively after plastic deformation could be investigated, enhancing the fabric's reusability. Also, exploring the potential of using the textured surface finish of the prototypes to assess textile stresses, as mentioned in the discussion, can provide insights into the internal forces within the fabric.

Improving the presented frame design by potentially automating it, as described in Section 5.1, can further enhance accuracy and efficiency in the fabrication process. Testing additional fabrication workflows, such as robotic concrete spraying, could further improve the accuracy and control of the mortar application process, as well as the aforementioned automation of the process. Furthermore, upscaling the physical prototypes to larger dimensions in future research will help understand the behavior of the fabric formwork and combined structures at a larger scale, assessing the feasibility of industry applications. This would require further development of connection details, exploring both dry and wet connection methods.

In future research, the FE-analysis should be refined, for more realistic representations of the mechanical behaviour of the combined structures. Non-linear analysis can be applied to gain insights into the behaviour of configurations exhibiting large deformations and the risk of buckling, and to better simulate the behavior of the connections between elements, particularly for compression-only connections. Furthermore, alternative load cases, such as lateral wind loads or localized live loads, should be investigated, to understand the structures' responses to various load scenarios.

Lastly, implementing the in Section 5.3 proposed approaches for ”forward” computational combination of shapes and ”backward” rationalization of surface segmentation using the constraints extracted from the frame setup can open new possibilities for the design process and for the exploration of a wider range of possible geometries.

References

[1] Adapa. *Adaptive Mould D200*. URL: https://adapamoulds.com/portfolio-item/adaptive-mould-d200-2/.

[2] International Energy Agency. “Energy Technology Perspectives 2020”. In: (2020). URL: https://www.iea.org/reports/energy-technology-perspectives-2020.

[3] Giulia Boller and Pierluigi D’Acunto. “Structural design via form finding: Comparing Frei Otto, Heinz Isler and Sergio Musmeci”. In: July 2021.

[4] J.C Chilton. “39 etc... : Heinz Isler’s infinite spectrum of new shapes for shells”. In: (Sept. 2009).

[5] Intergovernmental Panel on Climate change. “IPCC, 2022: Technical Summary”. In: *Climate Change 2022: Mitigation of Climate Change. Contribution of Working Group III to the Sixth Assessment Report of the Intergovernmental Panel on Climate Change* (2022). DOI: 10.1017/9781009157926.002.

[6] Julian Lowell Coolidge. *A History of the Conic Sections and Quadric Surfaces*. Dover Publications, 1968.

[7] Eduardo Costa et al. “Computational design exploration of a segmented concrete shell building floor system”. In: *Proceedings of the Institution of Civil Engineers - Structures and Buildings* 176 (Mar. 2023), pp. 1–32. DOI: 10.1680/jstbu.22.00156.

[8] Deborah DeHovitz. “The Platonic Solids: An Exploration of the Five Regular Polyhedra and the Symmetries of Three-Dimensional Space”. In: 2016. URL: https://api.semanticscholar.org/CorpusID:36719344.

[9] H. Engel and H. Bandel. *Tragsysteme: Structure systems*. Deutsche Verlagsanst., 1967.

[10] C. Faber. *Candela, the Shell Builder*. Candela: The Shell Builder v. 10. Reinhold Publishing Corporation, 1963. URL: https://books.google.nl/books?id=BharvgEACAAJ.

[11] Lucy Flieger. “Flexible Formwork: A Textile-Centric Approach - Investigating pattern influence on the deformation behavior of weft-knitted textiles under hydrostatic loading”. MA thesis. Delft University Of Technology, 2024. URL: http://resolver.tudelft.nl/uuid:c19a29a5-a2b1-489f-b83b-94cb4c58a94a.

[12] O P Gibbons et al. “How to calculate embodied carbon (2nd edition)”. In: *IStructE Guide* (2022).

[13] Steffen Grunewald et al. “Deliberate deformation of concrete after casting”. In: June 2012.

[14] Will J Hawkins et al. “Flexible formwork technologies–a state of the art review”. In: *Structural Concrete* 17.6 (2016), pp. 911–935.

[15] Hamid Jafarbiglu and Alireza Pourreza. “A comprehensive review of remote sensing platforms, sensors, and applications in nut crops”. In: *Computers and Electronics in Agriculture* 197 (2022), p. 106844. ISSN: 0168-1699. DOI: https://doi.org/10.1016/j.compag.2022.106844. URL: https://www.sciencedirect.com/science/article/pii/S0168169922001612.

[16] Anass Kariouh. “Flexibly formed concrete: Exploiting the deformation behaviour of weft-knitted formworks caused by concrete pressure”. MA thesis. Delft University Of Technology, 2023.

[17] Anass Kariouh and Mariana Popescu. “(Unpublished) Reusable flexible formworks for constructing complex concrete structures”. In: *4th RILEM International Conference on Concrete and Digital Fabrication* (2024).

[18] Cornelie Leopold. “Geometry Concepts In Architectural Design”. In: 2006. URL: https://api.semanticscholar.org/CorpusID:220380565.

[19] Qingpeng Li. “Form Follows Force: A theoretical framework for Structural Morphology, and Form-Finding research on shell structures”. PhD thesis. Mar. 2018. DOI: 10.7480/abe.2018.2.

[20] Wei Li et al. “A review of formwork systems for modern concrete construction”. In: *Structures* 38 (2022), pp. 52–63. ISSN: 2352-0124. DOI: https://doi.org/10.1016/j.istruc.2022.01.089. URL: https://www.sciencedirect.com/science/article/pii/S2352012422000911.

[21] Hao Long et al. “Distribution Features of Deviation and Determination of a Tolerance Method for Prefabricated Concrete Components”. In: *Buildings* 13.5 (2023). ISSN: 2075-5309. DOI: 10.3390/buildings13051142. URL: https://www.mdpi.com/2075-5309/13/5/1142.

[22] Mladena Luković et al. “Strain Hardening Cementitious Composite (SHCC) for crack width control in reinforced concrete beams”. In: *Heron* 64.1/2 (2019), p. 181.

[23] Mishael Nuh et al. “Digital fabrication of ribbed concrete shells using automated robotic concrete spraying”. In: *Additive Manufacturing* 59 (2022), p. 103159. ISSN: 2214-8604. DOI: https://doi.org/10.1016/j.addma.2022.103159. URL: https://www.sciencedirect.com/science/article/pii/S2214860422005486.

[24] John Orr et al. “Concrete structures using fabric formwork”. In: *The Structural Engineer* 89 (Apr. 2011), pp. 20–26. DOI: 10.17863/CAM.17019.

[25] Frei Otto. “Tensile structure diagrams”. In: *Casabella* 301 (1966), p. 35.

[26] Robin Oval et al. “Creasing the British Museum: Topology Finding of Crease Patterns for Shell Structures”. In: *Journal of the International Association for Shell and Spatial Structures* 65.1 (2024), pp. 44–56. DOI: doi:10.20898/j.iass.2024.004. URL: https://www.ingentaconnect.com/content/iass/jiass/2024/00000065/00000001/art00007.

[27] Daniel Piker. “Kangaroo: Form Finding with Computational Physics”. In: *Architectural Design* 83.2 (2013), pp. 136–137. DOI: https://doi.org/10.1002/ad.1569. eprint: https://onlinelibrary.wiley.com/doi/pdf/10.1002/ad.1569. URL: https://onlinelibrary.wiley.com/doi/abs/10.1002/ad.1569.

[28] M. Popescu et al. “Building in Concrete with an Ultra-lightweight Knitted Stay-in-place Formwork: Prototype of a Concrete Shell Bridge”. In: *Structures* 14 (2018), pp. 322–332. ISSN: 2352-0124. DOI: https://doi.org/10.1016/j.istruc.2018.03.001. URL: https://www.sciencedirect.com/science/article/pii/S2352012418300262.

[29] Mariana Popescu et al. “Structural design, digital fabrication and construction of the cable-net and knitted formwork of the KnitCandela concrete shell”. In: *Structures*. Vol. 31. Elsevier. 2021, pp. 1287–1299.

[30] Mariana Adriana Popescu. “KnitCrete: Stay-in-place knitted formworks for complex concrete structures”. PhD thesis. ETH Zurich, 2019.

[31] Helmut Pottmann et al. *Architectural Geometry*. Bentley Institute Press, 2007. ISBN: 9781934493045.

[32] Clemens Preisinger. “Linking Structure and Parametric Geometry”. In: *Architectural Design* 83 (Mar. 2013). DOI: 10.1002/ad.1564.

[33] Christian Raun and Adapa. “Adaptive mould-A cost-effective mould system linking design and manufacturing of double-curved GFRC panels”. In: 2016. URL: https://api.semanticscholar.org/CorpusID:84837548.

[34] Christopher Rausch, Chloe Edwards, and Carl Haas. “Benchmarking and Improving Dimensional Quality on Modular Construction Projects – A Case Study”. In: *International Journal of Industrialized Construction* 1.1 (2020), pp. 2–21. DOI: 10.29173/ijic212.

[35] Martin H. Sadd. “Chapter 6 - Strain Energy and Related Principles”. In: *Elasticity (Second Edition)*. Ed. by Martin H. Sadd. Second Edition. Boston: Academic Press, 2009, pp. 113–133. ISBN: 978-0-12-374446-3. DOI: https://doi.org/10.1016/B978-0-12-374446-3.50010-8. URL: https://www.sciencedirect.com/science/article/pii/B9780123744463500108.

[36] Diederik Veenendaal, Mark West, and Philippe Block. “History and overview of fabric formwork: using fabrics for concrete casting”. In: *Structural Concrete* 12.3 (2011), pp. 164–177.

[37] Krittika Walia, Robin Oval, and Olivier Baverel. “FAB Shell (Fabric–Arch–Base Shell): Concrete shell building using fabric membranes and telescopic arches as formwork”. In: *Proceedings of IASS Annual Symposia*. Vol. 2020. 20. International Association for Shell and Spatial Structures (IASS). 2020, pp. 1–12.

[38] M. West. *The Fabric Formwork Book: Methods for Building New Architectural and Structural Forms in Concrete*. Taylor & Francis, 2016. ISBN: 9781317380924. URL: https://books.google.nl/books?id=1At6DQAAQBAJ.

[39] Yue Wu, Yi Xia, and Qingpeng Li. “Structural morphogenesis of free-form shells by adjusting the shape and thickness”. In: *Proceedings of IASS Annual Symposia* 2015.17 (2015), pp. 1–14. URL: https://www.ingentaconnect.com/content/iass/piass/2015/00002015/00000017/art00014.

[40] Jian Zhou et al. “Development of engineered cementitious composites with limestone powder and blast furnace slag”. In: *Materials and Structures* 43 (July 2010), pp. 803–814. DOI: 10.1617/s11527-009-9549-0.

A

Summary of results

A.1. Overview

A.1.1. Overview of strain energy analysis results

No.	Con.	Rot.	Covered volume [m3]	Total strain energy [kNm]	Bending strain energy [kNm]	Axial strain energy [kNm]	Axial strain energy ratio [%]	Tot. strain energy per cov. volume [Nm/m3]
8	Linked	0°	52,07	0,307	0,239	0,068	22,2	5,90
		-7,2°	50,07	0,157	0,071	0,086	54,8	3,14
		23,4°	57,57	0,079	0,050	0,029	36,4	1,37
	Hinged	0°	52,07	0,155	0,106	0,049	31,6	2,98
		-9,0°	49,53	0,111	0,044	0,067	60,5	2,24
		12,6°	55,19	0,066	0,035	0,031	46,9	1,20
	Rigid	0°	52,07	0,112	0,072	0,040	36,0	2,15
		-9,0°	49,53	0,105	0,042	0,063	59,9	2,12
		12,6°	55,19	0,057	0,030	0,027	47,4	1,03
6	Linked	0°	81,59	0,329	0,250	0,079	23,9	4,03
		-7,2°	79,39	0,317	0,203	0,114	36	3,99
		37,8°	80,81	0,160	0,121	0,039	24,4	1,98
	Hinged	0°	81,59	0,192	0,115	0,077	40,2	2,35
		-10,8°	78,09	0,219	0,114	0,105	48,0	2,80
		37,8°	80,81	0,104	0,060	0,044	42,1	1,29
	Rigid	0°	81,59	0,170	0,098	0,072	42,5	2,08
		-19,8°	74,26	0,282	0,146	0,136	48,2	3,80
		37,8°	80,81	0,104	0,060	0,044	42,1	1,29
10	Linked	-	163,38	0,819	0,680	0,139	17,0	5,01
	Hinged	-	163,38	0,627	0,520	0,107	17,0	3,84
	Rigid	-	163,38	0,102	0,060	0,042	41,0	0,62
5	Linked	37,8°	37,75	0,295	0,247	0,048	16,4	7,83
		84,6°	53,47	0,019	0,011	0,008	42,8	0,36
	Hinged	37,8°	37,75	0,109	0,076	0,033	30,2	2,88
		84,6°	53,47	0,015	0,008	0,007	47,0	0,28
	Rigid	37,8°	37,75	0,108	0,075	0,033	30,7	2,87
		84,6°	53,47	0,015	0,008	0,007	47,3	0,28
2.1	Linked	33,3°	191,57	0,365	0,247	0,118	32,4	1,91
		28,8°	205,01	0,313	0,218	0,095	30,3	1,53

	Hinged	29,7°	202,47	0,300	0,162	0,138	46,0	1,48
		21,6°	222,31	0,201	0,118	0,083	41,2	0,90
	Rigid	28,8°	205,01	0,202	0,125	0,077	38,2	0,99
		21,6°	222,31	0,179	0,114	0,065	36,3	0,81
2.2	Linked	-22,5°	211,97	0,270	0,200	0,070	25,9	1,27
		-10,8°	228,63	0,217	0,162	0,055	25,2	0,95
	Hinged	-12,6°	227,16	0,161	0,096	0,065	40,5	0,71
		-8,1°	230,08	1,449	0,881	0,568	39,2	6,30
	Rigid	-18,0°	220,32	0,100	0,059	0,041	41,1	0,45
		-9,9°	229,22	0,091	0,054	0,037	40,4	0,40
19	Linked	-	82,19	0,018	0,009	0,009	47,9	0,22
	Hinged	-	82,19	0,010	0,005	0,005	49,7	0,12
	Rigid	-	82,19	0,010	0,005	0,005	49,5	0,12
20	Linked	-	74,11	0,020	0,009	0,011	54,0	0,27
	Hinged	-	74,11	0,013	0,006	0,007	54,7	0,18
	Rigid	-	74,11	0,012	0,005	0,007	55,2	0,16

Table A.1: Overview of the results of the strain energy analyses of the different combinations

A.1.2. Overview of deformation and stress analysis results

No.	Con.	Rot.	Max. deformation	Max. tensile stress	Surface area exceeding tensile limit
			[mm]	[N/mm2]	[%]
8	Linked	0°	234,4	88,0	29,49
		-7,2°	30,4	18,6	5,64
		23,4°	35,0	22,1	1,35
	Hinged	0°	118,9	44,0	8,70
		-9,0°	30,0	16,2	4,65
		12,6°	23,3	17,1	1,22
	Rigid	0°	27,4	19,6	7,16
		-9,0°	17,9	14,8	2,76
		12,6°	20,7	13,8	1,79
6	Linked	0°	159,1	73,6	28,56
		-7,2°	129,0	31,4	13,74
		37,8°	121,2	22,8	10,8
	Hinged	0°	85,0	51,0	8,30
		-10,8°	96,8	18,3	6,50
		37,8°	77,5	20,2	2,40
	Rigid	0°	84,6	17,8	5,40
		-19,8°	130,1	20,2	7,90
		37,8°	72,7	15,5	1,70
10	Linked	-	208,1	58,2	44,01
	Hinged	-	185,9	54,2	37,38
	Rigid	-	11,9	5,0	3,15
5	Linked	37,8°	208,5	66,8	21,40
		84,6°	11,4	6,4	0,00
	Hinged	37,8°	201,2	67,0	21,10
		84,6°	12,8	6,5	0,00
	Rigid	37,8°	63,3	25,7	6,80
		84,6°	11,5	6,1	0,00
2.1	Linked	33,3°	-	-	-

		28,8°	81,7	100,3	15,75
	Hinged	29,7°	-	-	-
		21,6°	46,1	46,0	4,31
	Rigid	28,8°	-	-	-
		21,6°	39,7	18,2	13,68
2.2	Linked	-22,5°	-	-	-
		-10,8°	60,1	66,4	7,43
	Hinged	-12,6°	-	-	-
		-8,1°	40,1	50,7	4,49
	Rigid	-18,0°	-	-	-
		-9,9°	27,2	14,5	4,47
19	Linked	-	5,1	4,2	0,00
	Hinged	-	4,1	3,6	0,00
	Rigid	-	3,7	3,3	0,00
20	Linked	-	4	8,4	0,23
	Hinged	-	3,7	5,4	0,16
	Rigid	-	1,8	4,2	0,03

Table A.2: Overview of the results of the deformation and stress analyses of the different combinations

A.2. Strain energy analysis results

A.2.1. Combination 8

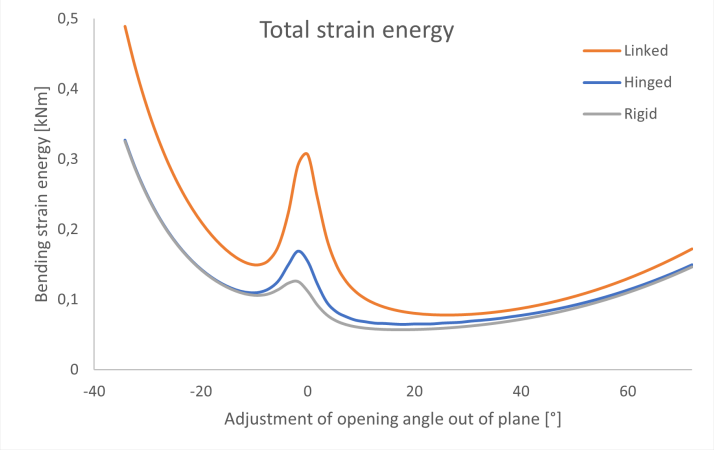

(a) Total strain energy (total = axial + bending)

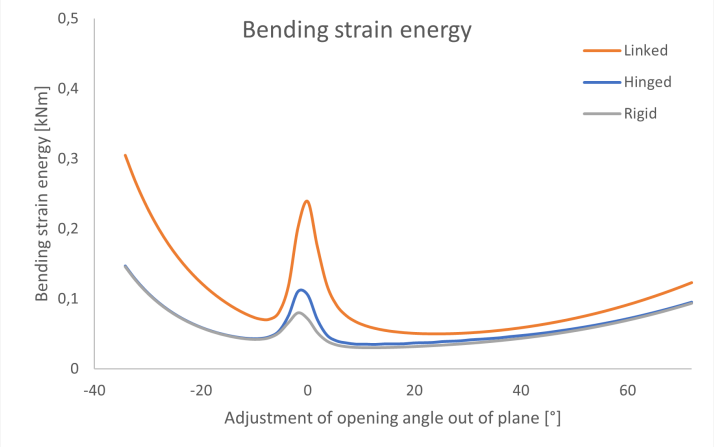

(b) Bending strain energy (bending)

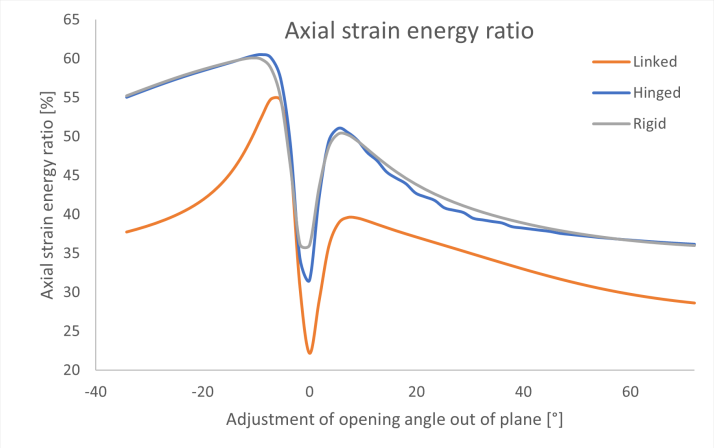

(c) Axial strain energy ratio (ratio = axial / total)

Figure A.1: Combination 8: (a) Total strain energy, (b) bending strain energy, and (c) axial strain energy ratio depending on angle variation and for different connection types

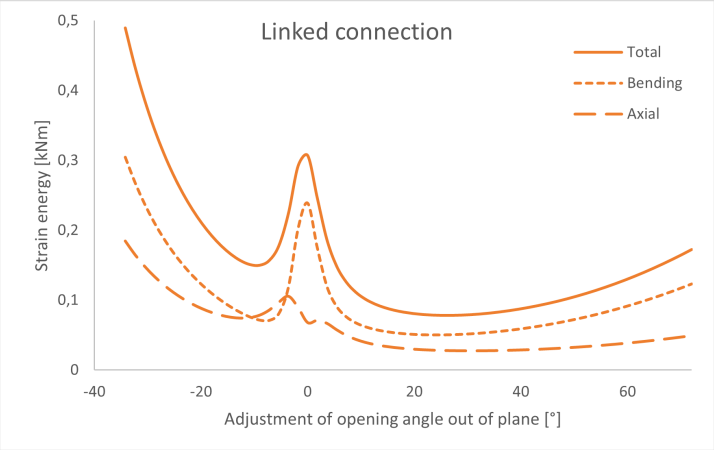

(a) Total strain energy contributions - linked connection

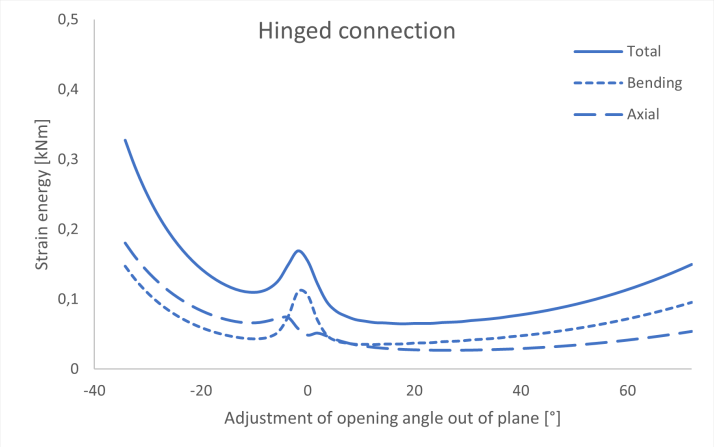

(b) Total strain energy contributions - hinged connection

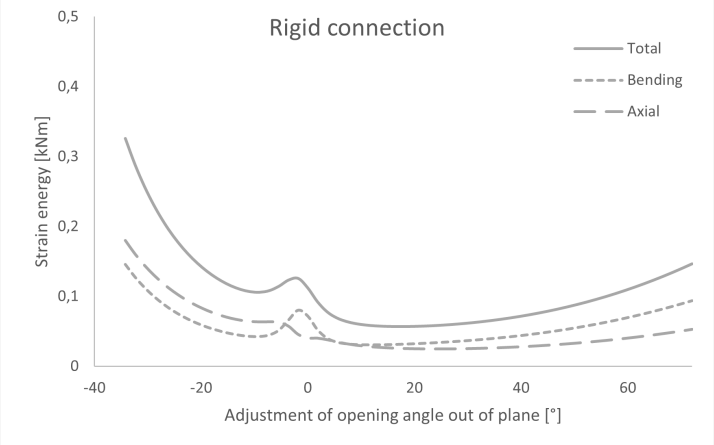

(c) Total strain energy contributions - rigid connection

Figure A.2: Combination 8: Contributions to the total strain energy for (a) linked connection, (b) hinged connection and (c) rigid connection depending on opening angle

A.2.2. Combination 6

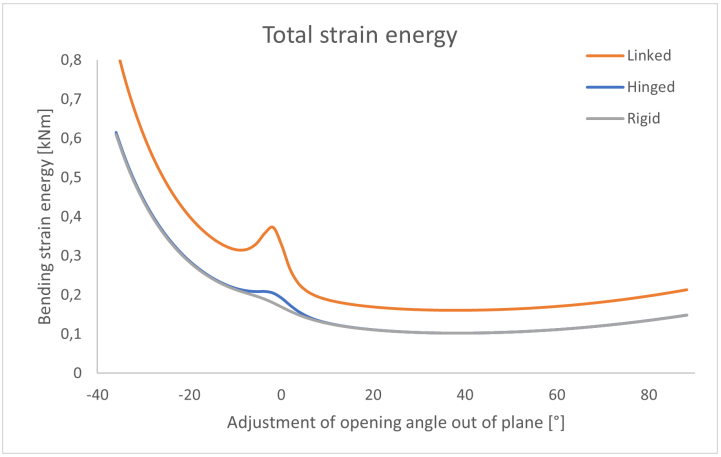

(a) Total strain energy (total = axial + bending)

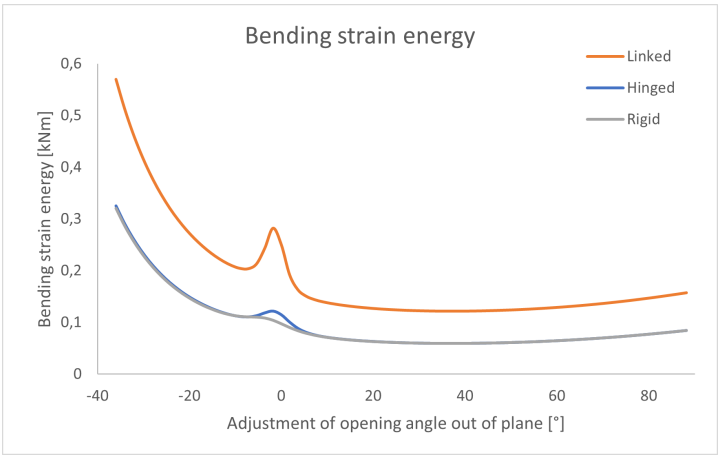

(b) Bending strain energy (bending)

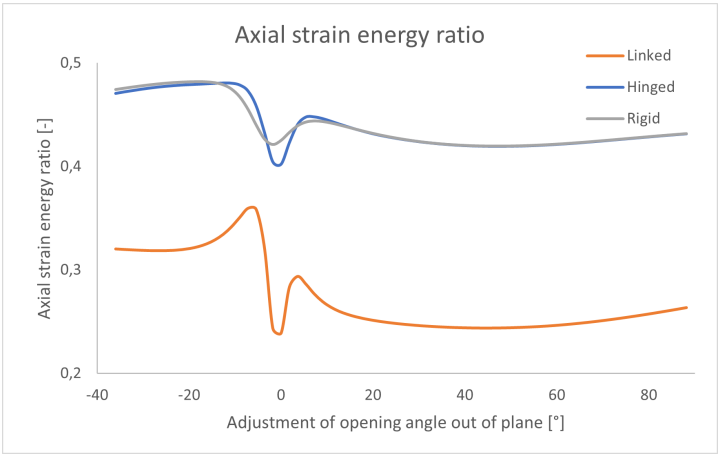

(c) Axial strain energy ratio (ratio = axial / total)

Figure A.3: Combination 6: (a) Total strain energy, (b) bending strain energy, and (c) axial strain energy ratio depending on angle variation and for different connection types

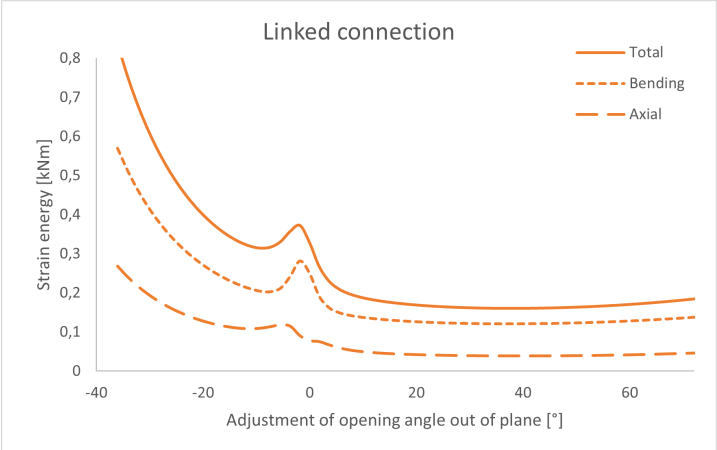

(a) Total strain energy contributions - linked connection

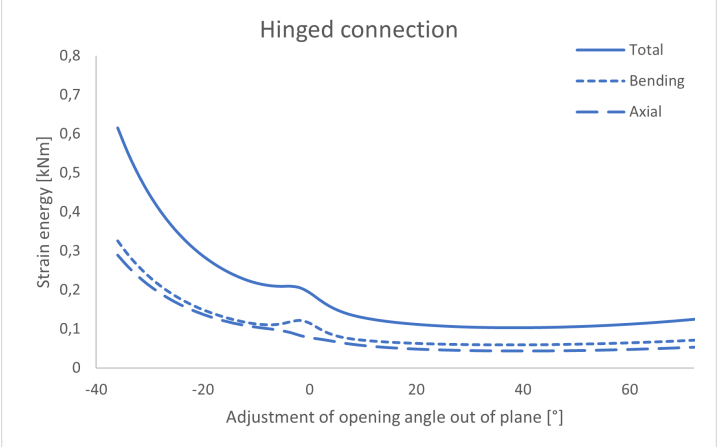

(b) Total strain energy contributions - hinged connection

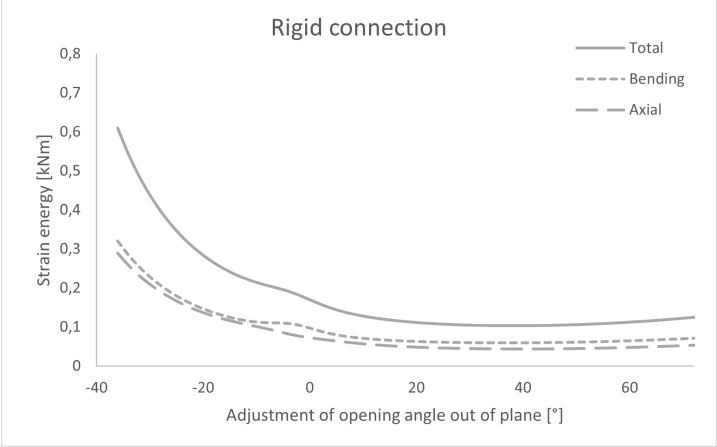

(c) Total strain energy contributions - rigid connection

Figure A.4: Combination 6: Contributions to the total strain energy for (a) linked connection, (b) hinged connection and (c) rigid connection depending on opening angle

A.2.3. Combination 10

Connection	Total SE [kNm]	Bending SE [kNm]	Axial SE [kNm]	Axial SE ratio [%]
linked	0.82	0.68	0.14	17
hinged	0.63	0.52	0.11	17
rigid	0.10	0.06	0.04	41

Table A.3: Combination 10: Results of the strain energy (SE) analysis

A.2.4. Combination 5

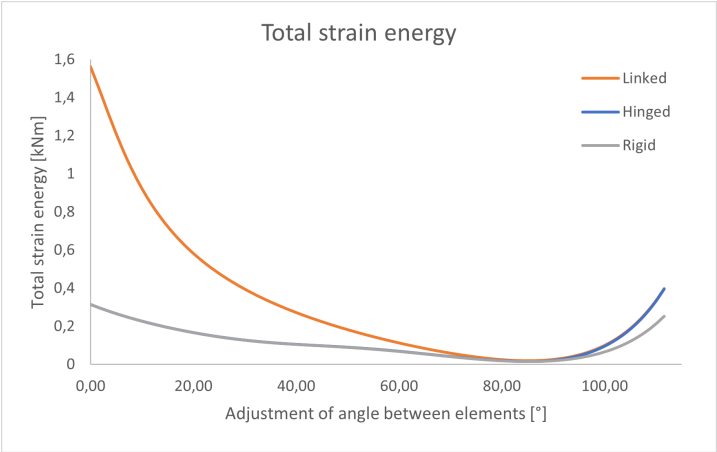

(a) Total strain energy (total = axial + bending)

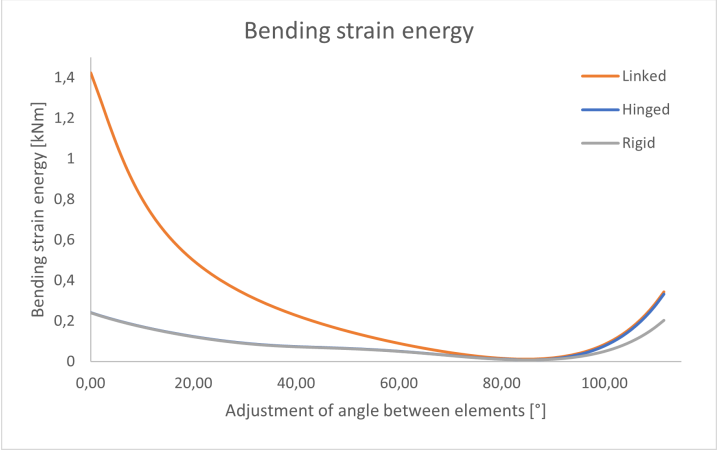

(b) Bending strain energy (bending)

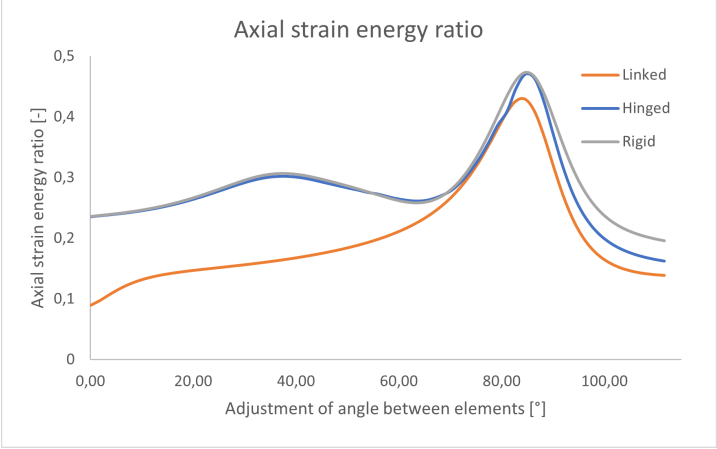

(c) Axial strain energy ratio (ratio = axial / total)

Figure A.5: Combination 5: (a) Total strain energy, (b) bending strain energy, and (c) axial strain energy ratio depending on angle variation and for different connection types

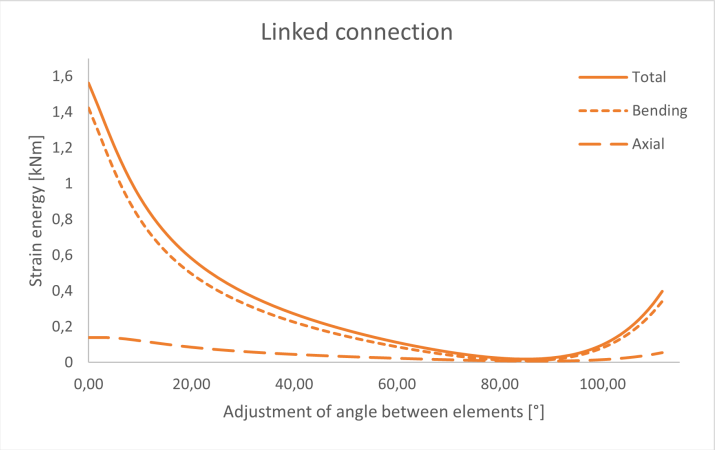

(a) Total strain energy contributions - linked connection

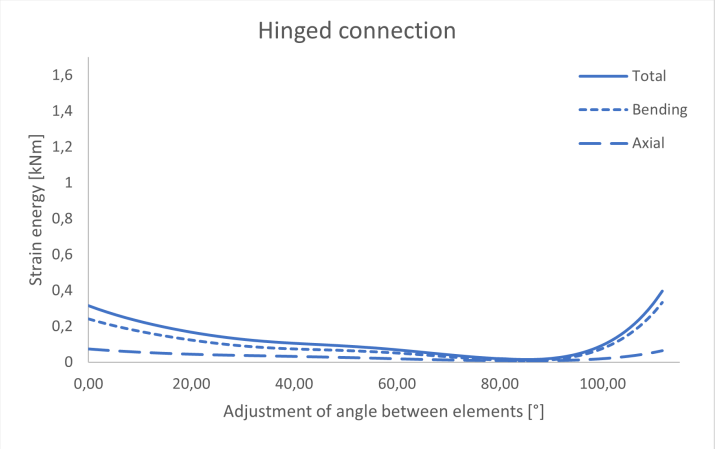

(b) Total strain energy contributions - hinged connection

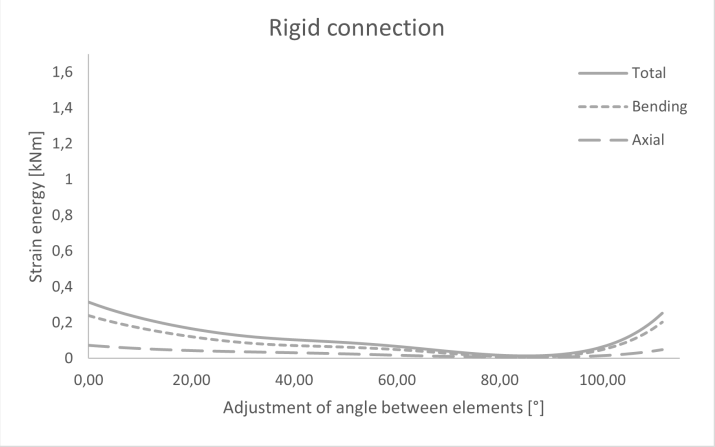

(c) Total strain energy contributions - rigid connection

Figure A.6: Combination 5: Contributions to the total strain energy for (a) linked connection, (b) hinged connection and (c) rigid connection depending on opening angle

A.2.5. Combination 2.1

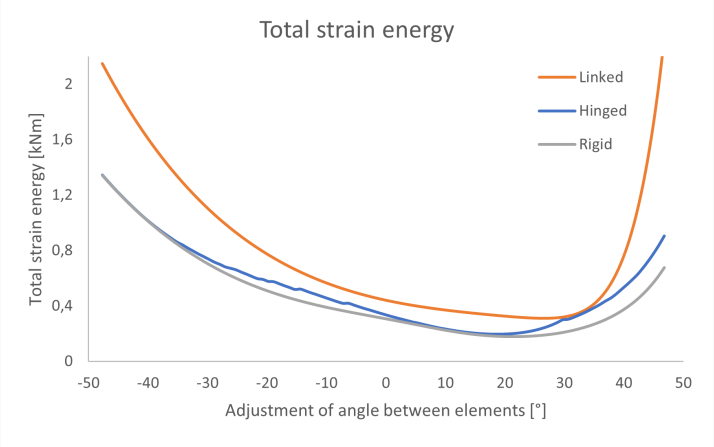

(a) Total strain energy (total = axial + bending)

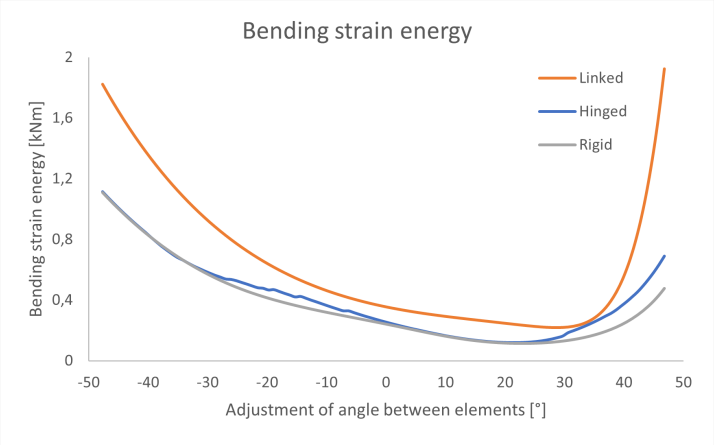

(b) Bending strain energy (bending)

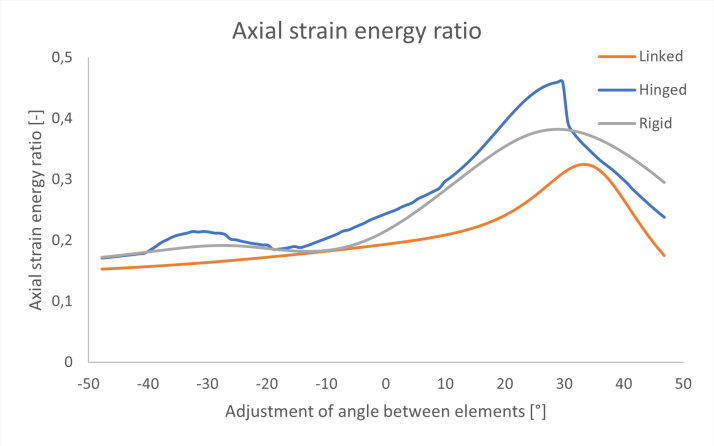

(c) Axial strain energy ratio (ratio = axial / total)

Figure A.7: Combination 2.1: (a) Total strain energy, (b) bending strain energy, and (c) axial strain energy ratio depending on angle variation and for different connection types

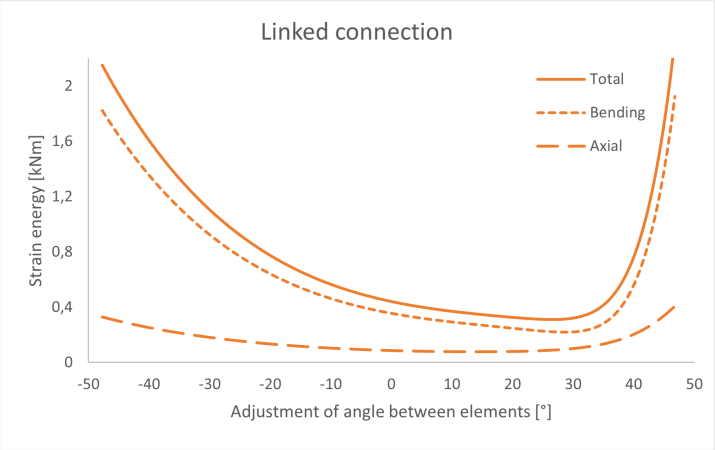

(a) Total strain energy contributions - linked connection

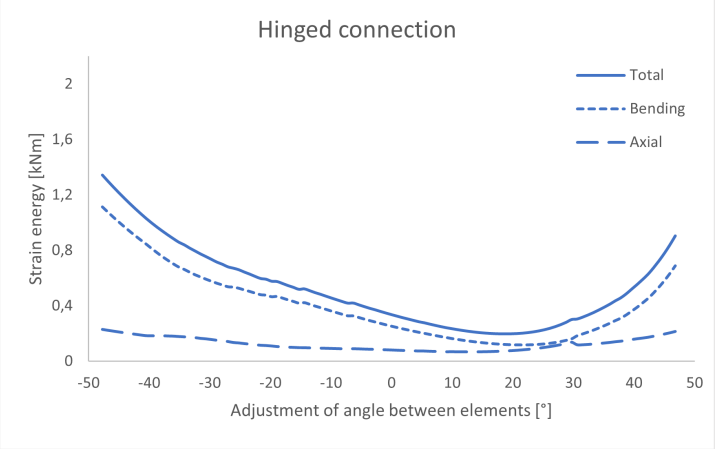

(b) Total strain energy contributions - hinged connection

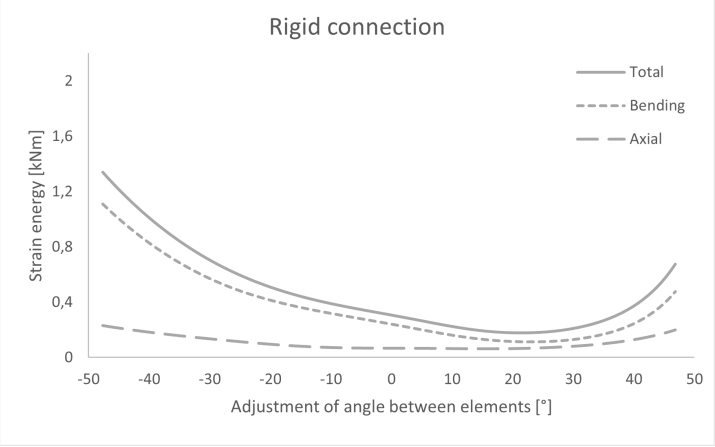

(c) Total strain energy contributions - rigid connection

Figure A.8: Combination 2.1: Contributions to the total strain energy for (a) linked connection, (b) hinged connection and (c) rigid connection depending on opening angle

A.2.6. Combination 2.2

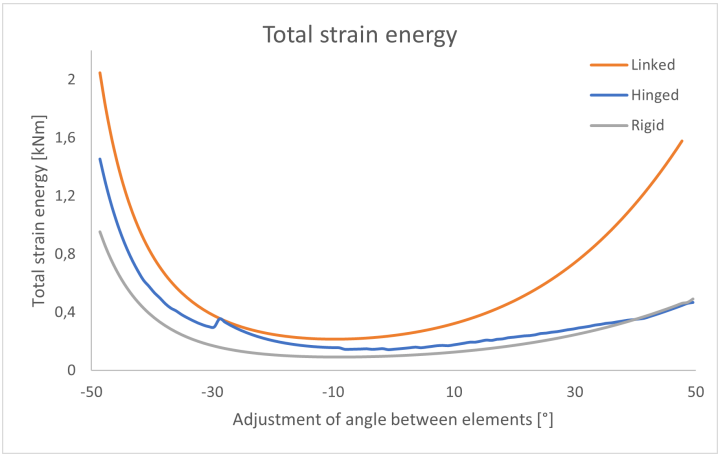

(a) Total strain energy (total = axial + bending)

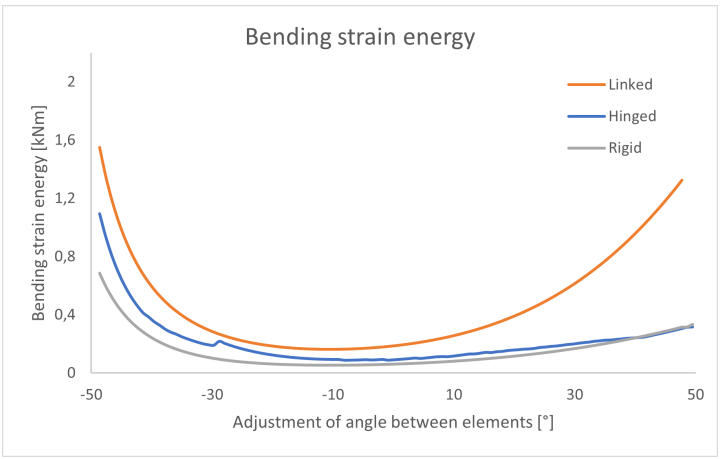

(b) Bending strain energy (bending)

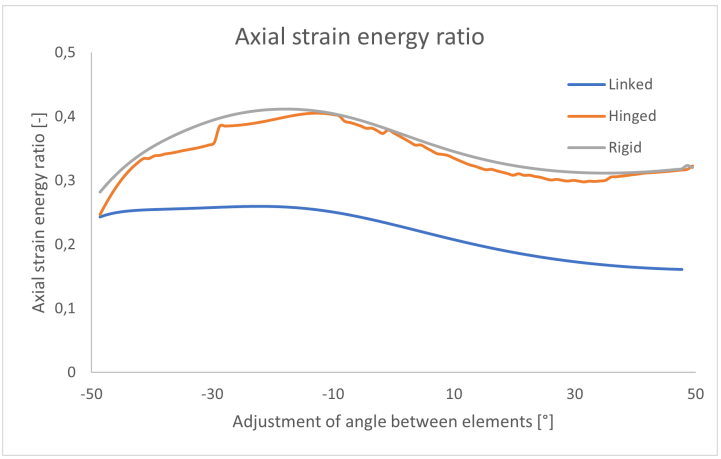

(c) Axial strain energy ratio (ratio = axial / total)

Figure A.9: Combination 2.2: (a) Total strain energy, (b) bending strain energy, and (c) axial strain energy ratio depending on angle variation and for different connection types

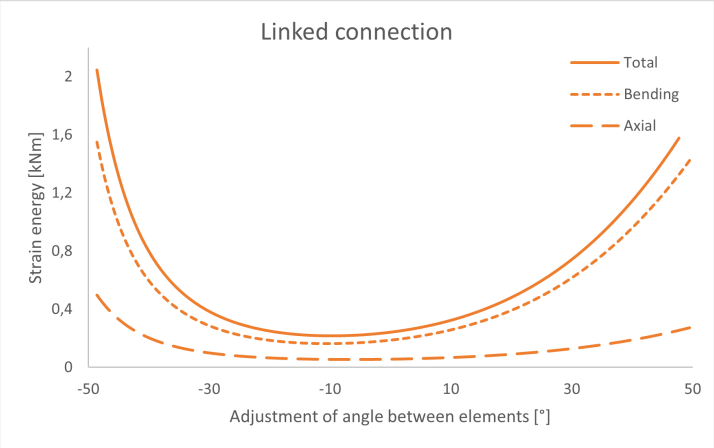

(a) Total strain energy contributions - linked connection

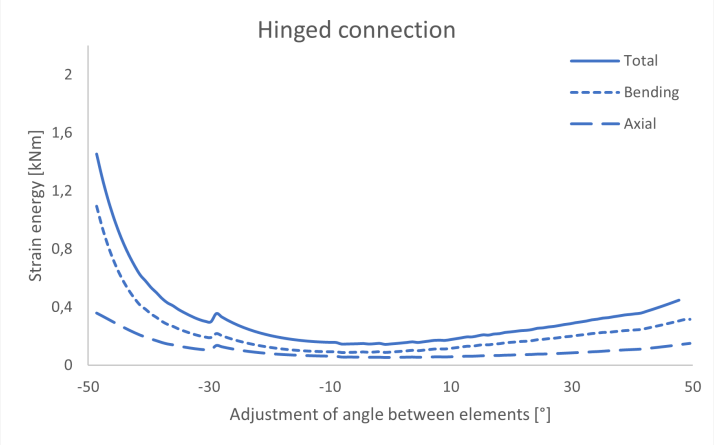

(b) Total strain energy contributions - hinged connection

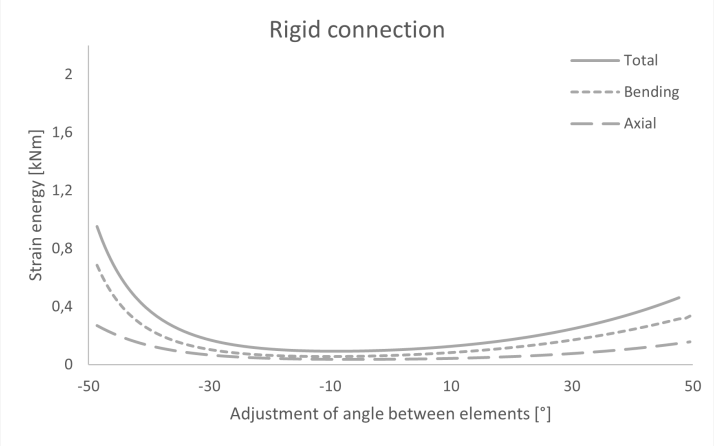

(c) Total strain energy contributions - rigid connection

Figure A.10: Combination 2.2: Contributions to the total strain energy for (a) linked connection, (b) hinged connection and (c) rigid connection depending on opening angle

A.2.7. Combination 19

Connection	Total SE [kNm]	Bending SE [kNm]	Axial SE [kNm]	Axial SE ratio [%]
linked	$1.79 * 10^-2$	$9.32 * 10^-3$	$8.57 * 10^-3$	47.9
hinged	$9.94 * 10^-3$	$5.00 * 10^-3$	$4.94 * 10^-3$	49.7
rigid	$9.84 * 10^-3$	$4.97 * 10^-3$	$4.87 * 10^-3$	49.5

Table A.4: Combination 19 & 20: Results of the strain energy (SE) analysis

A.2.8. Combination 20

Connection	Total SE [kNm]	Bending SE [kNm]	Axial SE [kNm]	Axial SE ratio [%]
linked	$2.02 * 10^-2$	$9.27 * 10^-3$	$1.09 * 10^-2$	54.0
hinged	$1.26 * 10^-2$	$5.69 * 10^-3$	$6.87 * 10^-3$	54.7
rigid	$1.18 * 10^-2$	$5.28 * 10^-3$	$6.51 * 10^-3$	55.2

Table A.5: Combination 19 & 20: Results of the strain energy (SE) analysis

A.3. Stress analysis results

A.3.1. Combination 8

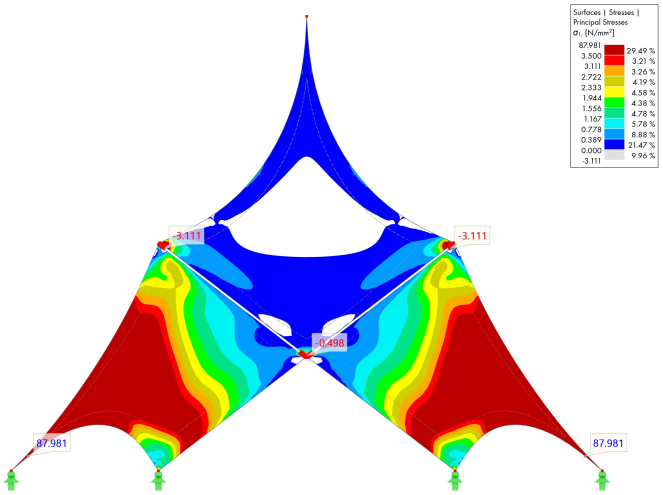

(a) Linked: 0°

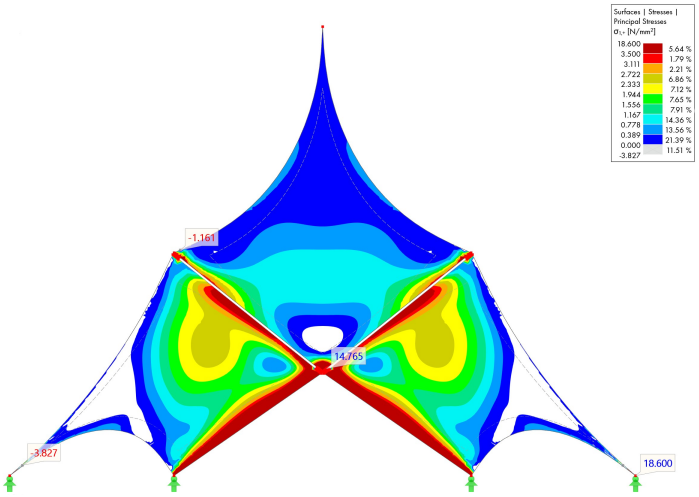

(b) Linked: -7.2°

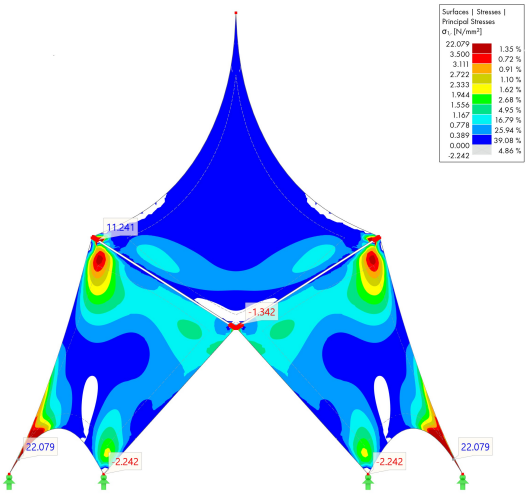

(c) Linked: 23.4°

Figure A.11: Combination 8 - Linked: Tensile stresses under self-weight for rotation angles (a) 0°, (b) -7.2°, and (c) 23.4°

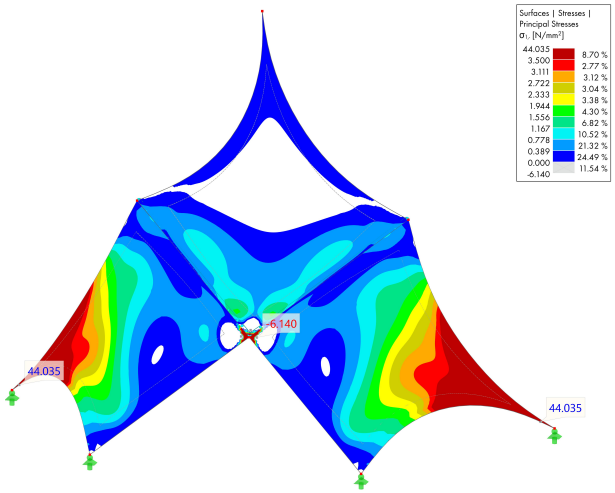

(a) Hinged: 0°

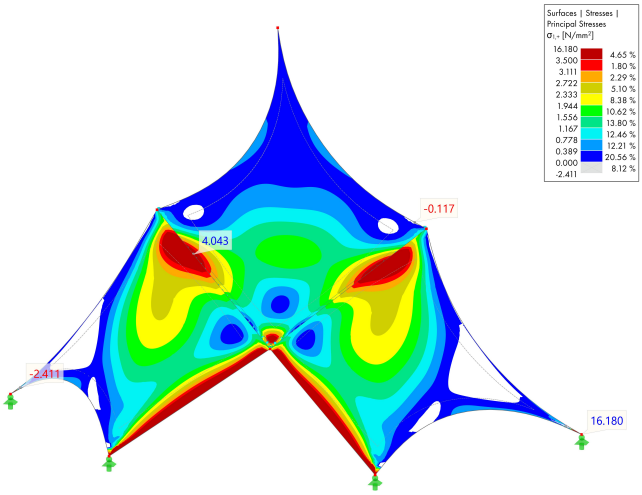

(b) Hinged: -9.0°

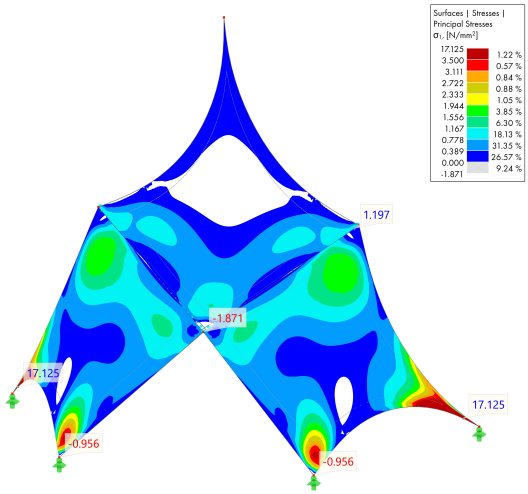

(c) Hinged: 12.6°

Figure A.12: Combination 8 - Hinged: Tensile stresses under self-weight for rotation angles (a) 0°, (b) -9.0°, and (c) 12.6°

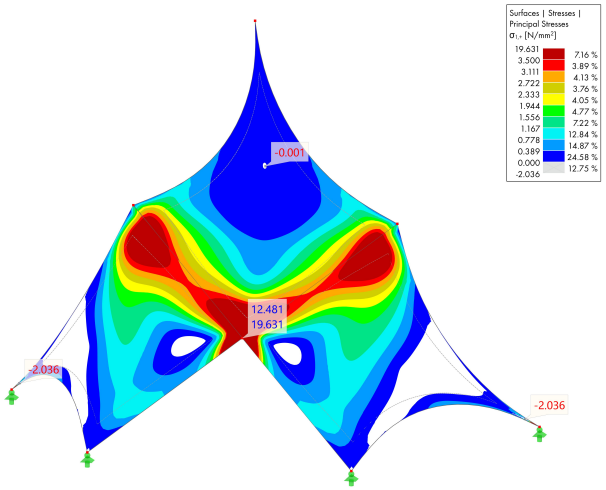

(a) Rigid: 0°

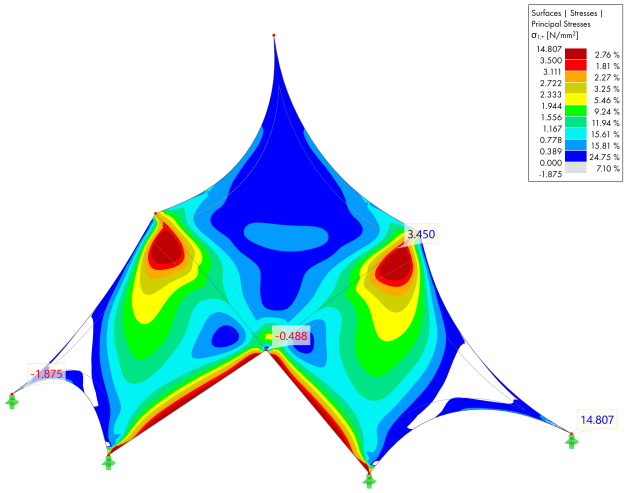

(b) Rigid: -9.0°

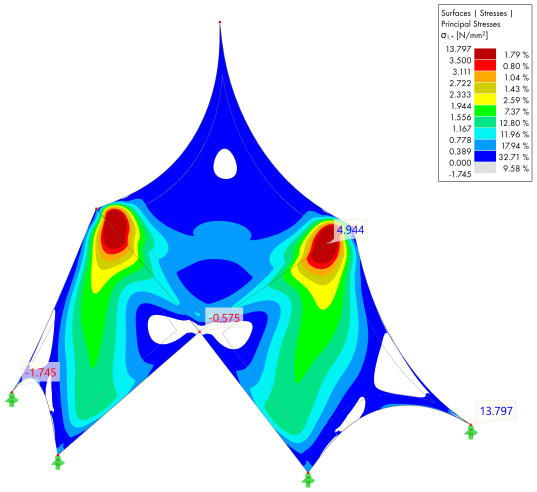

(c) Rigid: 12.6°

Figure A.13: Combination 8 - Rigid: Tensile stresses under self-weight for rotation angles (a) 0°, (b) -9.0°, and (c) 12.6°

A.3.2. Combination 6

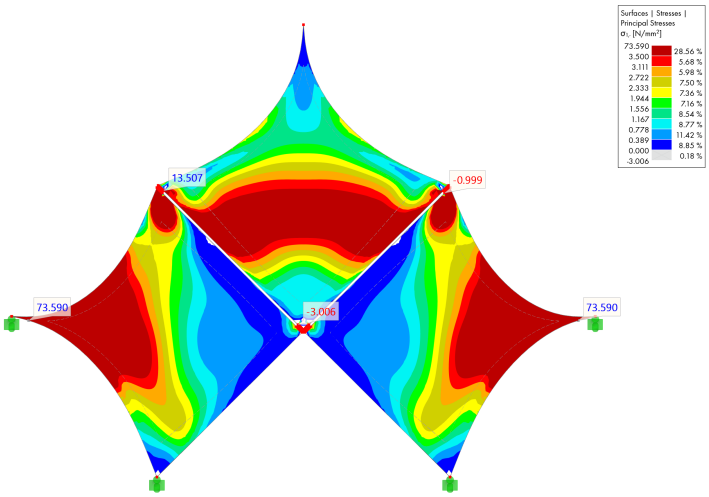

(a) Linked: 0°

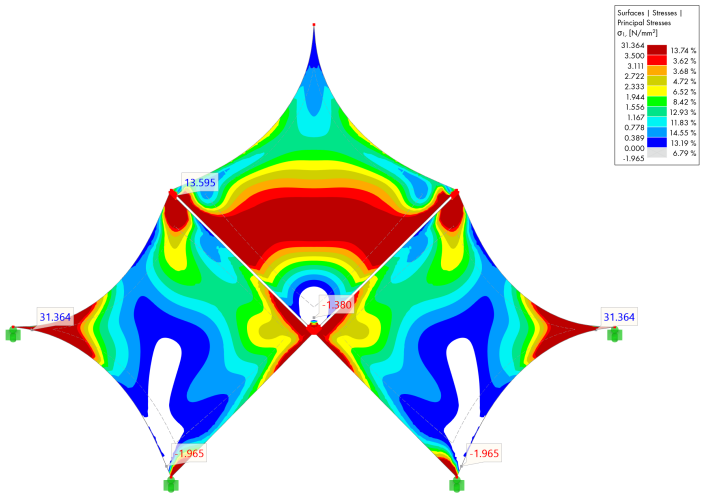

(b) Linked: -7.2°

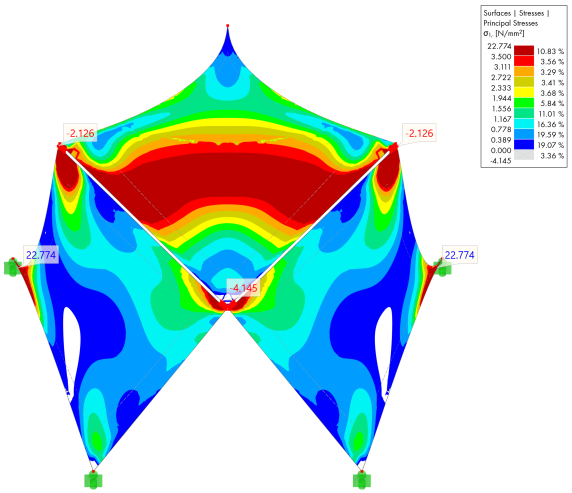

(c) Linked: 37.8°

Figure A.14: Combination 6 - Linked: Tensile stresses under self-weight for rotation angles (a) 0°, (b) -7.2°, and (c) 37.8°

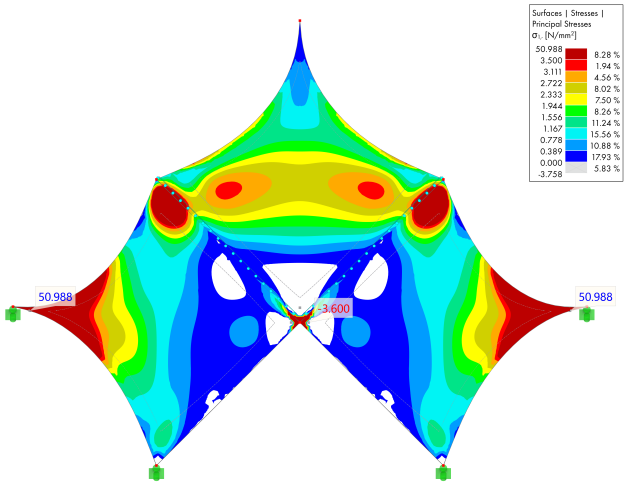

(a) Hinged: 0°

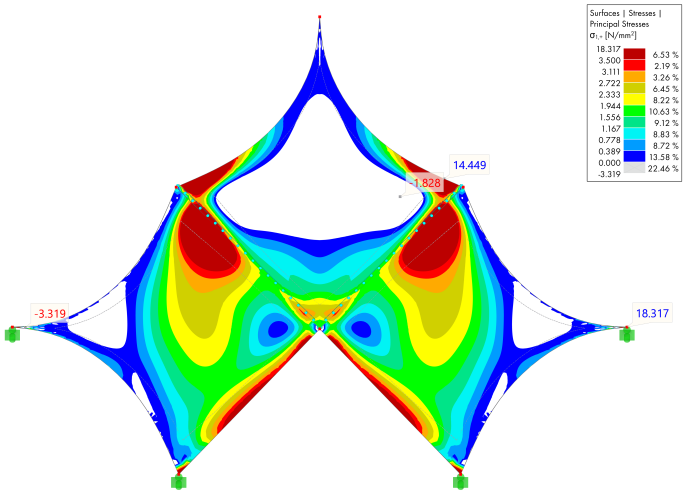

(b) Hinged: -10.8°

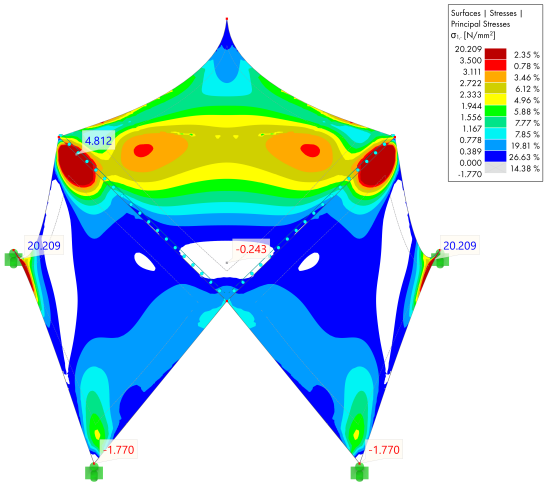

(c) Hinged: 37.8°

Figure A.15: Combination 6 - Hinged: Tensile stresses under self-weight for rotation angles (a) 0°, (b) -10.8°, and (c) 37.8°

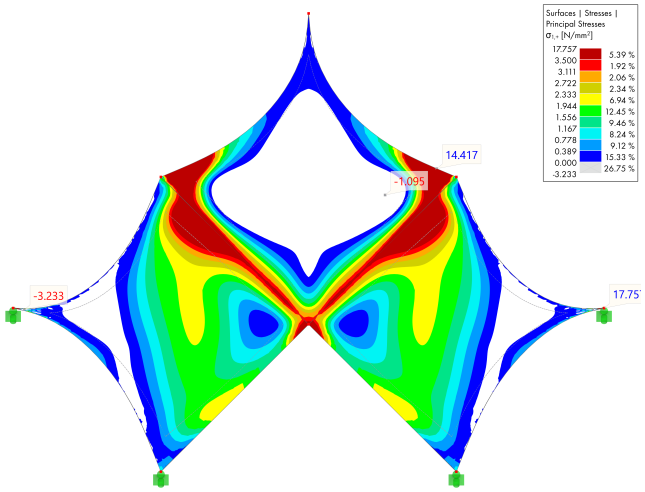

(a) Rigid: 0°

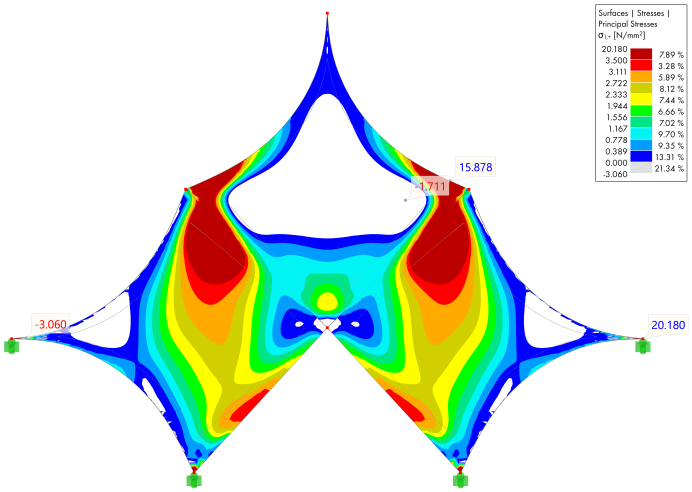

(b) Rigid: -19.8°

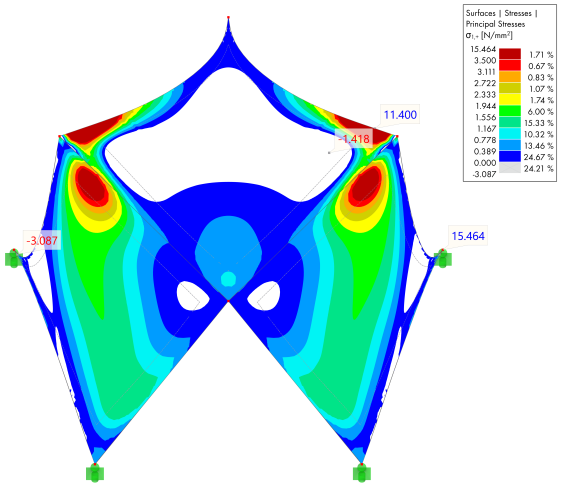

(c) Rigid: 37.8°

Figure A.16: Combination 6 - Rigid: Tensile stresses under self-weight for rotation angles (a) 0°, (b) -19.8°, and (c) 37.8°

A.3.3. Combination 10

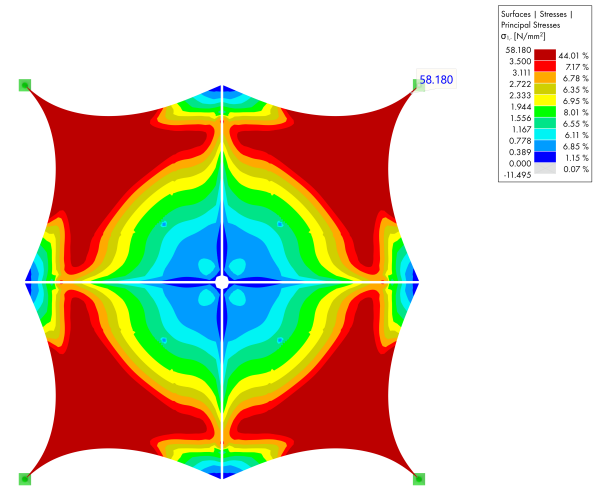

(a) Linked

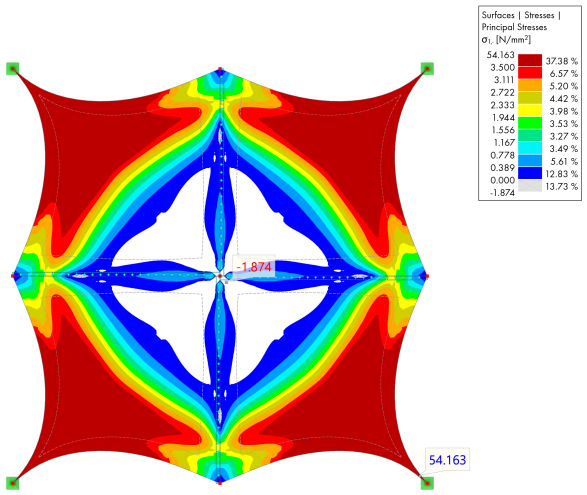

(b) Hinged

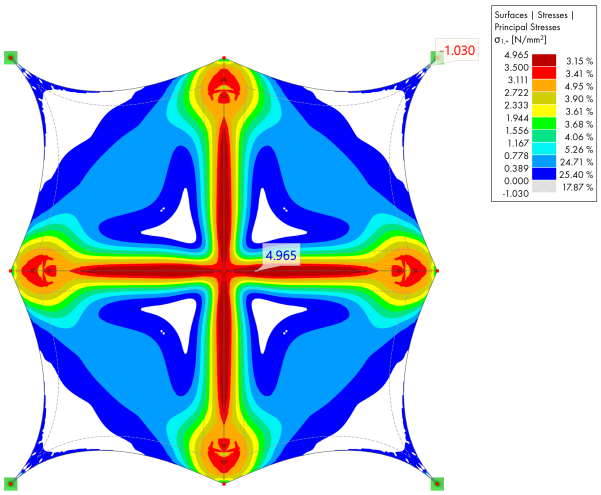

(c) Rigid

Figure A.17: Combination 10: Tensile stresses under self-weight for (a) linked, (b) hinged, and (c) rigid connection

A.3.4. Combination 5

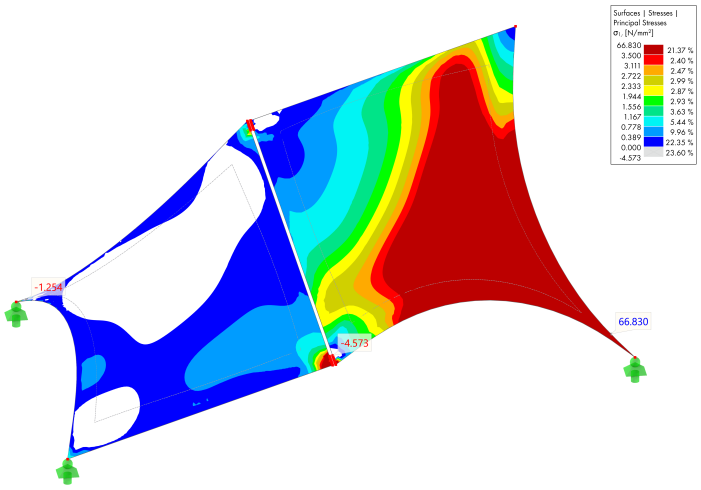

(a) Linked: 37.8° (as-built)

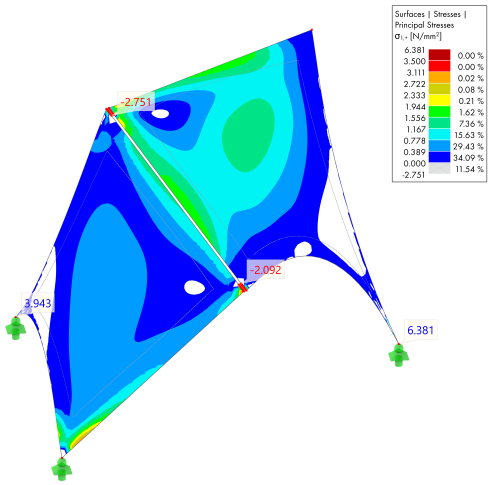

(b) Linked: 84.6° (optimized)

Figure A.18: Combination 5 - Linked: Tensile stresses under self-weight for rotation angles (a) 37.8° (as-built) and (b) 84.6° (optimized)

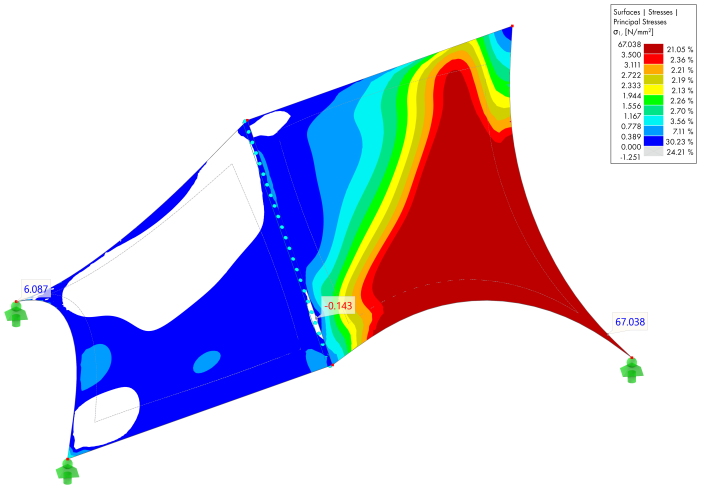

(a) Hinged: 37.8° (as-built)

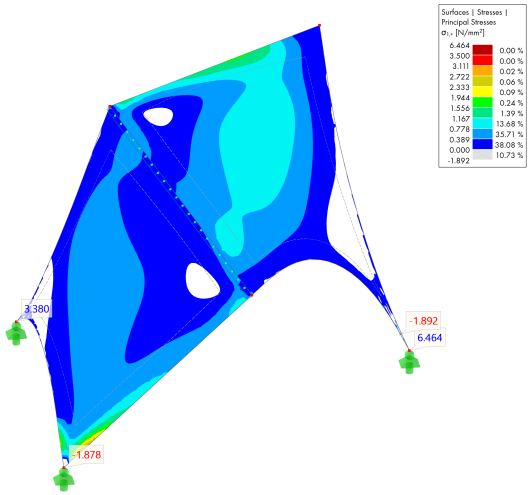

(b) Hinged: 84.6° (optimized)

Figure A.19: Combination 5 - Hinged: Tensile stresses under self-weight for rotation angles (a) 37.8° (as-built) and (b) 84.6° (optimized)

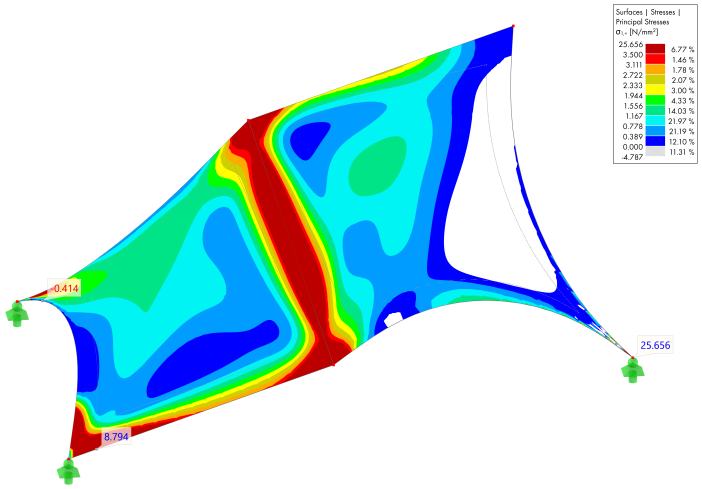

(a) Rigid: 37.8° (as-built)

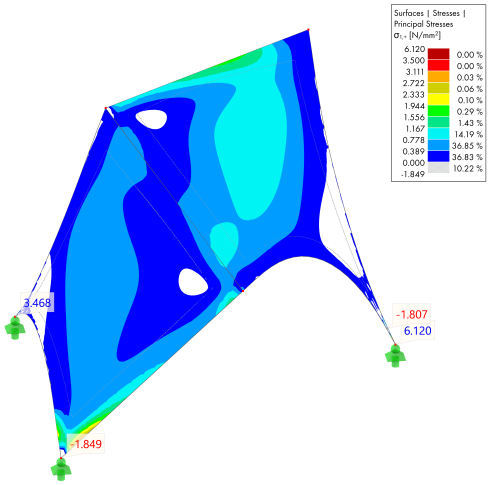

(b) Rigid: 84.6° (optimized)

Figure A.20: Combination 5 - Rigid: Tensile stresses under self-weight for rotation angles (a) 37.8° (as-built) and (b) 84.6° (optimized)

A.3.5. Combination 2.1

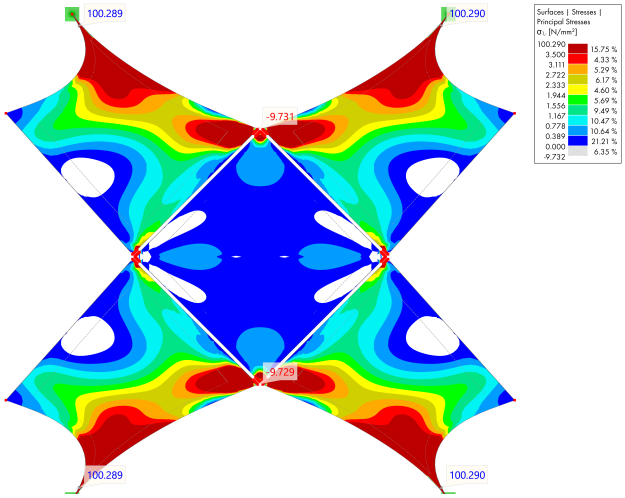

(a) Linked: 28.8°

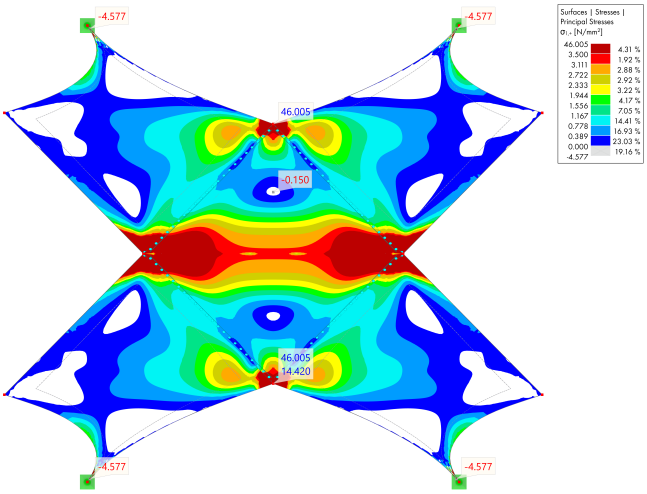

(b) Hinged: 21.6°

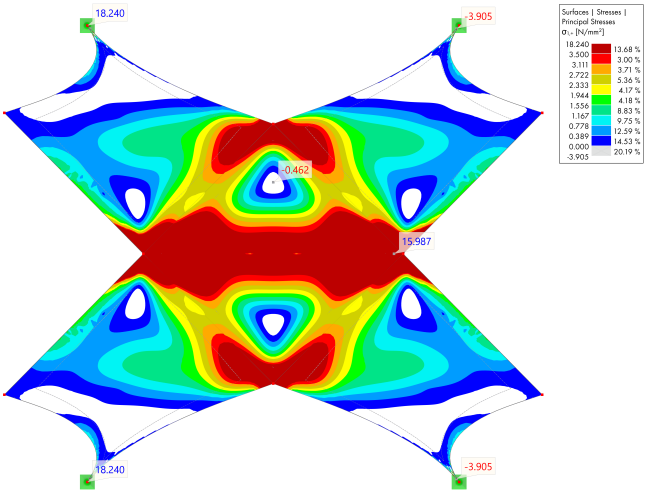

(c) Rigid: 21.6°

Figure A.21: Combination 2.1: Tensile stresses under self-weight for rotation angles (a) 28.8° (linked connection), (b) 21.6° (hinged connection), and (c) 21.6° (rigid connection)

A.3.6. Combination 2.2

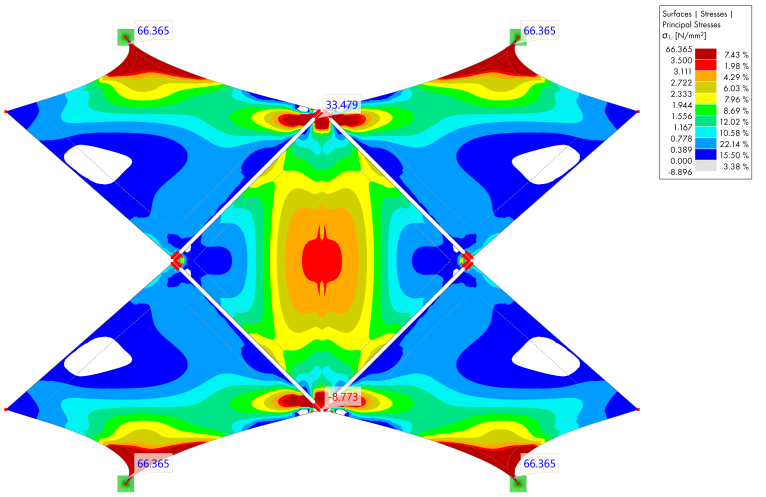

(a) Linked: -10.8°

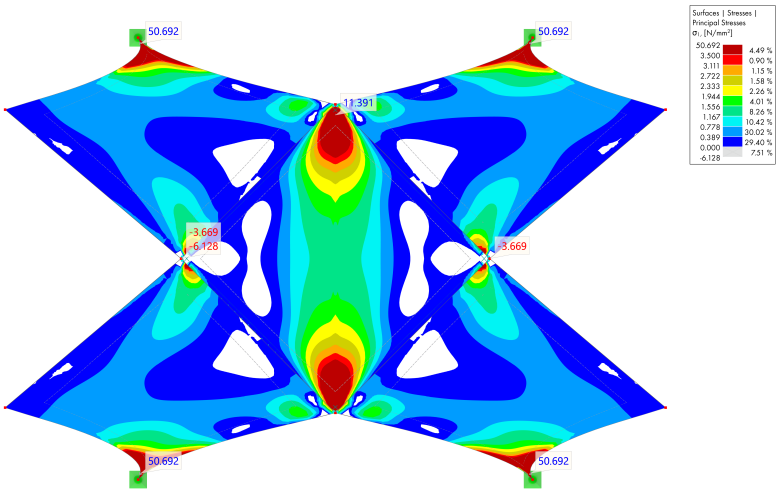

(b) Hinged: -8.1°

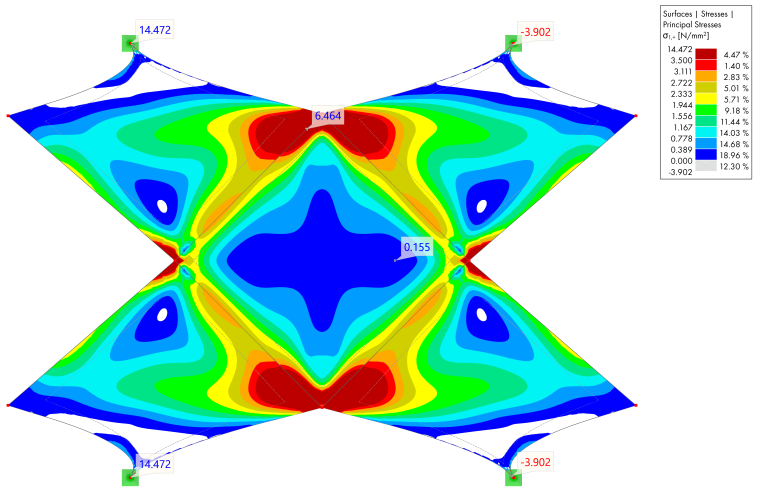

(c) Rigid: -9.9°

Figure A.22: Combination 2.2: Tensile stresses under self-weight for rotation angles (a) -10.8° (linked connection), (b) -8.1° (hinged connection), and (c) -9.9° (rigid connection)

A.3.7. Combination 19

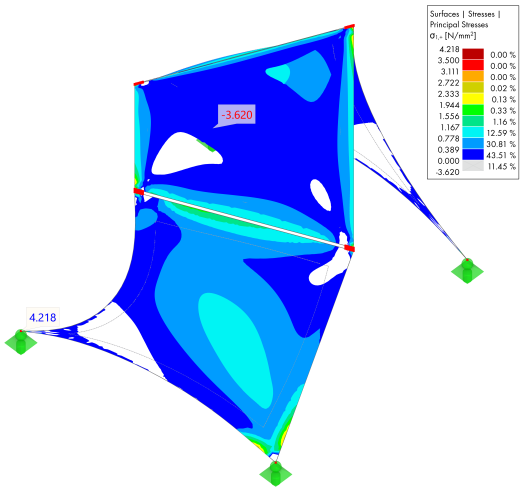

(a) Linked

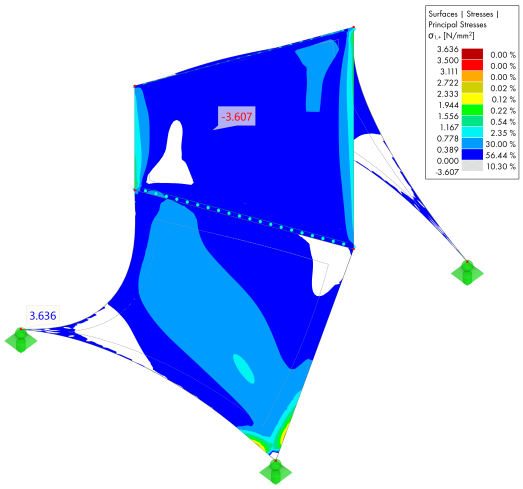

(b) Hinged

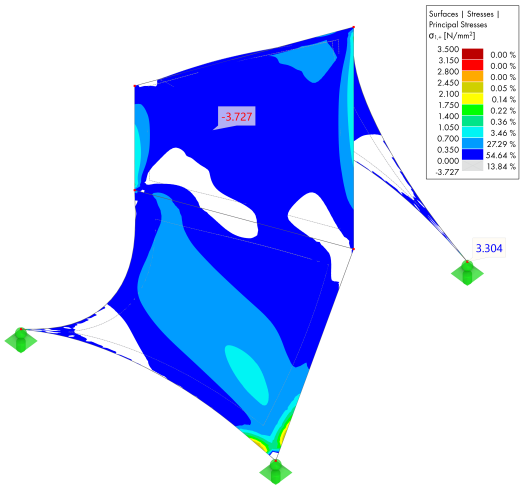

(c) Rigid

Figure A.23: Combination 19: Tensile stresses under self-weight for (a) linked connection, (b) hinged connection, and (c) rigid connection

A.3.8. Combination 20

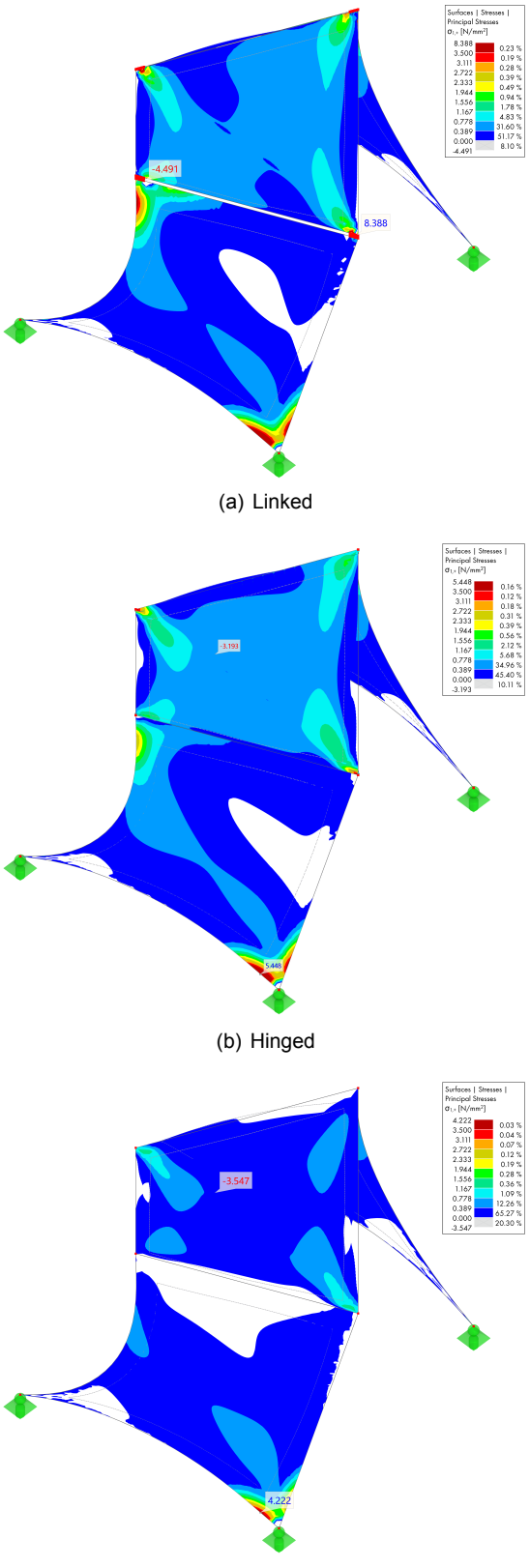

(a) Linked

(b) Hinged

(c) Rigid

Figure A.24: Combination 20: Tensile stresses under self-weight for (a) linked connection, (b) hinged connection, and (c) rigid connection

A.4. Deformation analysis results

A.4.1. Combination 8

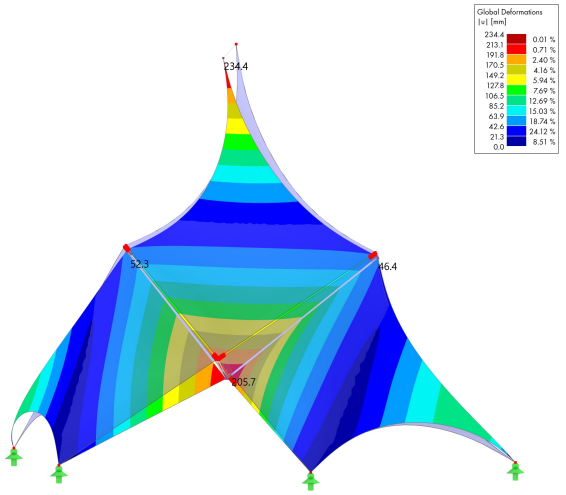

(a) Linked: 0°

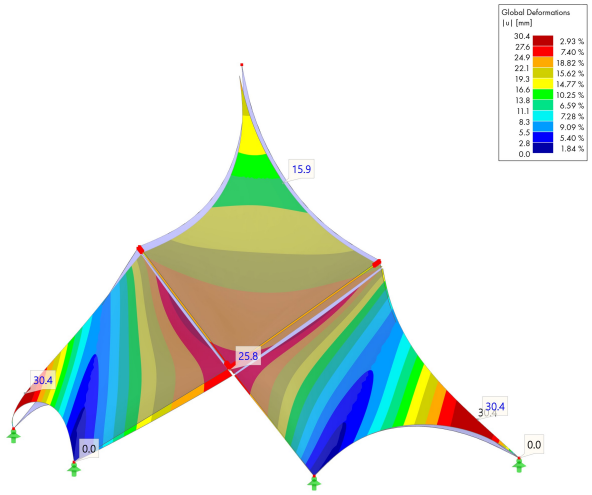

(b) Linked: -7.2°

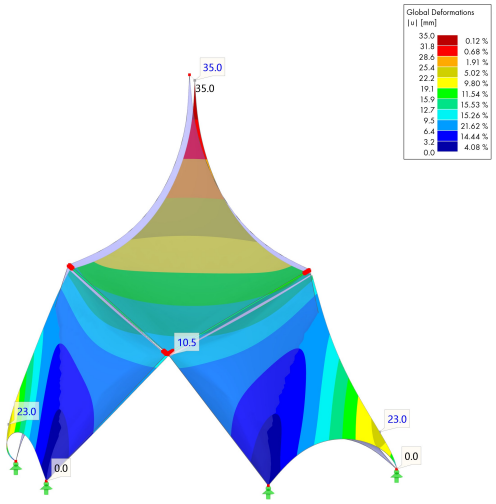

(c) Linked: 23.4°

Figure A.25: Combination 8 - Linked: Deformations under self-weight for rotation angles (a) 0°, (b) -7.2°, and (c) 23.4°

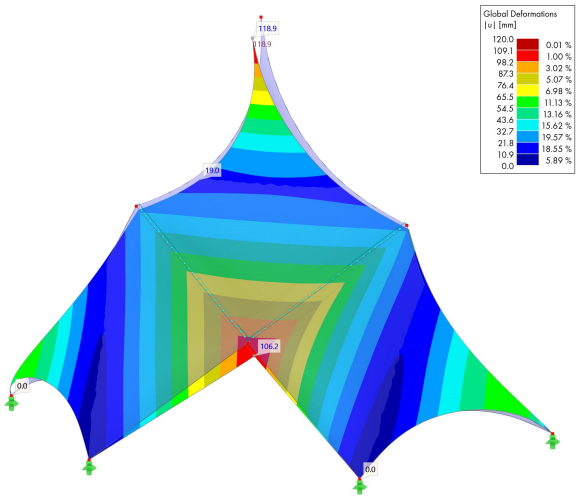

(a) Hinged: 0°

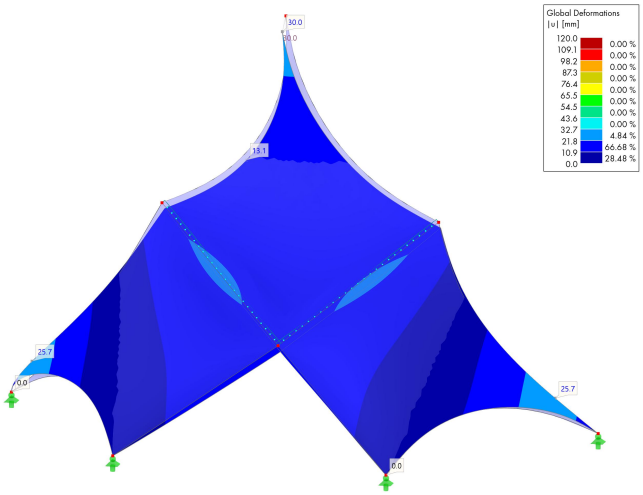

(b) Hinged: -9.0°

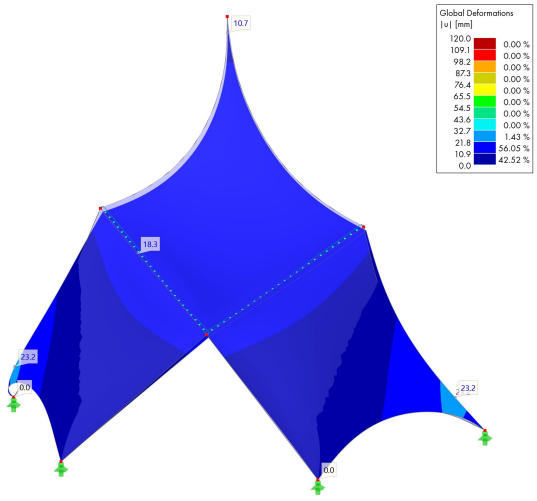

(c) Hinged: 12.6°

Figure A.26: Combination 8 - Hinged: Deformations under self-weight for rotation angles (a) 0°, (b) -9.0°, and (c) 12.6°

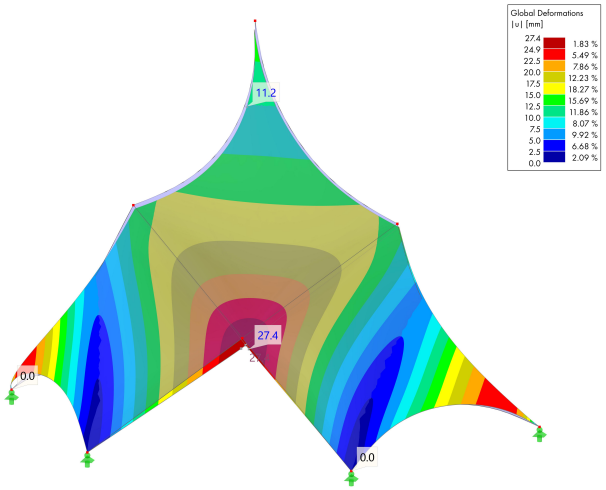

(a) Rigid: 0°

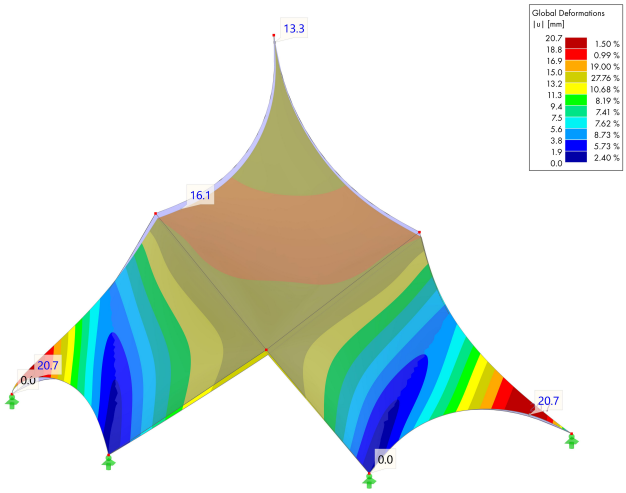

(b) Rigid: -9.0°

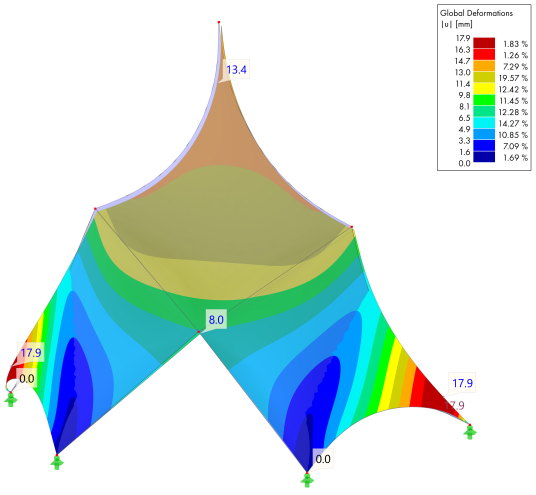

(c) Rigid: 12.6°

Figure A.27: Combination 8 - Rigid: Deformation under self-weight for rotation angles (a) 0°, (b) -9.0°, and (c) 12.6°

A.4.2. Combination 6

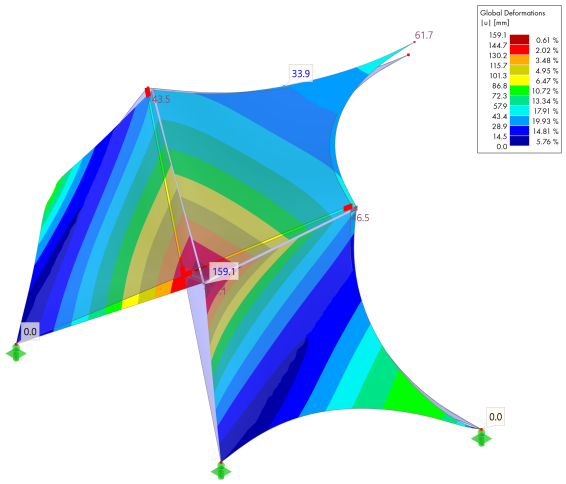

(a) Linked: 0°

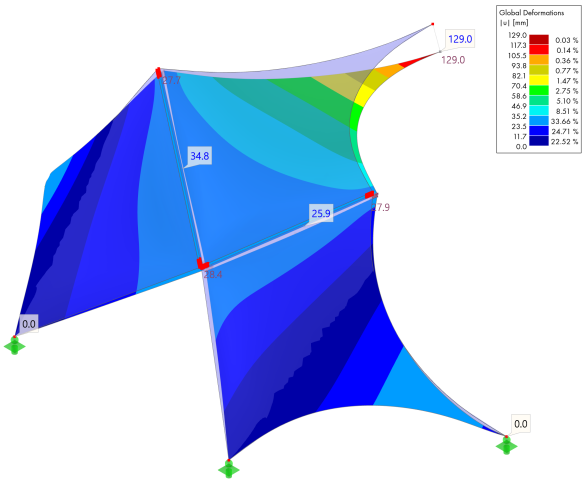

(b) Linked: -7.2°

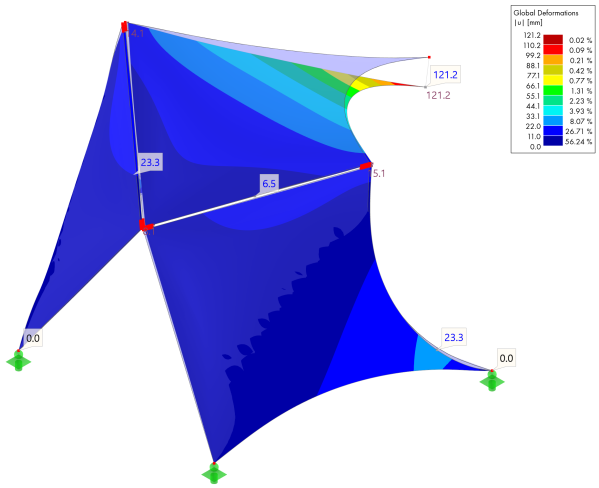

(c) Linked: 37.8°

Figure A.28: Combination 6 - Linked: Deformations under self-weight for rotation angles (a) 0°, (b) -7.2°, and (c) 37.8°

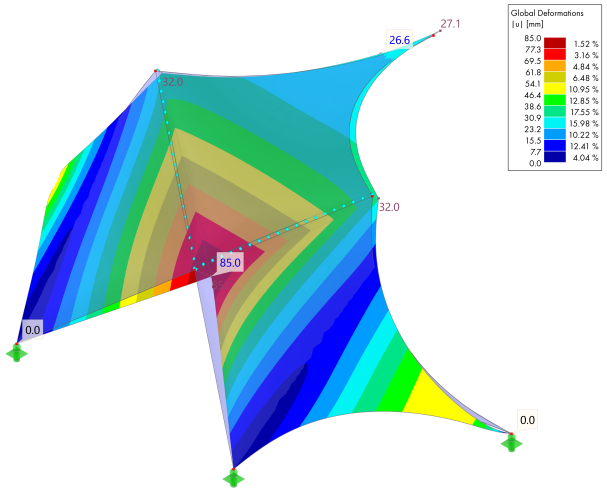

(a) Hinged: 0°

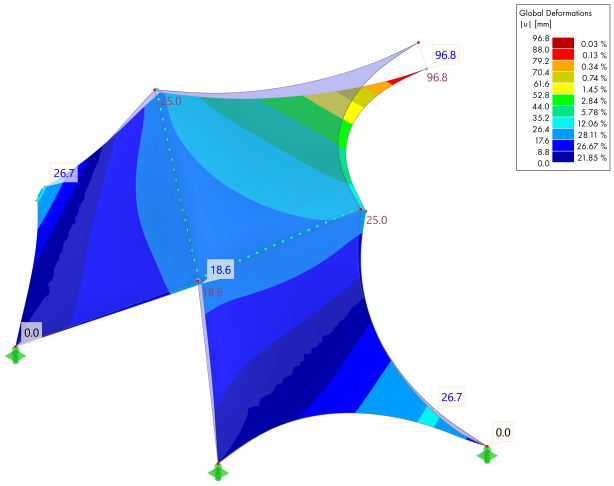

(b) Hinged: -10.8°

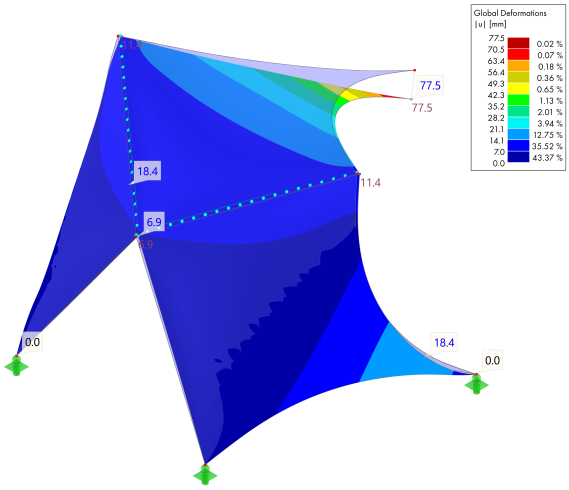

(c) Hinged: 37.8°

Figure A.29: Combination 6 - Hinged: Deformations under self-weight for rotation angles (a) 0°, (b) -10.8°, and (c) 37.8°

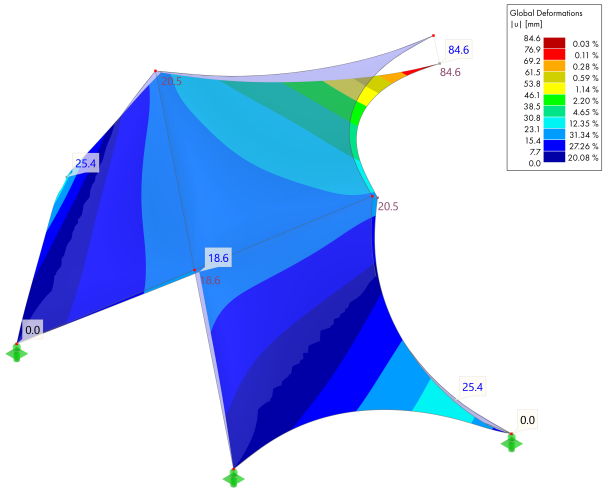

(a) Rigid: 0°

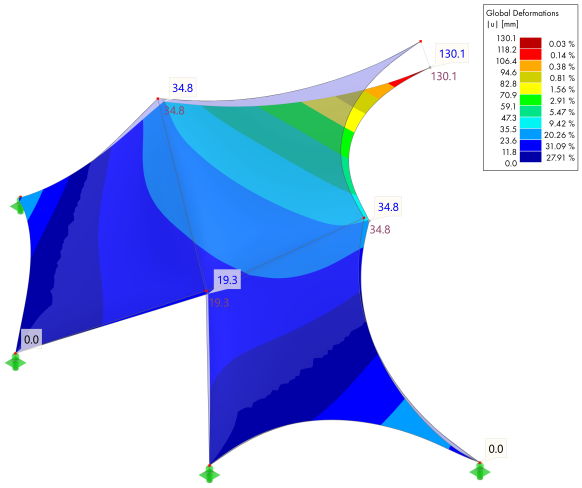

(b) Rigid: -19.8°

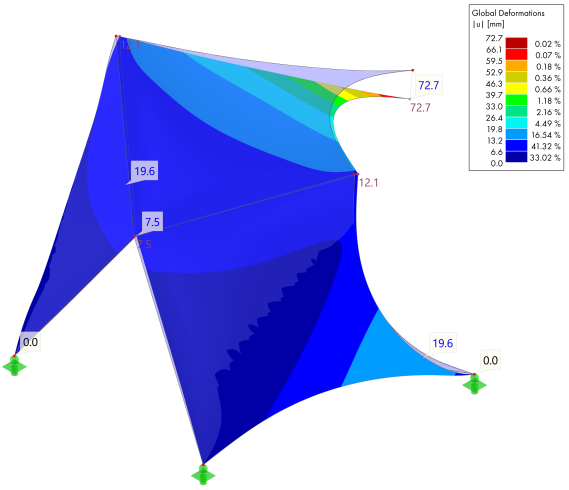

(c) Rigid: 37.8°

Figure A.30: Combination 6 - Rigid: Deformations under self-weight for rotation angles (a) 0°, (b) -19.8°, and (c) 37.8°

A.4.3. Combination 10

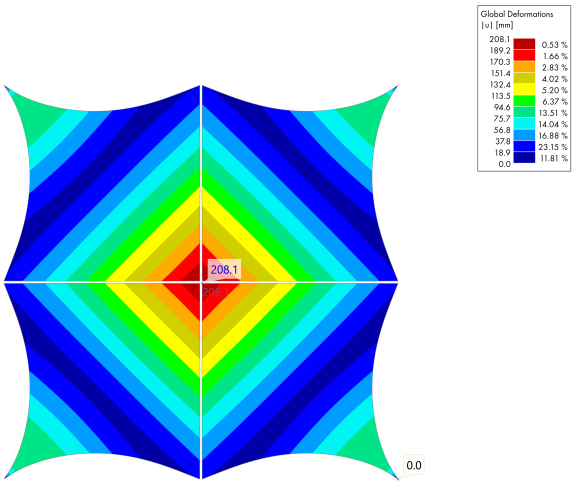

(a) Linked

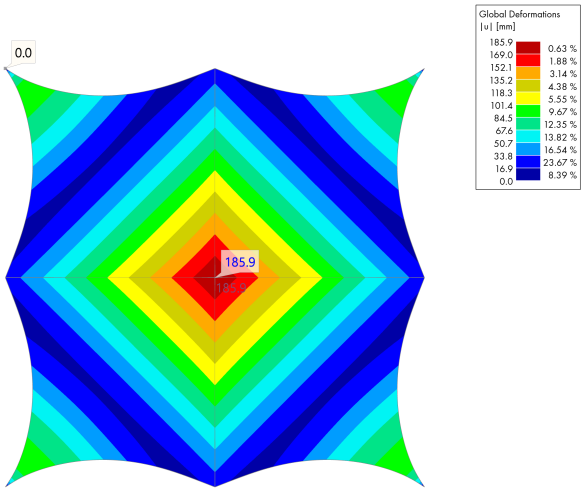

(b) Hinged

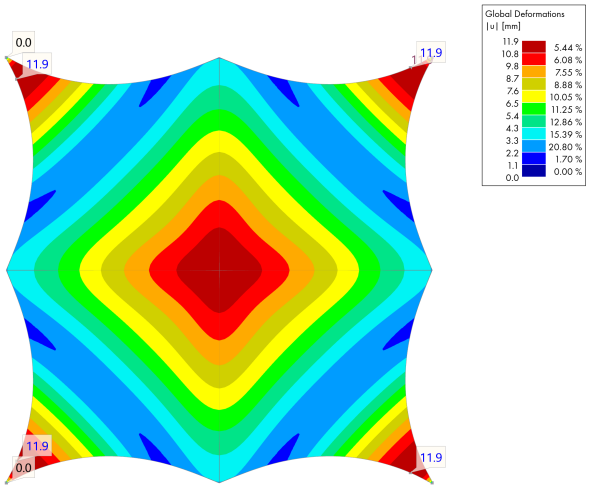

(c) Rigid

Figure A.31: Combination 10: Deformations under self-weight for (a) linked, (b) hinged, and (c) rigid connection

A.4.4. Combination 5

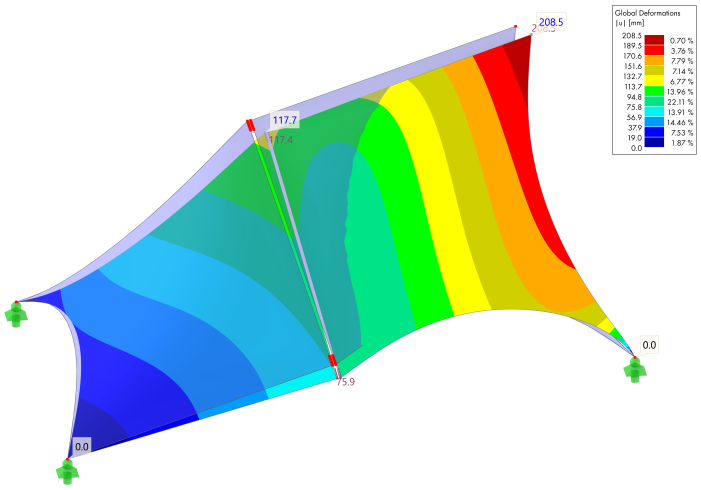

(a) Linked: 37.8° (as-built)

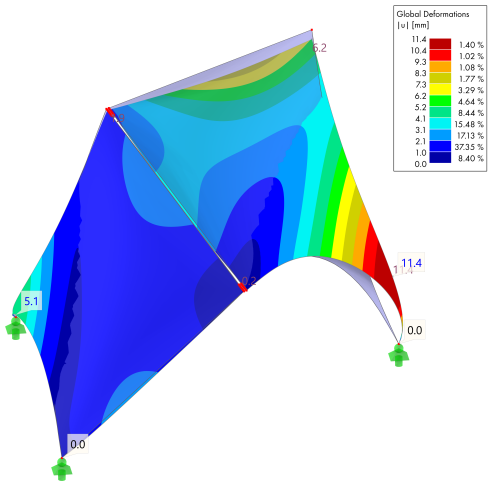

(b) Linked: 84.6° (optimized)

Figure A.32: Combination 5 - Linked: Deformations under self-weight for rotation angles (a) 37.8° (as-built) and (b) 84.6° (optimized)

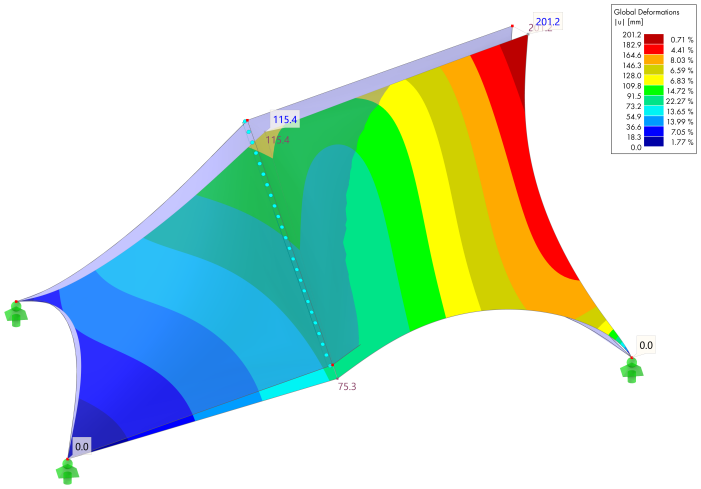

(a) Hinged: 37.8° (as-built)

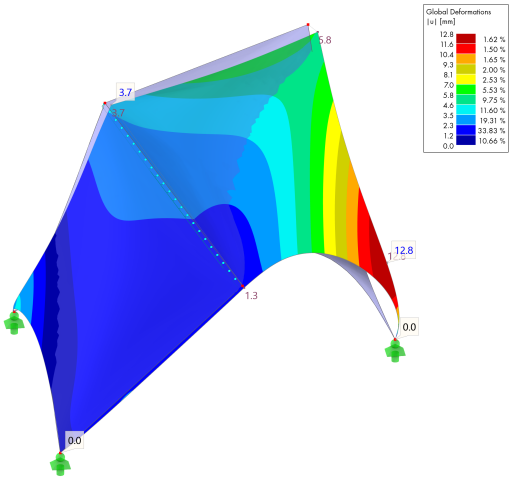

(b) Hinged: 84.6° (optimized)

Figure A.33: Combination 5 - Hinged: Deformations under self-weight for rotation angles (a) 37.8° (as-built) and (b) 84.6° (optimized)

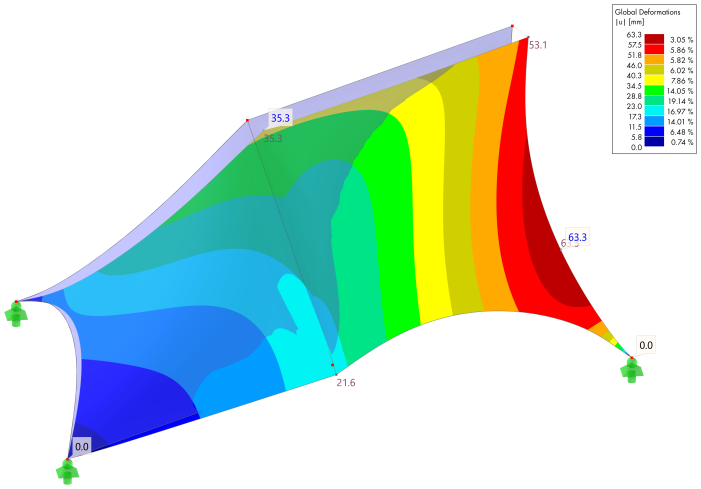

(a) Rigid: 37.8° (as-built)

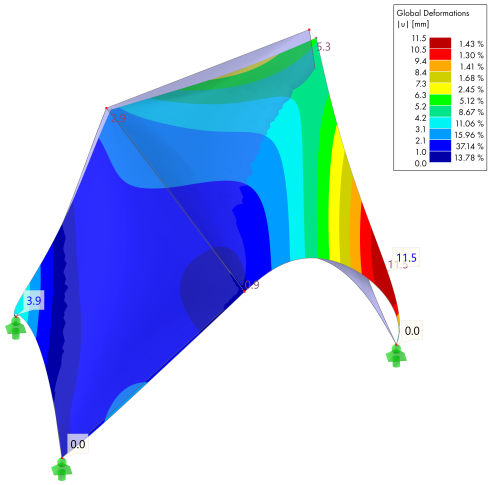

(b) Rigid: 84.6° (optimized)

Figure A.34: Combination 5 - Rigid: Deformation under self-weight for rotation angles (a) 37.8° (as-built) and (b) 84.6° (optimized)

A.4.5. Combination 2.1

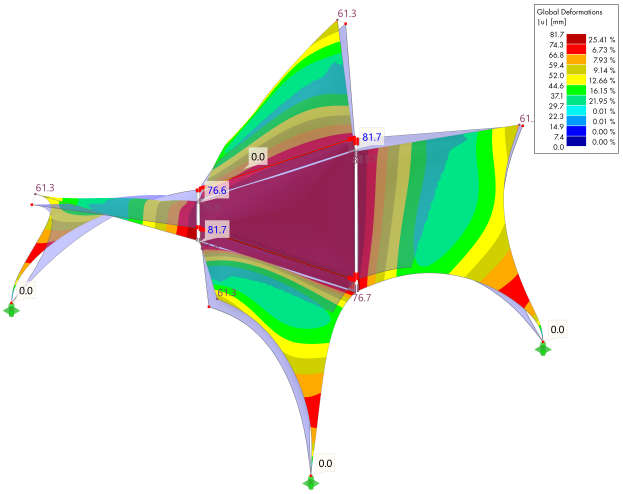

(a) Linked: 28.8°

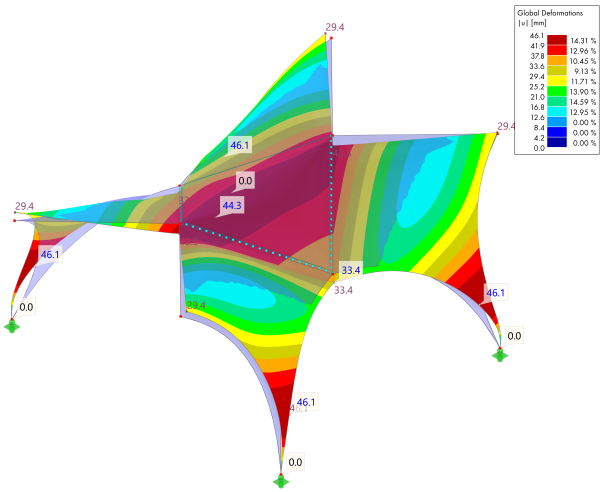

(b) Hinged: 21.6°

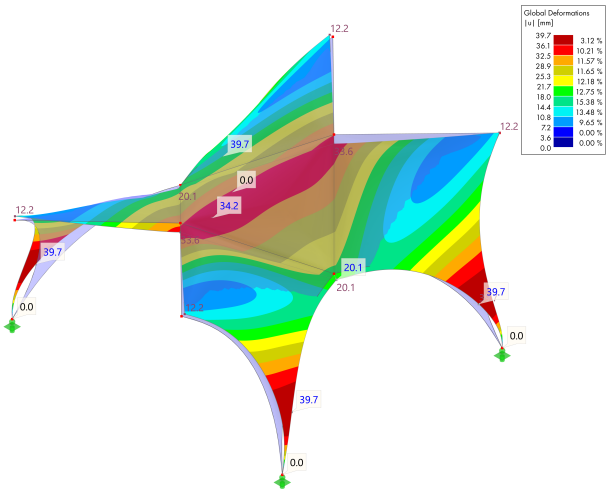

(c) Rigid: 21.6°

Figure A.35: Combination 2.1: Deformation under self-weight for rotation angles (a) 28.8° (linked connection), (b) 21.6° (hinged connection), and (c) 21.6° (rigid connection)

A.4.6. Combination 2.2

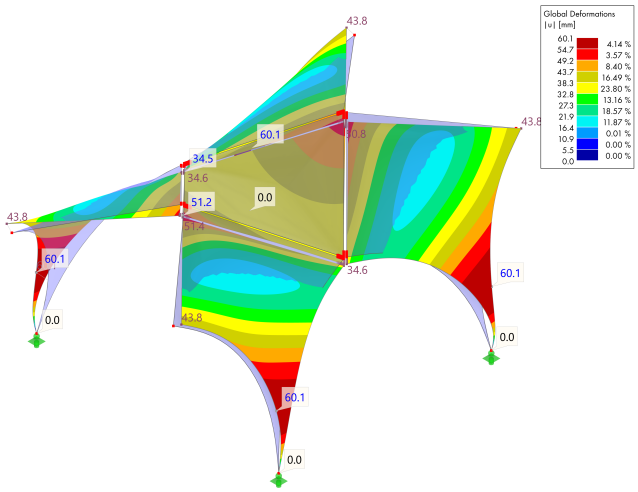

(a) Linked: -10.8°

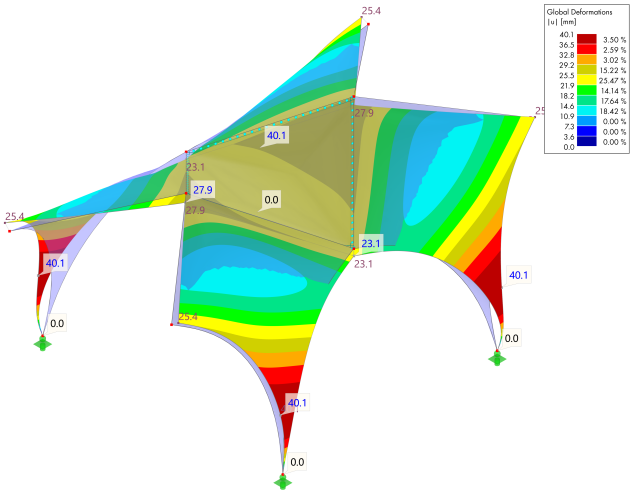

(b) Hinged: -8.1°

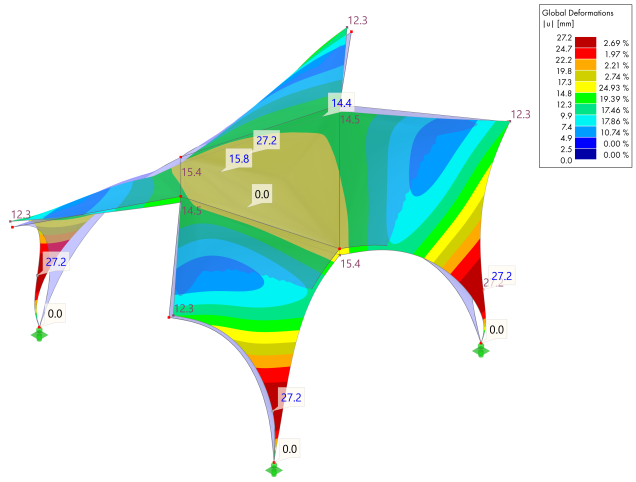

(c) Rigid: -9.9°

Figure A.36: Combination 2.2: Deformations under self-weight for rotation angles (a) -10.8° (linked connection), (b) -8.1° (hinged connection), and (c) -9.9° (rigid connection)

A.4.7. Combination 19

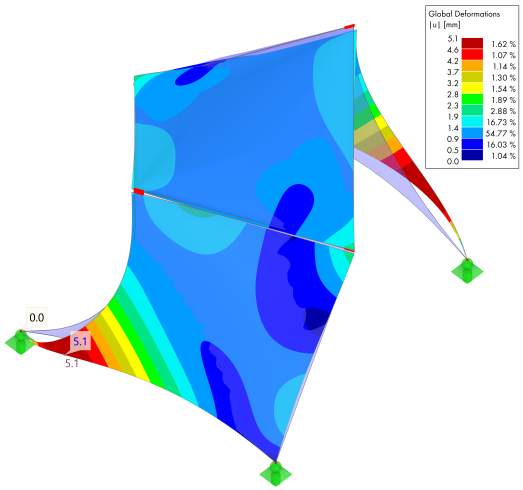

(a) Linked

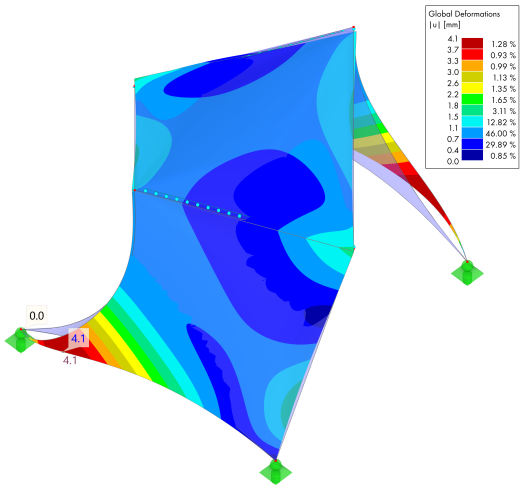

(b) Hinged

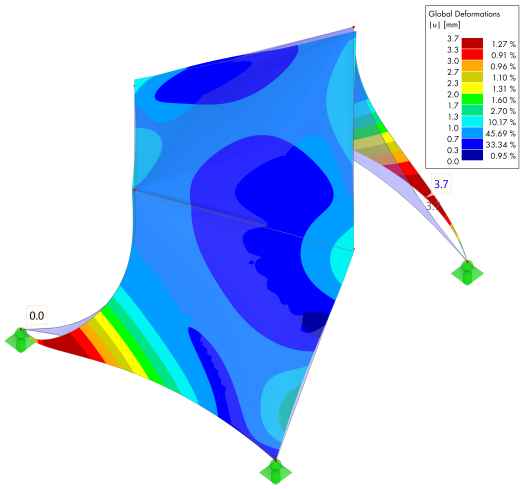

(c) Rigid

Figure A.37: Combination 19: Deformation under self-weight for (a) linked connection, (b) hinged connection, and (c) rigid connection

A.4.8. Combination 20

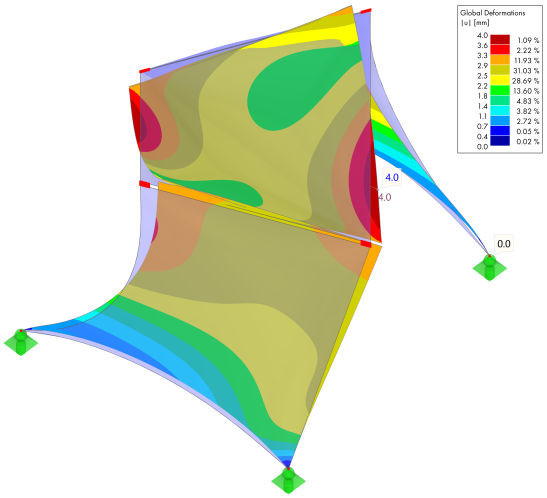

(a) Linked

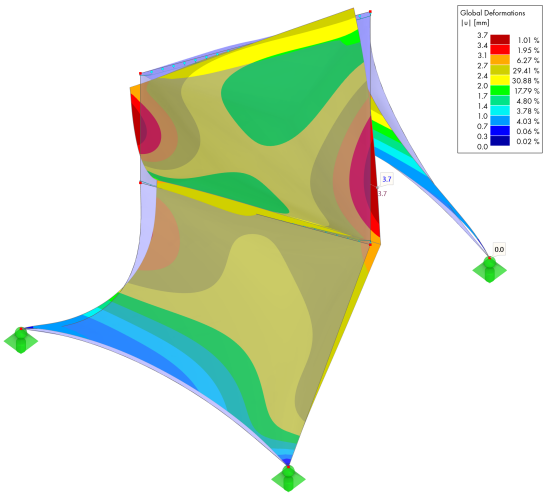

(b) Hinged

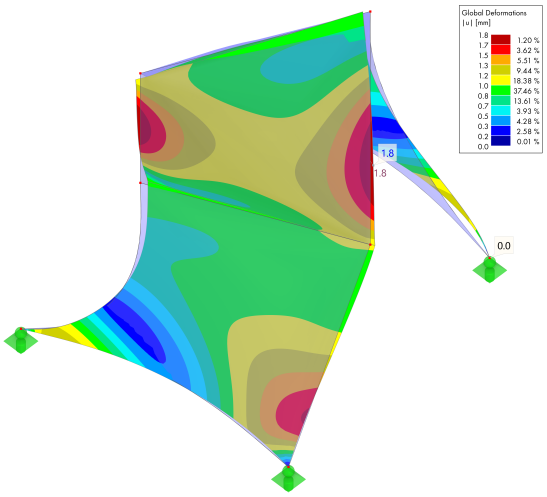

(c) Rigid

Figure A.38: Combination 20: Deformation under self-weight for (a) linked connection, (b) hinged connection, and (c) rigid connection

B

Detailed stress and deformation analysis

B.1. Combination 6

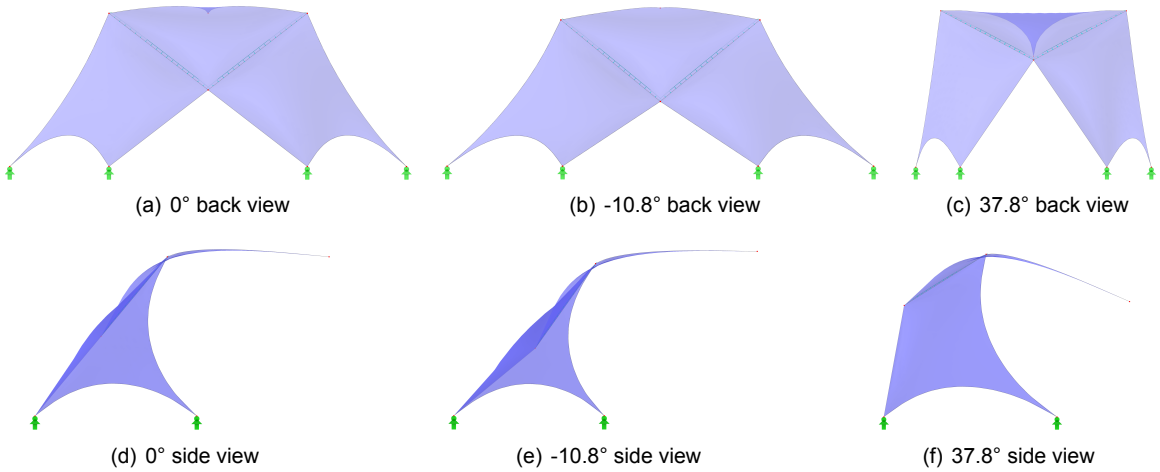

(a) 0° back view (b) -10.8° back view (c) 37.8° back view

(d) 0° side view (e) -10.8° side view (f) 37.8° side view

Figure B.1: Combination 6: Configurations resulting from strain energy analysis

B.1.1. Deformation analysis

The results of the deformation analysis of Combination 6 are presented in Figure B.2. The deformations of the structure under self-weight for the configurations at the rotation angles 0°, -10.8°, and 37.8° are shown. The individual elements are connected through hinged connections.

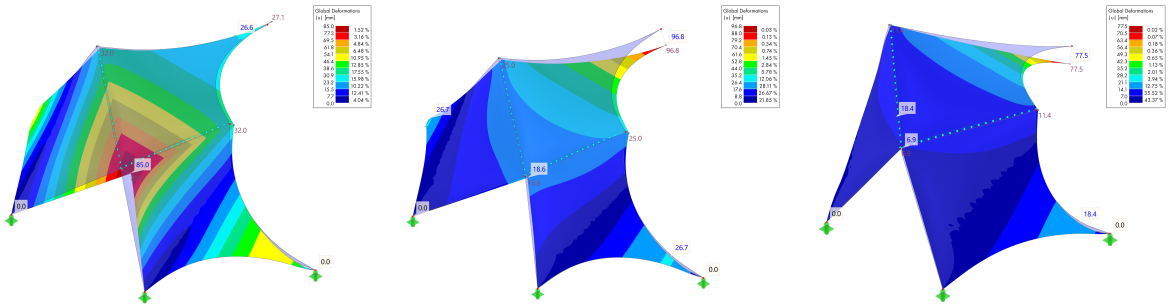

(a) 0° (b) -10.8° (c) 37.8°

Figure B.2: Combination 6: Deformation under self-weight

As shown in Figure B.2, Combination 6 exhibits relatively large deformations across all three rotation angle configurations compared to Combination 8. While the in-plane configuration at 0° rotation shows large deformations with a maximum of 85 mm at the center of the structure, the deformations of the configurations at -10.8° and 37.8° are significant lower in this region. In contrast, the two latter configurations show large deformations at the cantilevering tip of the top element. The low deformations in the center of the structure in the out-of-plane configurations indicate increased stiffness of the structures in that region due to the creases introduced by the joints between the elements. Furthermore, the configuration at 37.8° demonstrates lower deformations at both the tip (78 mm compared to 97 mm at -10.8°) and the center (7 mm compared to 19 mm at -10.8°), confirming its improved structural performance anticipated in the strain energy analysis.

B.1.2. Tensile stress analysis

The analysis of the tensile stresses in the three different rotation angle configurations of Combination 6 are shown in Figure B.3.

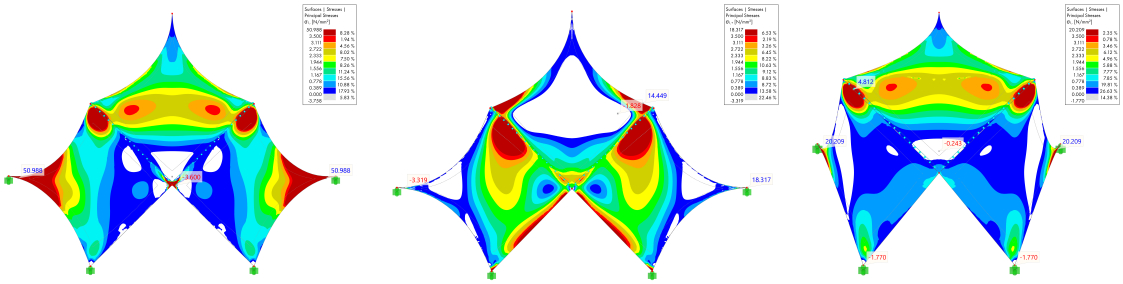

(a) 0° (b) -10.8° (c) 37.8°

Figure B.3: Combination 6: Tensile stresses under self-weight

In the rotation angle configurations at 0° and 37.8°, the maximum tensile stresses occur in the top layers of the surfaces, whereas in the -10.8° configuration, they occur in the bottom layer. The 0° configuration exhibits peak tensile stresses up to 51 N/mm^2 at the lateral support corners, exceeding the tensile capacity of the SHCC material (3.5 N/mm^2) over 8.3% of its surface area. Although the absolute maximum tensile stress in the -10.8° configuration is 18 N/mm^2, slightly lower than the 20 N/mm^2 in the 37.8° configuration, the overall performance of the 37.8° configuration is better. In this latter configuration, only 2.4% of the surface area exceeds the tensile stress limit of 3.5 N/mm^2, compared to 6.5% in the -10.8° configuration. Furthermore, despite a larger portion of the surface area being in compression in the -10.8° configuration, the 37.8° configuration shows generally lower tensile stresses across the surface.

B.2. Combination 10

B.2.1. Deformation analysis

The results of the strain energy analysis are supported by the deformation analysis. As shown in Figure B.4, the rigidly connected variant exhibits only minimal deformations of 12 mm across a diagonal span of approximately 12 meters. In contrast, the hinged and linked systems show extremely large deformations at the center of the structure, measuring 186 mm and 208 mm, respectively — 15 to 17 times greater than the rigid connection. Additionally, in the rigid connection variant, the slender ”legs” of the structure deform outward to the same extent as the center deforms downward. Meanwhile, the center of the hinged and linked structures deforms about twice as much as the ”legs” of the structure.

The highly different behavior between rigid and hinged or linked connections suggests the presence of mechanism-like effects, similar to a beam pinned at both supports with a hinge in the middle. This phenomenon can be traced to the configuration of the interface edges of all four elements in one plane and to the low out-of-plane bending stiffness of the ”legs”. This planar setup, combined with the low bending stiffness, leads to significant deformations and high bending stresses in the structure.

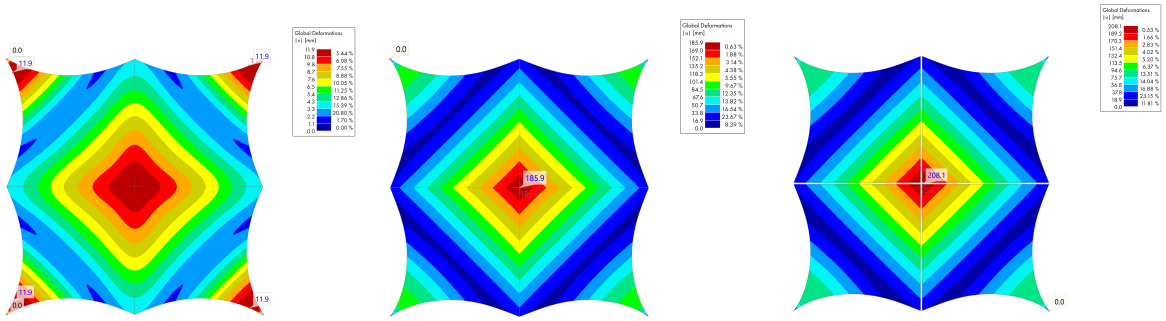

(a) rigid connection (b) hinged connection (c) linked connection

Figure B.4: Combination 10: Deformation under self-weight

B.2.2. Tensile stress analysis

The tensile stress analysis, shown in Figure B.5, confirms the significantly different behavior between the rigid and the hinged or linked variants. In the rigid variant, maximum tensile stresses occur in the bottom layer at the interface edges between the four elements, with a peak value of 5.0 N/mm^2 in these areas, and a total of 3.2% of the surface area exceeding the limit of 3.5 N/mm^2. In contrast, both the hinged and linked variants exhibit maximum stresses in the top layer at the support regions, with relatively low tensile stresses at the interfaces. These results demonstrate the bending-dominant behavior in the hinged and linked variants, leading to high tensile stresses on the surfaces. Notably, almost half of the surface areas in the hinged (37%) and linked (44%) variants exceed the SHCC’s tensile capacity .

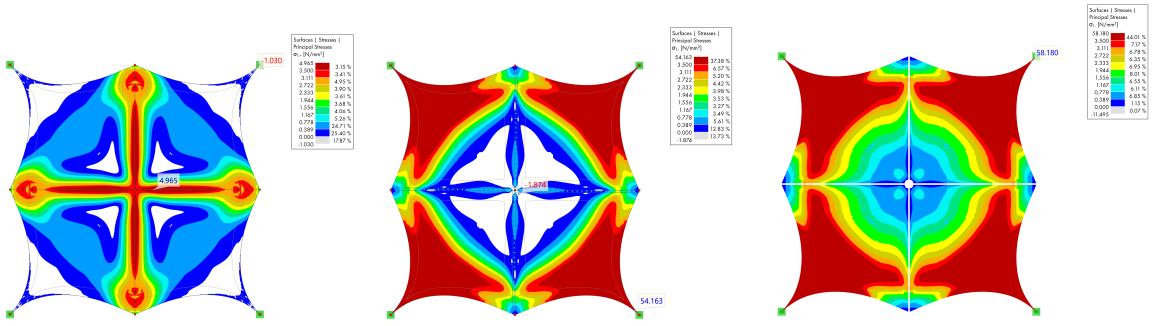

(a) rigid connection (b) hinged connection (c) linked connection

Figure B.5: Combination 10: Tensile stresses under self-weight

B.3. Combination 5

The configurations to be analyzed are shown in Figure B.6.

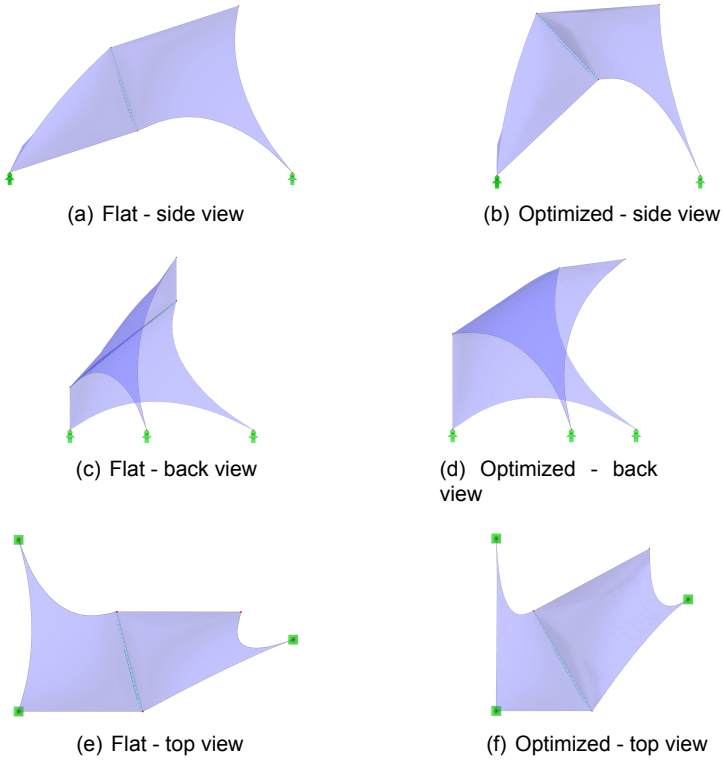

(a) Flat - side view (b) Optimized - side view

(c) Flat - back view (d) Optimized - back view

(e) Flat - top view (f) Optimized - top view

Figure B.6: Combination 5: Configurations resulting from strain energy analysis and as-built configuration

B.3.1. Deformation analysis

Figure B.7 shows the results of the deformation analysis of the flat as-built configuration and the optimized configuration with the lowest bending strain energy of Combination 5 for the hinged connection variant.

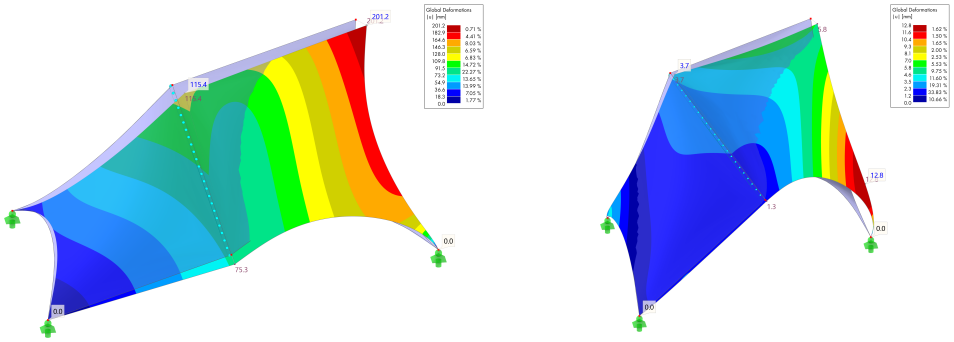

(a) Flat (as-built) (b) Optimized

Figure B.7: Combination 5: Deformation under self-weight

The optimized configuration in Figure B.7 (b), with a span between the supports of approximately 6 meters, exhibits only small deformations, with a maximum of 12.8 mm occurring near the single support of the second element. The first element, supported at two points, shows a maximum deformation of just 3.7 mm at the joint between the two elements. In contrast, the flat as-built configuration in Figure B.7

(a), with a larger span of approximately 8.5 meters, displays extremely large deformations of 114.5 mm at the joint and 201.2 mm at its highest point. The maximum deformations of the two configurations differ by a factor of 15, once again highlighting the improved structural performance of a ”steeper” configuration of the elements.

B.3.2. Tensile stress analysis

The results of the tensile stress analysis of Combination 5 shown in Figure B.8 underline the findings of the deformation analysis.

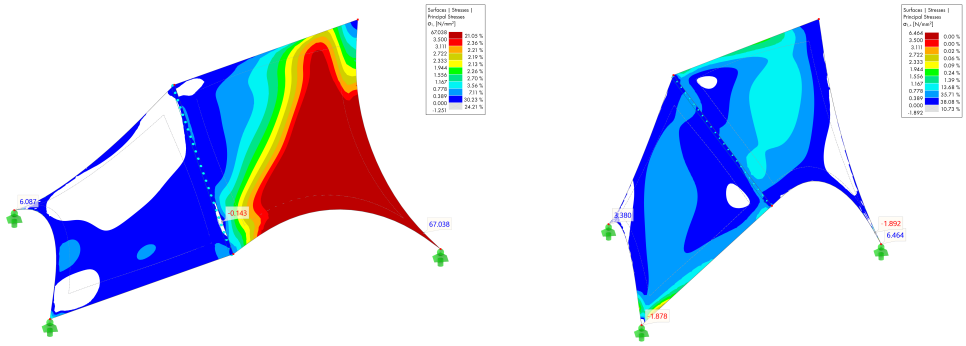

(a) Flat (as-built) (b) Optimized

Figure B.8: Combination 5: Tensile stresses under self-weight

The flat configuration exhibits high tensile stresses, with a maximum of 67.0 N/mm^2 in the top layer of the second element, resulting in 21% of the total surface area exceeding the tensile capacity of the SHCC of 3.5 N/mm^2. In contrast, the optimized configuration shows very low tensile stresses, with a localized maximum of 6.5 N/mm^2 at the point support of the second element, which is negligible and can be attributed to the modeling of the support as a point. Besides this stress concentration, the entire surface area remains below the tensile limit. Overall, the results show that even though a flat configuration with a smooth connection between the elements may appear more desirable as it suggests a more membrane-like behavior, a ”steeper” configuration, in which one element acts more in bending and the other more in in-plane compression, proves to be structurally more efficient.

B.4. Combination 2.1 and 2.2

The two configurations with rotation angles of 21.6° for Combination 2.1 and -8.1° for Combination 2.2 are depicted in Figure B.9.

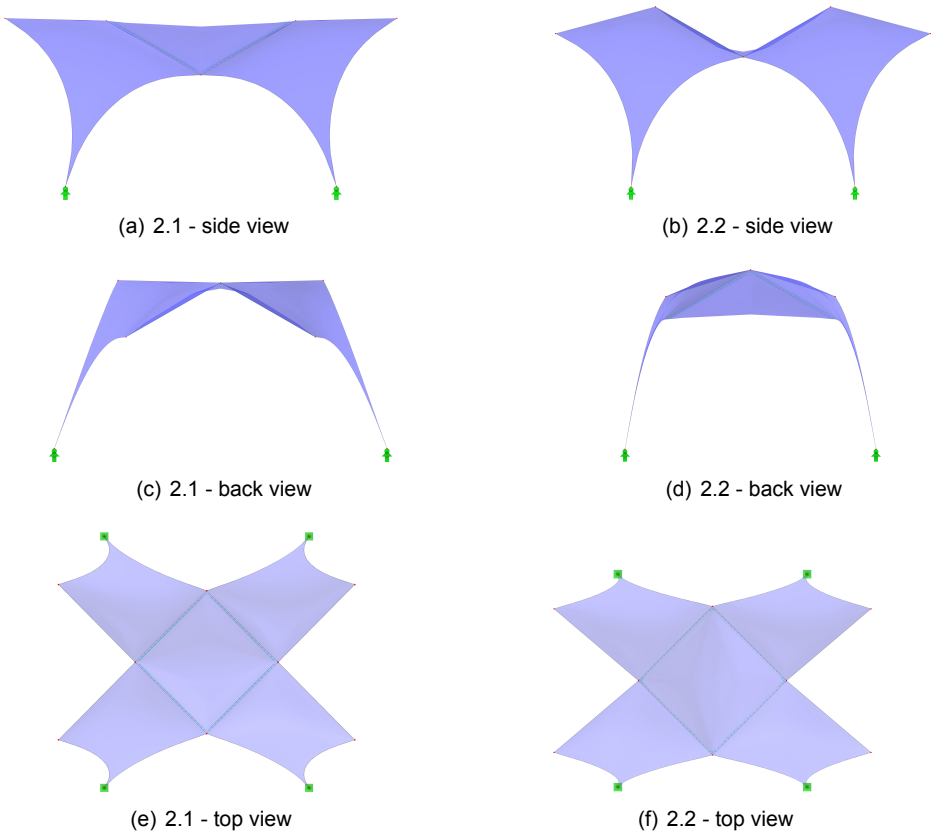

(a) 2.1 - side view (b) 2.2 - side view

(c) 2.1 - back view (d) 2.2 - back view

(e) 2.1 - top view (f) 2.2 - top view

Figure B.9: Combination 2.1 and 2.2: Configurations resulting from strain energy analysis and as-built configuration

B.4.1. Deformation analysis

In Combination 2.1, the central element of Geometry 2 deforms downwards along the longitudinal axis in the center of the structure reaching a maximum value in that region of 44.3 mm, as shown in Figure B.10. The overall maximum deformation occurs in the region of the ”legs” of the structure, which deform outward with a maximum value of 46.1 mm. In contrast, Combination 2.2 shows significantly less deformation in the central element of Geometry 2. In Combination 2.1, the central element deforms around the longitudinal axis, causing its longitudinal high corner points to deform downwards relative to its lateral, lower corner points, creating bending along the longitudinal axis. While in Combination 2.2, the longitudinal high corner points of the central element deform downwards relative to the lateral corner points as well, this now results in bending around the short, transversal axis of the structure. In total, the central element of Combination 2.2 shows a maximum deformation of only 27.9 mm. The overall maximum deformation of Geometry 2.2, as in Combination 2.1, occurs in the ”legs of the structure with a value of 40.1 mm.

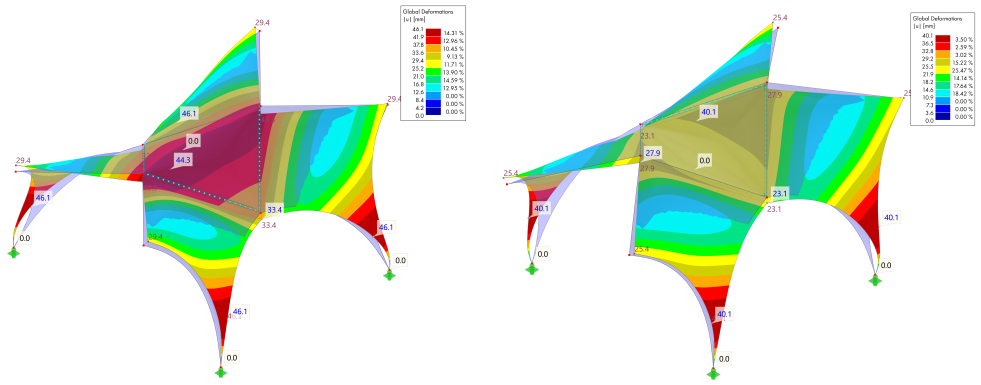

(a) 2.1: 21.6° (b) 2.2: -8.1°

Figure B.10: Combination 2.1 and 2.2: Deformation under self-weight

B.4.2. Tensile stress analysis

The previously described phenomenon of bending around the longitudinal (horizontal) axis in Combination 2.1 and bending around the transversal (vertical) axis in Combination 2.2 also shows in the results of the tensile stress analysis depicted in Figure B.11. In Combination 2.1, the maximum tensile stresses occur in the bottom layer of the surfaces, particularly along the longitudinal axis in the central element and at the corner points where three elements converge. The highest stress concentrations, with a peak value of 46.1 N/mm^2, are found at the lateral corner points of the central element. The high stresses along the longitudinal axis in the bottom layer of the central element confirm the previously described occurrence of bending around this axis. Overall, 4.3% of the surface area exceed the tensile limit of 3.5 N/mm^2. Combination 2.2 shows the highest tensile stresses at the upper layer of the surfaces, with maxima near the supports in the "legs" of the structure of 50.7 N/mm^2. Furthermore, stress concentrations are observed at the two lateral corner points of the central element. As the tensile stresses occur at the top layer of the surface, this confirms the observation of "upward" bending of the element around the transversal axis. In total, 4.5 % of the surface area exceed the SHCC's tension capacity in Combination 2.2.

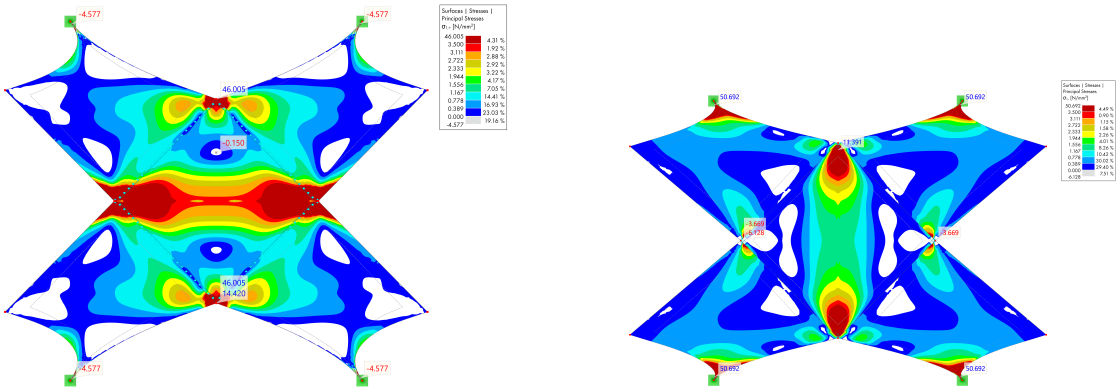

(a) 2.1: 21.6° (b) 2.2: -8.1°

Figure B.11: Combination 2.1 and 2.2: Tensile stresses under self-weight

B.5. Combination 19 and 20

The subsequently analyzed hinged configurations of Combinations 19 and 20 are illustrated in Figure B.12.

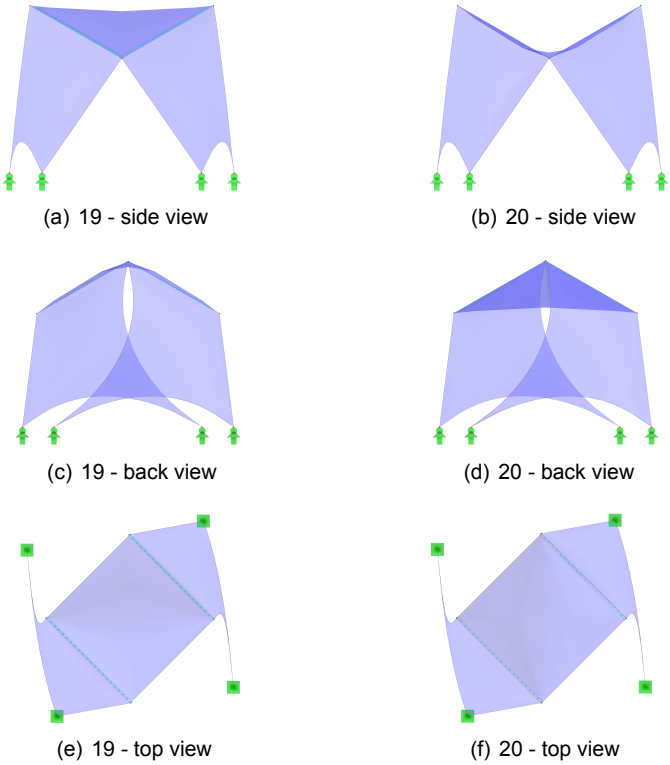

(a) 19 - side view (b) 20 - side view

(c) 19 - back view (d) 20 - back view

(e) 19 - top view (f) 20 - top view

Figure B.12: Combination 19 and 20: Configurations resulting from strain energy analysis and as-built configuration

B.5.1. Deformation analysis

Figure B.13 presents the results of the deformation analysis for Combinations 19 and 20. The maximum deformation is similar for both variants, with Combination 19 reaching 4.1 mm and Combination 20 at 3.7 mm. However, the overall deformation behavior differs significantly between the two. Combination 19 exhibits only minor deformations in the central element and most parts of the supporting elements, ranging from 0.4 to 1.6 mm, with the largest deformations of 4.1 mm occurring outward pointing in the slender parts of the bottom elements near the point supports. In contrast, Combination 20 shows its largest deformations of 3.7 mm in the middle of the unsupported edges of the top element, with larger overall surface deformations ranging from 2.0 to 3.7 mm. In Combination 20, the regions near the supports experience the smallest deformations.

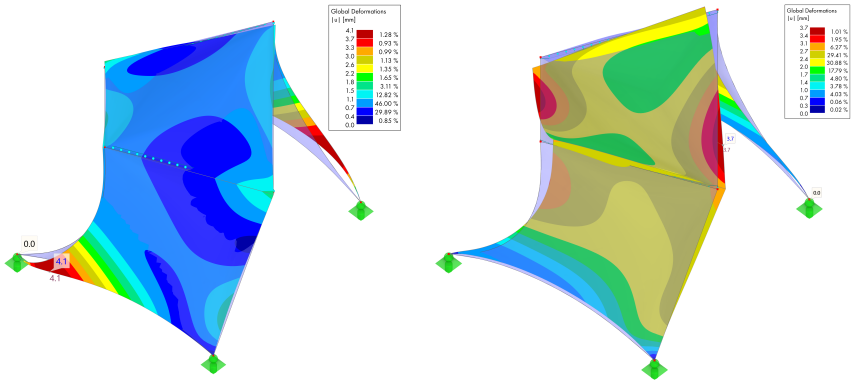

(a) 19 (b) 20

Figure B.13: Combination 19 and 20: Deformation under self-weight

B.5.2. Tensile stress analysis

The results of the tensile stress analysis are presented in Figure B.14. In both combinations, maximum stresses are observed in the bottom layer of the elements, with stress concentrations at the point supports, showing peak stresses of 3.6 N/mm^2 in Combination 19 and 5.4 N/mm^2 in Combination 20. Combination 19 exhibits increased tensile stresses along the free edges of the top element, while Combination 20 shows higher stresses localized at the corner points of the top element. Overall, the stress peaks exceeding the tensile limit in Combination 19 are negligible, and in Combination 20, only 0.16% of the surface area exceeds the limit of 3.5 N/mm^2.

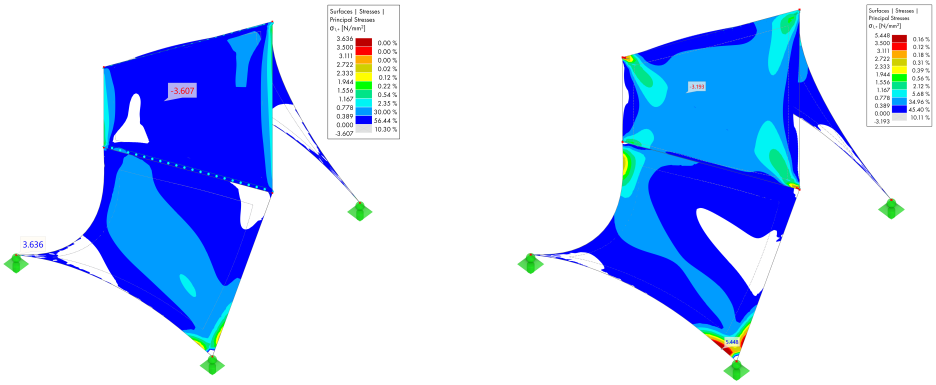

(a) 19 (b) 20

Figure B.14: Combination 19 and 20: Tensile stresses under self-weight